A great deal of attention has been given to the production of low sulphur steels by ladle treatment techniques. The work commenced in the early/mid-1970's in Japan and was quickly adopted by the Scandinavian and European steelmakers. There is now a proliferation of ladle techniques capable of producing low cost, high quality clean steels. The majority of these techniques involve the injection of a desulphurising agent into the molten steel usually using an inert carrier gas, such as argon, and often followed by a vacuum degassing treatment.

In the UK the use of such techniques for the production of gun steels, as an alternative to air melt steel, has demonstrated that significantly higher toughness levels can be obtained. Even at relatively high strength levels the properties are comparable to those obtained with good quality ESR steel. A detailed investigation[4] has been undertaken on steel produced by the argon oxygen decarburisation (AOD) process. The first experimental cast gave encouraging results although there was a problem with entrapped alumina inclusions. The second cast did not suffer from this problem and the toughness levels, Figure 10, were further enhanced, being comparable with the ESR results shown in Figure 11.

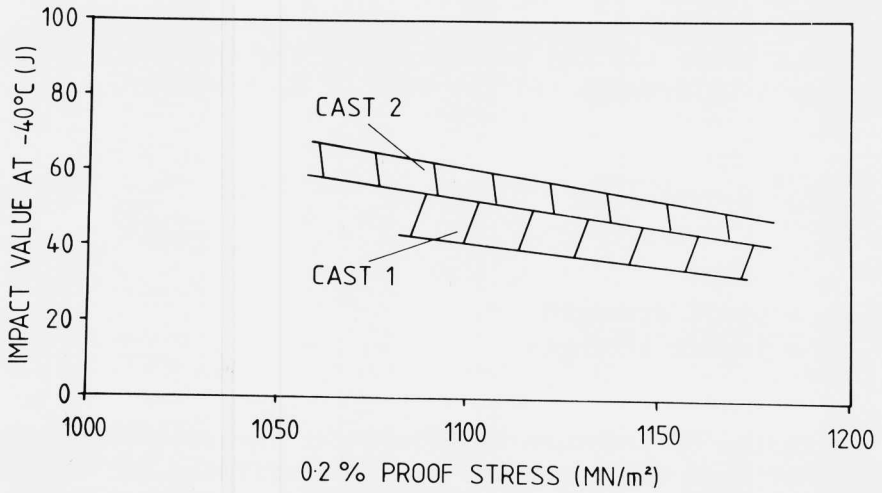

FIGURE 10. Strength/toughness properties for AOD steel.

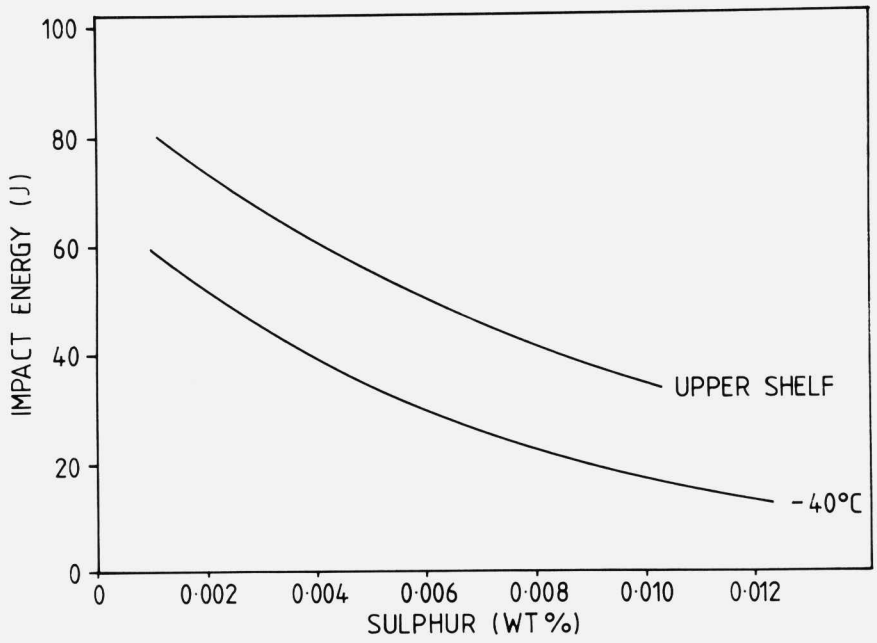

FIGURE 11. Strength/toughness properties for ESR steel.

Fracture toughness test results are shown in Table 3. It should be noted that the tests were invalid and so K_{1c} values were estimated using the relationship proposed by Barsom & Rolfe (5) and incorporating the constants derived by Hawkins & Goldthorpe (6) for 3½Ni Cr Mo V steel:

$$\left(\frac{K_{1c}}{\sigma_y}\right)^2 = 0.35 \left(\frac{C_v}{\sigma_y}\right) + 0.006 \qquad (2)$$

where σ_y = yield strength
C_v = impact strength.

Estimates of fracture toughness for the second forging were higher than those for the first, confirming the superior quality of this forging. The estimated fracture toughness for this forging was only 10-15% less than that obtained on good quality ESR steel, Figure 12. The results on the first forging were slightly lower (15-20%) but nevertheless exceeded the minimum requirements specified for ESR steel at these strength levels.

TABLE 3.

FRACTURE TOUGHNESS PROPERTIES OF GUN STEEL PRODUCED BY THE AOD PROCESS

TEST POS^{n}	FORGING 1			FORGING 2		
	0·2%PS (MN/m²)	K_Q ($MNm^{-3/2}$)	K_{IC} ($MNm^{-3/2}$)	0·2%PS (MN/m²)	K_Q ($MNm^{-3/2}$)	K_{IC} ($MNm^{-3/2}$)
A	1145	148	158	1099	NYD	167
B	1137	138	158	1061	NYD	167
C	1135	154	154	1089	NYD	164
D	1125	147	157	1121	NYD	150

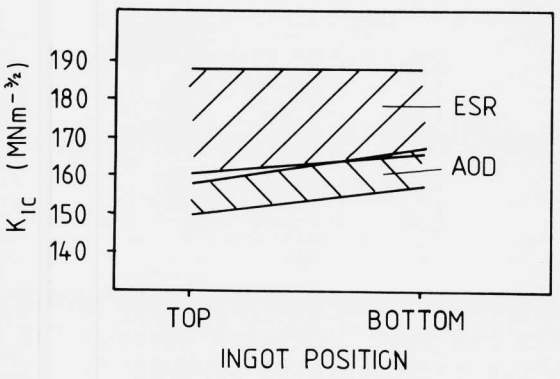

FIGURE 12. Comparison of K_{1c} values for AOD and ESR steel.

The results obtained to date on "improved quality" air melt steel, i.e., ladle or secondary refined steel, have demonstrated that such steels are capable of giving properties comparable to those obtained with ESR steel. However there has been a wide range of properties observed and, in order to consistently achieve the high levels, careful process control is required. The steelmaker must be instructed to produce a clean low sulphur steel and the best way of accomplishing this is to tighten the specification. A reduction in the maximum permitted S level together with higher minimum Charpy

and ductility requirements are necessary. This approach has already proven successful with ESR steel. This aspect is being covered in the revision of the current UK specification for gun steels where three grades and hence three levels of properties are specified. The new requirements are summarised in Figure 13 and are compared with the current standard, Defence Standard 10-13/2 issued in 1976 and its predecessor, Defence Standard 10-13/1 issued in 1968[7].

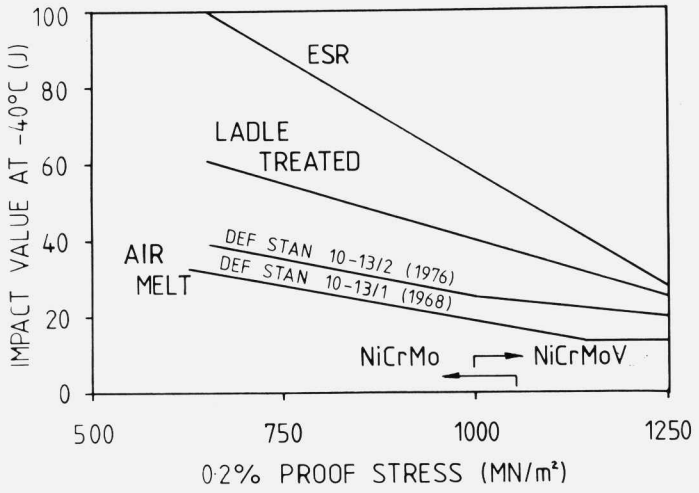

FIGURE 13. Specification requirements for gun steels.

Summary

Figure 13 demonstrates the extent to which the quality of UK gun steels has been increased through the use of improved steelmaking techniques to produce low sulphur, clean, tough steels. It was felt that further improvements in the toughness of these steels could be achieved through optimising the composition. This work is discussed in the second part of this paper.

OPTIMISATION OF EXISTING GUN STEELS

In 3½Ni Cr Mo V steels the carbon content is important because it controls the strength level via solid solution and carbide dispersion hardening. The carbon also has a significant effect on hardenability and is normally at a level of 0.3-0.4%. The carbide forming elements Cr Mo and V influence secondary hardening on tempering, in addition to providing

increased strength and hardenability by solid solution effects. It is generally considered that the alloy carbides Cr_7C_3, Mo_2C and V_4C_3 precipitate on tempering at 500-600°C and that at higher tempering temperatures the overageing carbides $M_{23}C_6$ and M_6C precipitate at the expense of Cr_7C_3 and Mo_2C[8]. At lower tempering temperatures cementite, Fe_3C, probably containing alloy elements in solid solution as $(Cr\ Mo\ V\ Fe)_3C$, is the predominant phase. Ni and Mn increase hardenability, strength and possibly toughness by solid solution effects.

An increase in the tempering temperature generally reduces strength but increases toughness as the high dislocation density of the martensite is reduced and interstitial carbon is rejected from solid solution. Grain refinement of the prior austenite will bring about toughening and strengthening of the steels as martensite packet sizes and lath widths respectively are correspondingly decreased. The use of a low hardening temperature is the simplest heat treatment method for austenite grain refinement. Particle pinning of austenite grain boundaries by undissolved precipitates will give even better grain refinement[9]. Porter & Dabkowski (10) showed that rapid heat treatment cycling is also a very effective experimental procedure for grain refining these steels.

The Ac_3 of 3¼Ni Cr Mo V steels is approximately 800°C and empirical optimisation of the heat treatment of these steels has resulted in the use of relatively low hardening temperatures, typically 860-870°C. As the Ac_1 temperature is approximately 675°C it is important to limit the tempering temperature to about 640°C to avoid partial re-austenitisation on tempering and subsequent transformation to brittle, untempered martensite on cooling after tempering.

As long ago as 1949 Crafts & Lamont (11) suggested that the optimum mechanical properties of steels are achieved when the alloying elements are present in their stoichiometric ratio with respect to the carbon content of the steel. The stoichiometry of a compound is simply the atomic weight ratio of the elements present. Hawkins et al.(12) applied this approach to 3¼Ni Cr Mo V steels and showed that for a typical steel containing 1%Cr, 0.6%Mo and 0.2%V the carbon required for stoichiometry was 0.13% compared with the normal level of 0.3-0.4%, Table 4. Experimental steels were produced containing 0.33, 0.20 and 0.12%C to investigate the effect on mechanical properties. The results are summarised in Table 5.

TABLE 4.

STOICHIOMETRIC CALCULATIONS FOR A 3¼Ni Cr Mo V GUN STEEL

ELEMENT	CARBIDE	STOICHIOMETRIC RATIO M : C	% CARBON FOR 1% ALLOY	% ALLOY IN STEEL	% CARBON REQUIRED
Cr	Cr_7C_3	16·59 : 1	0·060	1·0	0·060
Mo	Mo_2C	15·98 : 1	0·063	0·6	0·038
V	V_4C_3	5·66 : 1	0·176	0·2	0·035
			CARBON REQUIRED FOR STOICHIOMETRY		0·133

TABLE 5.

MECHANICAL PROPERTIES OF EXPERIMENTAL 0.12, 0.20 AND 0.33%C 3¼Ni Cr Mo V STEELS

CARBON (WT %)	TEMPERING TEMP(°C)	HARDNESS H_{V30}	TENSILE PROPERTIES		IMPACT PROPERTIES			
			0·2%PS (MN/m²)	UTS (MN/m²)	-40°C (J)	ITT (°C)	USE (J)	LSE (J)
0·33	630	379	1075	1158	40	-80	55	15
0·20	630	361	1048	1125	57	-60	80	9
0·12	610	375	1027	1129	42	-25	90	7

It may be seen from Table 5 that the carbon content could be reduced from 0.33 to 0.20% whilst still achieving the required strength/toughness combination of 1050MN/m^2 proof strength and 40J Charpy impact strength at -40°C. It should be noted that although there was a significant increase in upper shelf energy (USE) there was also an increase in impact transition temperature (ITT) as carbon was reduced; this may be more clearly seen in Figure 14. In addition, optical metallography revealed a marked variation in grain size of the three steels, Figure 15.

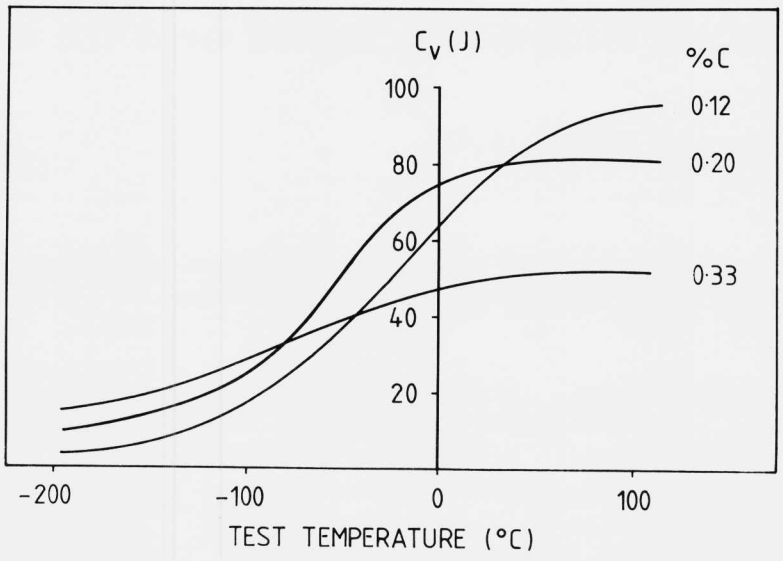

FIGURE 14. Impact transition curves for 0.12, 0.20 and 0.33%C gun steels.

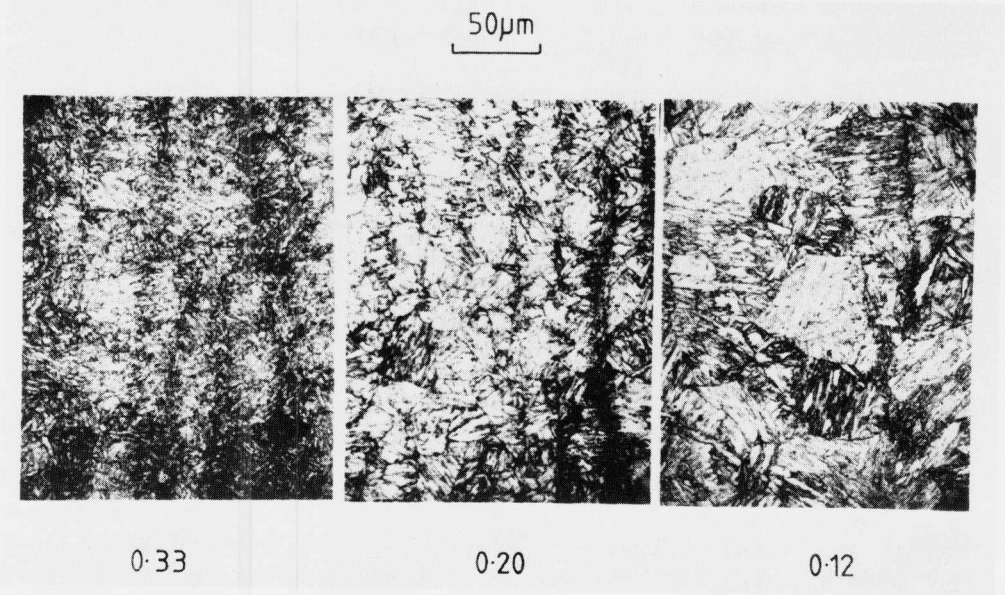

FIGURE 15. Optical micrographs for 0.33(left), 0.20(centre) and 0.12%C(right) gun steels.

These results were explained on the basis of the solubility for vanadium carbide in austenite. The solubility product for this system has been given by Narita (13) as:

$$\log[V][C] = \frac{-9500}{T} + 6.72 \qquad (3)$$

where [V] and [C] are the vanadium and carbon concentrations respectively and T is the absolute temperature.

This relationship is shown plotted for the hardening temperature of 870°C in Figure 16. The figure illustrates that the stoichiometric steel, 0.12%C, should contain no undissolved carbides, whereas the amounts of undissolved carbides should increase with carbon content. This was subsequently confirmed by electron microscopy[14]. As a consequence of this the stoichiometric steel had a higher USE than either the 0.20 or 0.33%C steels because of the lower number of coarse V_4C_3 particles, but a higher ITT because of the loss of particle pinning of the grain boundaries.

This work demonstrated that a slight excess of carbon was required in order to achieve the best compromise between a low ITT, through grain refinement, and a high USE, through a reduction in the number of coarse particles.

Subsequent work by Andrews (15) has shown that a reduction in the Mn level of the 0.2%C steel from 0.45 to 0.25% produced a further significant increase in the upper shelf energy, Figure 17. In this work Andrews also demonstrated that at the 0.3%C level a reduction of Mn from 0.45 to 0.10% produced both an increase in USE and a lowering of the ITT, Figure 18. A reduction in Ni from approximately 3.3 to 2.3% produced a further slight increase in USE and reduction in ITT.

Summary

This work has clearly demonstrated that considerable benefits can be gained through optimisation of the composition of gun steel. However reductions in C, Mn and Ni will all reduce hardenability so that it may not be possible to fully utilise these benefits in thick sectioned barrels/gun components, the current requirement being to harden through section sizes of 100-125mm.

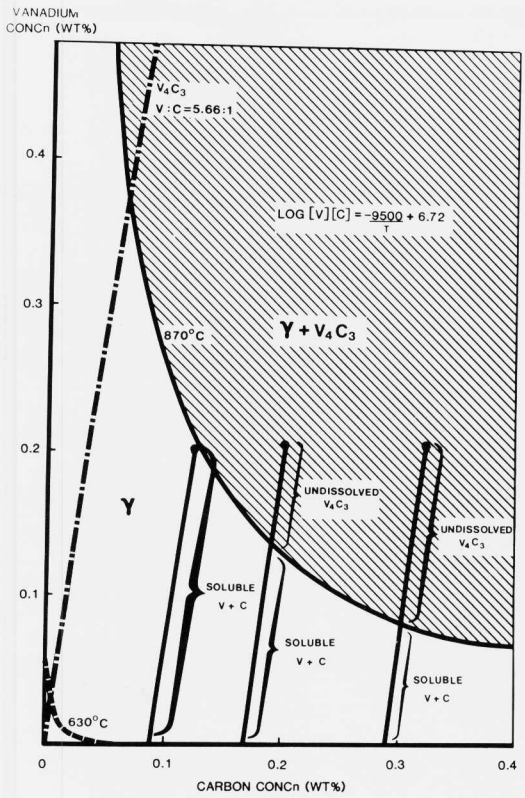

FIGURE 16. Solubility data for V_4C_3 in austenite for 3¼Ni Cr Mo V steel.

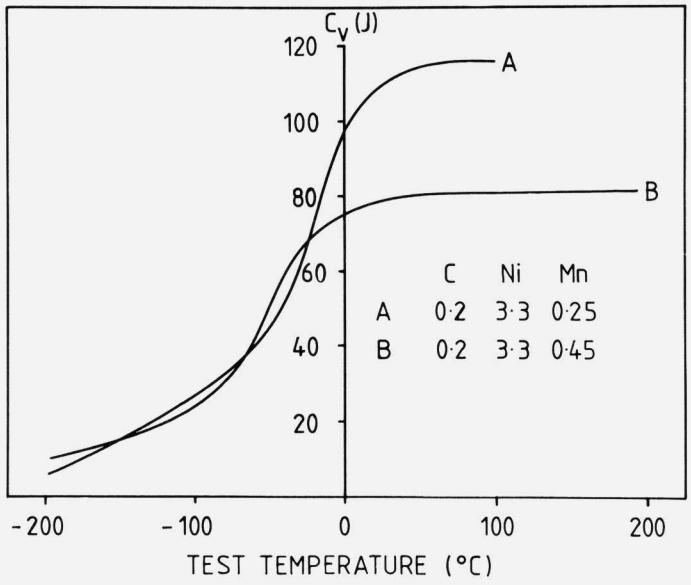

FIGURE 17. The influence of Mn on the impact properties of 0.2%C gun steels.

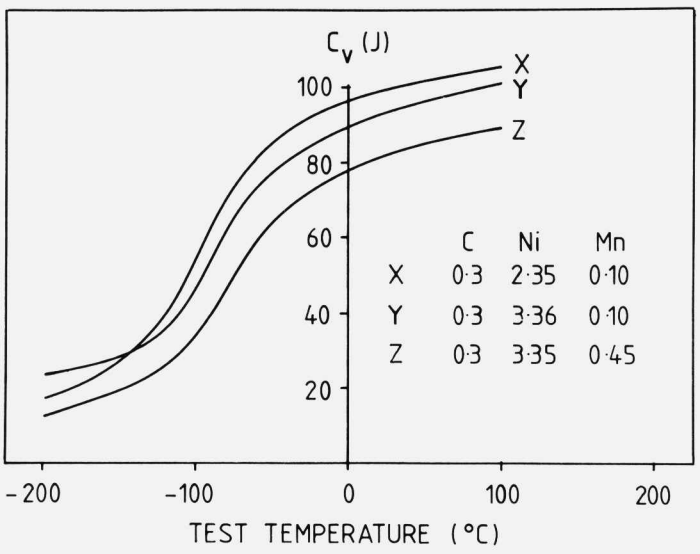

FIGURE 18. The influence of Ni and Mn on the impact properties of 0.3% gun steels.

Provided a low C, Ni, Mn gun steel has the required hardenability it offers an attractive improvement in toughness at the strength levels currently used. However it is unlikely that such a steel could be considered for future high pressure gun designs. The upper practical proof strength limit for such a low C steel will be approximately 1100-1150MN/m^2 as higher strength levels would require the use of unacceptably low tempering temperatures. Even with conventional gun steel with a 0.3-0.4% content, the maximum practical proof strength is approximately 1250-1300MN/m^2 as higher strength levels would again require the use of low tempering temperatures and impact toughness would be adversely affected, Figure 19. From this it is obvious that for strength levels in excess of ≈1300MN/m^2 alternative steels will be required, particularly if such strength levels are required in section sizes over ≈150mm. The development of alternative gun steels is discussed in the final part of this paper.

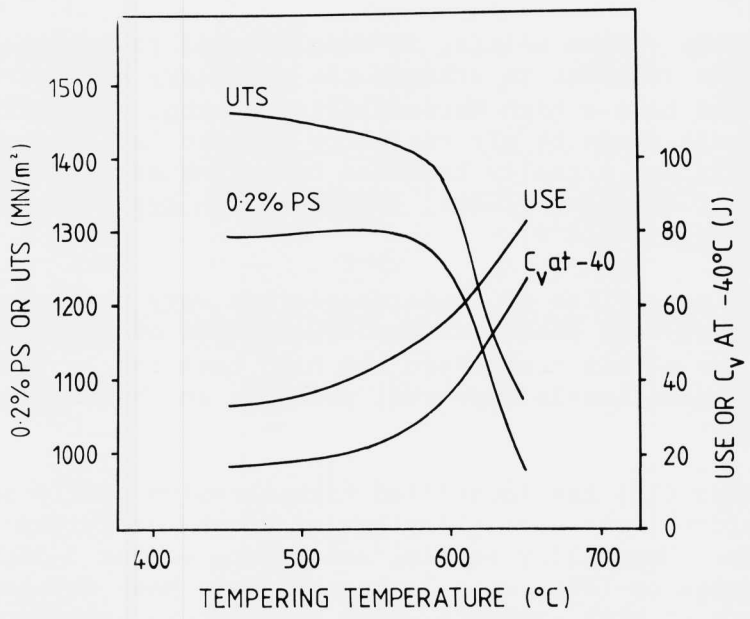

FIGURE 19. Tempering curve for 3¼Ni Cr Mo V steel.

THE DEVELOPMENT OF ALTERNATIVE GUN STEELS

The requirement for a steel capable of achieving proof strengths in excess of 1300MN/m^2, with a high transverse toughness at -40°C, in section sizes over ≈150mm, coupled with the necessity for tempering temperatures to be greater than 450°C, is one that can only be met by a limited number of steels. This stringent requirement obviously necessitates the use of high alloy steels.

Maraging steels are obvious candidate materials, but contain expensive alloying elements.

The maraging steels were developed to superimpose an age-hardening, strengthening mechanism onto a low interstitial content Fe-Ni martensite. As the carbon content is low (<0.03%), maraging steels have an excellent combination of strength and toughness. The steels are readily hot or cold worked and have good machinability. Such steels contain large additions of Ni, Mo and Co and hence are expensive. Mo and Co are strategic elements and in addition Co has a long radioactive half life.

Double vacuum melting is usually used to produce maraging steels in order to achieve the necessary high purity. The steels have a high hardenability so that even large section sizes can be air cooled to produce lath martensite. The steels are normally hardened by ageing at ≈450-480°C. A range of maraging steels, together with typical properties, are shown in Table 6.

The properties of these steels are very promising and there is obvious potential for development of such steels for use as gun steels - provided the high cost can be tolerated and toughness levels improved, probably at the expense of strength.

Keown (16) has identified high chromium steels as an alternative lower cost alloy system worthy of further investigation. Many alloy steels, containing either 3-5%Cr with high carbon or 12%Cr with low carbon, have been developed for a variety of high strength, high temperature applications.

Steels with 3-5%Cr Mo V have been independently developed over many years as tool steels[17], e.g., H13, H11, or as engineering alloys[18], e.g., BS970: 897M39, HST 100. The hot work tool steels are austenitised at relatively high temperatures, typically 1030°C, and double tempered at ≈565°C. The steels have high hot strength, good thermal shock resistance and

TABLE 6.

COMPOSITION AND MECHANICAL PROPERTIES OF TYPICAL MARAGING STEELS

STEEL	COMPOSITION (WT%)							0·2%PS (MN/m²)	A (%)	C_V (J)	TEST TEMP. (°C)
	C	Ni	Mo	Co	Al	Ti	Cr				
18%Ni	<0·02	18	5	9	0·15	0·6	-	1950	11	20	20
20%Ni	<0·02	20	-	-	0·25	1·5	-	1700	11	23	20
25%Ni	<0·02	25	-	-	0·25	1·5	-	1700	11	-	-
HY180	0·1	10	1	8	-	-	2	1275	19	129	-18
9Ni-4Co	0·25	9	-	4	-	-	-	1275	-	54	20

wear resistance but relatively poor toughness at lower temperatures. In contrast, the engineering grades are austenitised at lower temperatures, typically 930°C, and single tempered at high temperatures, ≈625°C, to give a good combination of yield strength and toughness.

Steels with 12%Cr Mo V have been optimised for creep-resisting applications at elevated temperatures with little concern for either yield strength or toughness at lower temperatures. These steels are typically heat treated at high austenitising and tempering temperatures, 1025 and 625°C respectively, to give maximum creep strength with adequate creep ductility and room temperature properties.

The high chromium steels were developed over 30 years ago before physical metallurgy concepts of grain refinement, solubility product, stoichiometry and low inclusion content were fully appreciated. The application of such concepts to these steels should lead to improved combinations of properties. It has already been shown[19] that improved toughness can be readily achieved with 12%Cr Mo V steels by lowering the austenitising temperature to produce finer grain steels.

The application of stoichiometry to a range of commercial high chromium steels demonstrated that all were lean with respect to carbon, Table 7. The powerful influence

of chromium in the 12%Cr Mo V low carbon steels was omitted because a large amount of the Cr enters into the cementite as $(FeCr)_3C$[20]. These calculations indicate that there is scope to either increase carbon or to decrease alloying elements such as vanadium to establish stoichiometric balance. Consideration has been given to vanadium carbide solubility calculations in order to balance the soluble/insoluble V_4C_3 by controlled heat treatment. By this means it should be possible to control both grain size and precipitation to produce the optimum combination of strength and toughness. This has highlighted possible alternative heat treatments to those normally given to these steels, Table 8.

TABLE 7.

STOICHIOMETRIC CALCULATIONS FOR A RANGE OF COMMERCIAL HIGH CHROMIUM STEELS

STEEL	TYPICAL COMPOSITION (WT%)					STOICHIOMETRIC C (WT%)
	C	Cr	Mo	V	Ni	
5% Cr Mo V	0·39	5·12	1·36	0·5	-	0·48
HST 140	0·4	5	2·0	0·4	-	0·49
H 13	0·4	5·3	1·4	1·0	-	0·58
12% Cr Mo V	0·12	12	2	0·3	-	0·18
JETHETE M152	0·12	11·7	1·93	0·33	2·28	0·18

The results indicate that the only feasible technique of improving the toughness of commercial 12%Cr Mo V steels is to lower the austenitising temperature. However, even using the normal austenitising temperature, these steels fail to meet the strength requirements being aimed for and a reduction in the austenitising temperature will further reduce the yield strength. This indicates that there is no readily available 12%Cr Mo V low carbon steel that will meet the required specification. With the 12%Cr Mo V steels the obvious alternative is to use alloy development, especially to increase the carbon level, to achieve the desired strength level.

TABLE 8.

HEAT TREATMENT PARAMETERS FOR COMMERCIAL HIGH CHROMIUM STEELS

STEEL	NORMAL HEAT TREATMENT (°C)	CALC. AUSTENITISING TEMPERATURE× (°C)
5 % Cr Mo V	1030/OQ + 600/AC + 600/AC	900
HST 140	1050/OQ + 550/AC	920
H 13	1050/OQ + 400/AC	925
12 % Cr Mo V	1050/AC + 650/AC	955
JETHETE M152	1050/AC + 650/AC	875

× Ac_3 + 50°C
OQ OIL QUENCH
AC AIR COOL

A programme of work is under way to evaluate the effects of this approach on the properties of commercial 5%Cr Mo V and higher carbon 12%Cr Mo V steels.

In applying solubility concepts to the 5%Cr Mo V steel it was assumed that the precipitating species was V_4C_3 in the absence of firm identification. It is possible that a complex precipitation sequence of M_2X, M_7C_3 and V_4C_3 is occurring with undissolved V_4C_3 precipitate particles controlling the austenite grain size. Transmission electron microscopy and microanalysis work is in progress to identify the precipitates which also could include alloy-enriched cementite. With no solubility data available for M_2X and M_7C_3 the solubility product for V_4C_3 in austenite was used, Figure 20, to determine the austenitising temperature for the steel to achieve grain control from undissolved carbides. Austenitising temperatures of 900, 975 and 1050°C, were used to produce proportions of insoluble/soluble carbides of $^2/_3$, $^1/_3$ and 0 respectively. Complete tempering curves, Figure 21, were determined to show the secondary hardening and over-ageing reactions. Data for conventional 3½Ni Cr Mo V gun steel is also included in Figure 21 which shows the superior strength of the 5%Cr Mo V steels. The secondary hardening reaction is not pronounced but obviously precipitation

reactions are contributing to retarded softening. It may also be seen that the ageing reaction occurs at a lower temperature than with conventional gun steel.

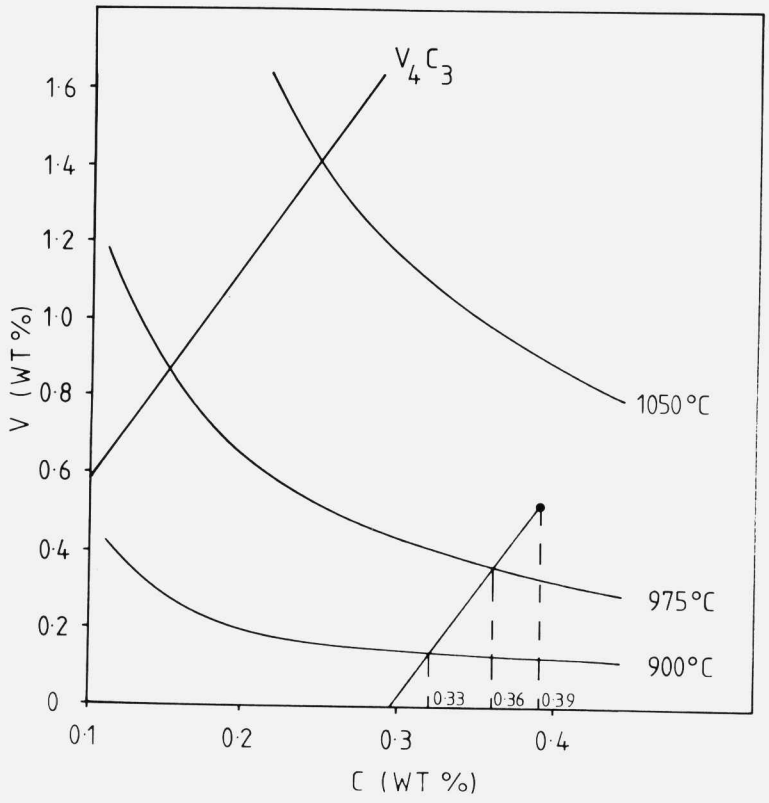

FIGURE 20. Solubility data for V_4C_3 in austenite for 5%Cr Mo V steel.

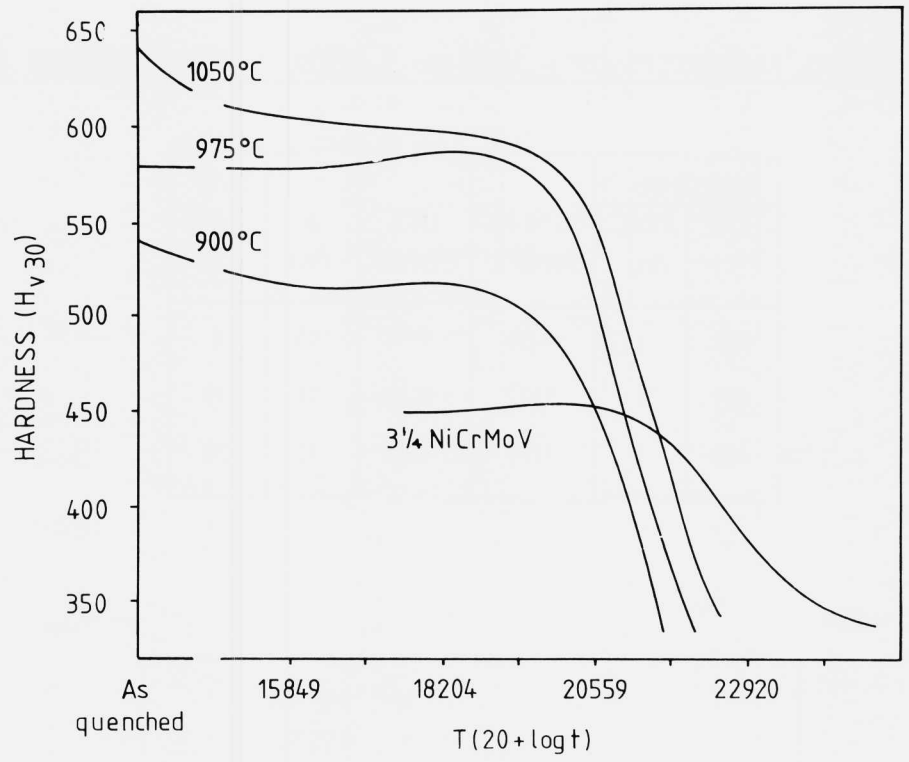

FIGURE 21. Tempering curves for 5%Cr Mo V steel.

Specimens austenitised at 975°C and tempered at 600, 615 and 630°C for 1 hour were selected for tensile and impact testing, the results being summarised in Table 9. The results demonstrate that the strength requirement has been attained. The impact results fall short of the requirement of 40J at -40°C and complete impact transition curves indicate a low upper shelf energy, possibly because of the presence of stabilised alloy-enriched cementite. The current electron microscopy investigations should clarify this point. Additional work on grain size control, steel chemistry and precipitation mechanisms is in progress to further optimise the mechanical properties.

With the 12%Cr Mo V steel again the lack of solubility data on M_2X and $M_{23}C_6$ precipitation has precluded precise solubility predictions of austenite grain control by undissolved precipitate particles. Using V_4C_3 data, Figure 22, as a guide austenitising temperatures of 875, 900 and 925°C were established for $^{2}/_{3}$, $^{1}/_{3}$ and 0 proportions of undissolved carbide. Although unsatisfactory, this approach does give some indication of the carbon in solution and its effect on

TABLE 9.

MECHANICAL PROPERTIES OF A 5%Cr Mo V STEEL AUSTENITISED AT 975°C

TEMPERING		0·2% PS	UTS	A	C_v at
TEMP. (°C)	TIME (hr)	(MN/m²)	(MN/m²)	(%)	-40°C (J)
600	1	1455	1784	10	8
615	1	1322	1585	11	13
630	1	1177	1409	12	28

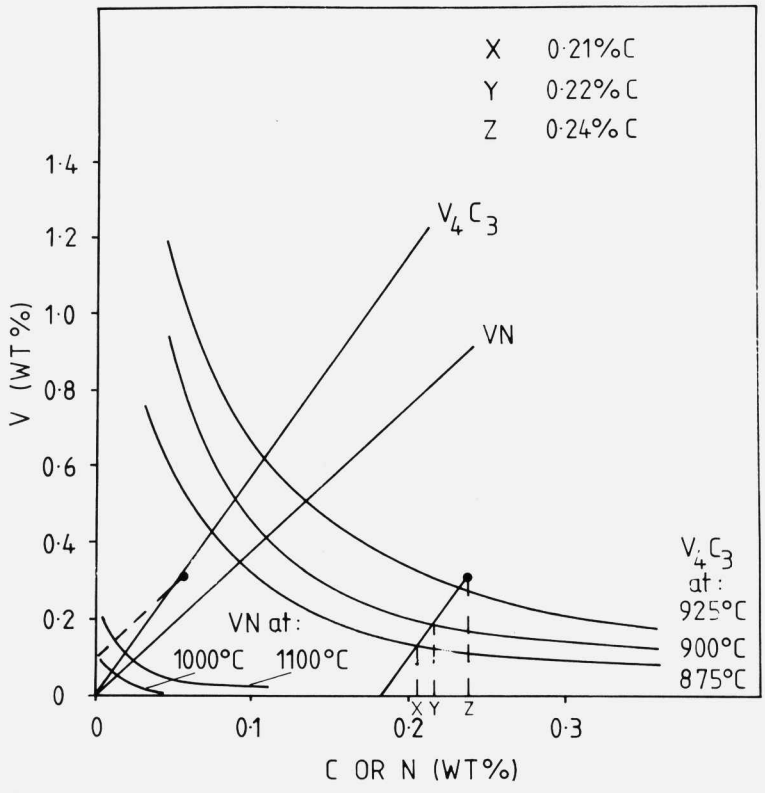

FIGURE 22. Solubility data for V_4C_3 in austenite for 12%Cr Mo V steel.

base hardness as shown by the tempering curves, Figure 23. As with the 5%Cr Mo V steels, the strength of this steel is superior to the conventional gun steel despite its lower carbon content. Mechanical property and electron microscopy investigations are being carried out on samples aged at 550, 600 and 650°C.

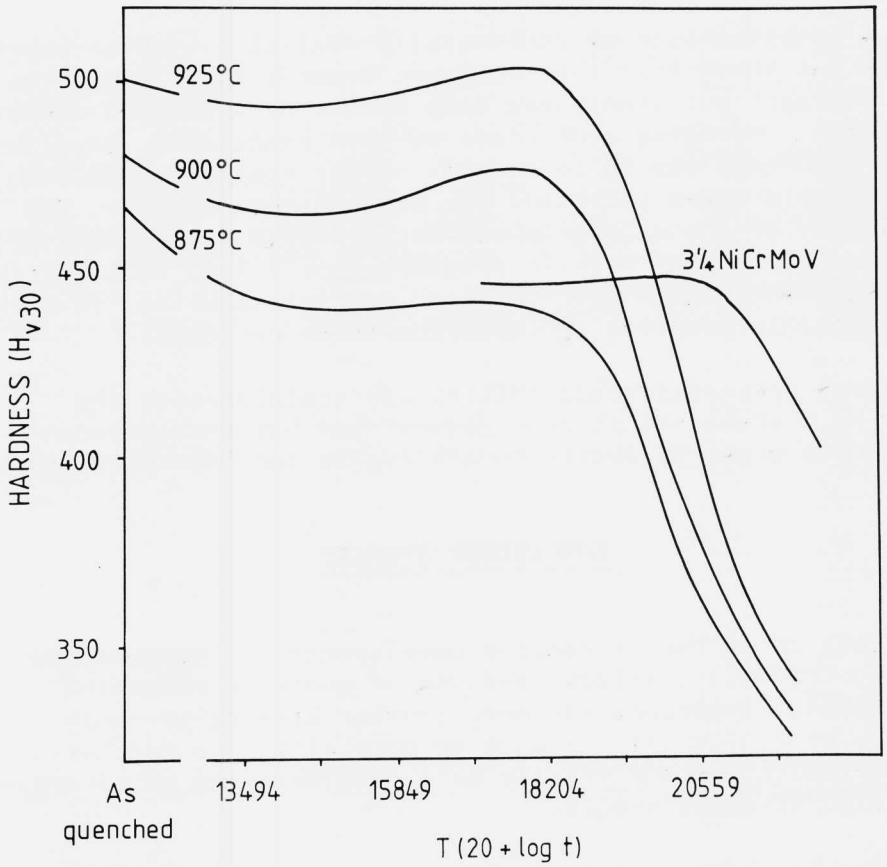

FIGURE 23. Tempering curves for 12%Cr Mo V steel.

A major problem that has arisen in the development of higher strength in this 12%Cr Mo V steel has been the unforeseen but important influence of nitrogen on the precipitation processes and mechanical properties. The experimental steel was based on existing 12%Cr Mo V steels but with an increased carbon content for extra strength. The high nitrogen content of the commercial alloys, 0.05%, was retained. Subsequent solubility considerations have shown that the lower solubi-

lity of vanadium nitride (VN) effectively reduces the amount of V available for precipitation as a carbide or carbo-nitride during tempering, Figure 22. For example if VN precipitates down to 1100°C there will be only 0.1%V available for precipitation as V_4C_3 or other phases on tempering. Further experimental melts, with lower nitrogen contents, are now being studied.

Summary

A consideration of commercially available high strength steels has shown that the stringent demands for alternative high strength gun steels can only be met by a limited number of steels. Maraging steels are obvious candidates, provided their high cost can be tolerated. Lower cost 5 or 12%Cr Mo V based steels offer potential for further development. The complexity of the alloys is preventing rapid development but electron microscopy work in progress should lead to a better understanding of the precipitation mechanisms which, in turn, should enable property optimisation to be achieved.

With increased hardenability and stainlessness the 12%Cr Mo V steel offers other advantages but the optimum properties might be easier to achieve in the 5%Cr Mo V steel.

CONCLUDING SUMMARY

This paper has traced the development of improved gun steels, initially, through the use of modern steelmaking techniques, to produce cleaner, tougher steels; secondly, through stoichiometric balance of composition to further improve toughness; and finally to a consideration of alternative high strength steels.

The toughness level of the traditionally used Ni Cr Mo (V) steels can be considerably improved through the use of electro slag refined steel. For maximum benefit it has been found essential to use clean, high quality electrodes for remelting. Further improvements in the toughness levels of this steel can be achieved through a reduction in the C, Ni and Mn contents although it is likely that hardenability will be adversely affected.

To meet the anticipated demands of the designers for future tank guns will require the use of alternative, higher alloy steels. The stringent demands can only be met by a limited number of steels and even these require optimising.

Work is in hand to optimise composition, heat treatment and mechanical properties of high Cr Mo V steels containing 5 or 12%Cr.

REFERENCES

1. A. R. Cox, B. D. Goldthorpe, J. Morris & D. T. Richards. MOD(PE) Unpublished Report, 1973.

2. Ministry of Defence. Defence Standard 10-13 Issue 2, 31 December 1976.

3. H. J. Wagner & K. Bar Avi. Metals Technology, November 1979, pp. 420-423.

4. R. Hawkins. AOD as an Alternative to ESR for the Production of High Quality Steel. Paper Presented at SCANINJECT IV, 4th International Conference on Injection Metallurgy, Lulea, Sweden, June 1986.

5. J. M. Barsom & S. T. Rolfe. Impact Testing of Metals. ASTM STP466, American Society for Testing and Materials, Philadelphia, 1970, p. 281.

6. R. Hawkins & B. D. Goldthorpe. MOD(PE) Unpublished Report, 1982.

7. Ministry of Defence, Defence Standard 10-13 Issue 1, 29 July 1968.

8. R. W. K. Honeycombe. Steels Microstructure and Properties. Met and Mat Sc Series Publ, E. Arnold, London, 1981.

9. F. B. Pickering. Physical Metallurgy and The Design of Steels. Allied Sci Publishers Ltd, Essex, 1978.

10. L. F. Porter & D. S. Dabkowski. Proceedings 16th Sagamore Army Materials Research Conference, New York, 1969.

11 W. Crafts & J. L. Lamont. Trans AIME, 180, 471, 1949.

12. R. Hawkins, T. D. Andrews & S. R. Keown. The Effect of Alloy Steel Design and Heat Treatment on Mechanical Properties of 3½Ni Cr Mo V Steel. Paper Presented at Australasian Inst of Metals, 1st National Heat Treatment Conference, Sydney, Australia, 27-29 August 1984.

13. K. Narita. Trans ISI Japan, 15, 145, 1975.

14. S. R. Keown, L. Taylor & R. Hawkins. To be published.

15. T. D. Andrews. MOD(PE) Unpublished Report, 1987.

16. S. R. Keown. MOD(PE) Unpublished Report, 1985.

17. G. A. Roberts & R. A. Cory. Tool Steels, 4th Edition, ASM, 1980.

18. J. D. Murray. ISI Special Report No 76, 1961, p. 41.

19. E. A. Little, D. R. Harries, F. B. Pickering & S. R. Keown. Metals Tech, 4, 205, 1982.

20. F. B. Pickering. Private Communication.

PROPERTIES AND APPLICATIONS OF ULTRAHIGH CARBON STEEL LAMINATES

R. D. CALIGIURI*[1], L. E. EISELSTEIN[2], O. D. SHERBY[3]
(1) Defense System Group, Failure Analysis Associates, Palo Alto, California 94303; (2) Metallurgy and Fracture Mechanics Department, SRI International, Menlo Park, California 94025; (3) Department of Materials Science and Engineering, Stanford University, Stanford, California 94305.

INTRODUCTION

Research over the past ten years at Stanford University, SRI International, and Failure Analysis Associates has demonstrated the feasibility of using diffusion bonding, roll bonding, or explosive welding techniques to fabricate laminated composites consisting of two or more layers of ferrous-based alloys with widely different properties. Specifically, it has been demonstrated that ultrahigh carbon (UHC), high-strength steels can be laminated (up to 300 layers) to lower carbon, higher toughness, ferritic or austenitic steels. The bonding parameters can be adjusted to yield interface conditions ranging from a perfect metallurgical bond to no bond at all. These all-metallic laminate composites can exhibit superior tensile and Charpy V-Notch properties relative to conventional monolithic high-strength steels, depending on component properties, heat treatment, and interlayer bond strength. In addition, certain of these laminate configurations can exhibit superplasticity at warm (500 to 800°C) temperatures, suggesting excellent formability for such laminates.

Applications for this technology that are currently under exploratory development include advanced all-metallic laminate armor systems for both heavy and lightweight vehicles, high strength/high toughness laminated cases for hardened target penetrators, bimetallic liners for shaped charges and explosively formed penetrators, and corrosion resistant cladding.

In this paper, we review the development of this technology, describe in detail the interesting properties of these laminates, and discuss the current status of some potential applications.

BACKGROUND ON ULTRAHIGH CARBON STEELS

UHC steels are plain carbon steels containing 1.0 to 2.1% C (15-32 vol.% cementite). Traditionally, steels of this high carbon content have been neglected by industry because of a belief that they are inherently brittle. Since the mid 1970s, UHC steels have been considered to have technological potential (1-5) because, when processed to develop ultrafine ferrite grains, 0.5-2 μm, stabilized by fine spheroidized cementite particles, they have been shown not only to be superplastic at intermediate temperatures, but also to be strong and ductile at room temperature (6-12). Further, because of their high carbon content, these steels can be made very hard (R_C = 65-68) by appropriate heat treatment after processing (13). Fine-grained UHC steels can also be solid state diffusion bonded readily either to themselves, or to other ferrous-base materials, at temperatures below the A_1 temperature (14) as shown in a historical example (Figure 1). This unique ability has been utilized to prepare ferrous laminated composites with superplastic properties at intermediate temperatures (15-17) and with very high impact resistance at low temperatures (17-19).

Superplastic Formability of UHC Steels

The original work on UHC steels demonstrated that superplasticity could be developed over the range of composition from about 0.87 to 2.1%C and the range of temperature from 650 to 800°C (8,9). This temperature range is from just below the A_1 temperature (727°C) to just above it. Furthermore, superplasticity was observed at intermediate strain rates (10^{-5} to $10^{-3}s^{-1}$). An overview of the expansion in composition and temperature ranges now

available for superplasticity in UHC steels is shown in Reference (20).

The commercial application of superplastic forming of UHC steel would be enhanced if superplasticity could be achieved at strain rates higher than $10^{-3}S^{-1}$. There are two methods of achieving such a goal: 1) by maintaining a fine grain size at higher thermomechanical processing temperatures, or 2) by decreasing the grain size, thereby making superplastic flow by grain boundary sliding at a given temperature more facile. It was discovered that the first method could be utilized in UHC steels by dilute alloying with silicon (20,21).

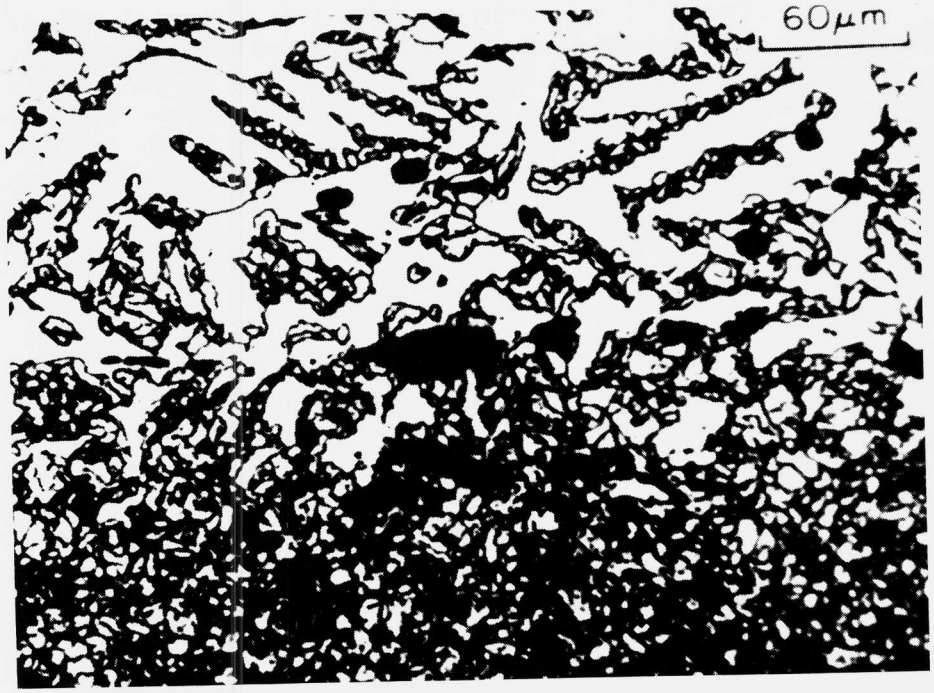

FIGURE 1: Example of an Adze blade, ca. 400 B.C. consisting of a medium carbon edge and a low carbon iron.

Silicon influences the thermodynamics of the Fe-C system and the kinetics of carbide formation and dissolution. Si is a known ferrite stabilizer and therefore increases the A_1 temperature of Fe-C alloys; this increase results in a wider ferrite

temperature range over which superplastic flow is possible relative to plain carbon UHC steels. Furthermore, because the carbon content on the eutectoid composition decreases with Si additions, Si increases the quantity of proeutectoid carbides. For this reason, there is an increase in the volume fraction of carbides available for grain boundary pinning in the austenite plus cementite range. Superplastic flow in austenite can thus now be expected, a property difficult to achieve in plain carbon UHC steels because rapid grain growth occurs in austenite. Thus the temperature range for superplastic flow is predicted to be increased with UHC-Si steels.

The effect of silicon on the microstructure of UHC steels is dramatically illustrated in Figure 2. In this example, a UHC steel containing 3.0% Si was metallurgically bonded to nominally the same UHC steel without silicon, and then held at 770° for 48 hours. The UHC steel without silicon clearly shows evidence of extensive carbide dissolution, whereas the UHC steel containing silicon appears unaffected by the excursion into the nominally austenite region.

In addition to improving the temperature range over which superplastic flow should be obtained, Si also inhibits grain growth of ferrite grains during superplastic deformation below the A_1 temperature. This is because Si inhibits carbide particle growth, and hence ferrite grain growth (controlled principally by carbide particle coarsening) is reduced. Another benefit of Si is that it dissolves in the ferrite or austenite matrix of iron. The hardness of the carbides is therefore unaffected since Si does not contribute to the structure of the carbides. An increase in hardness of the carbides could be deleterious to superplasticity (22). As a solid solution strengthener, however, Si can be expected to make slip processes more difficult during superplastic deformation, thereby extending the range of strain rate over which grain boundary sliding (superplastic flow) dominates deformation (22).

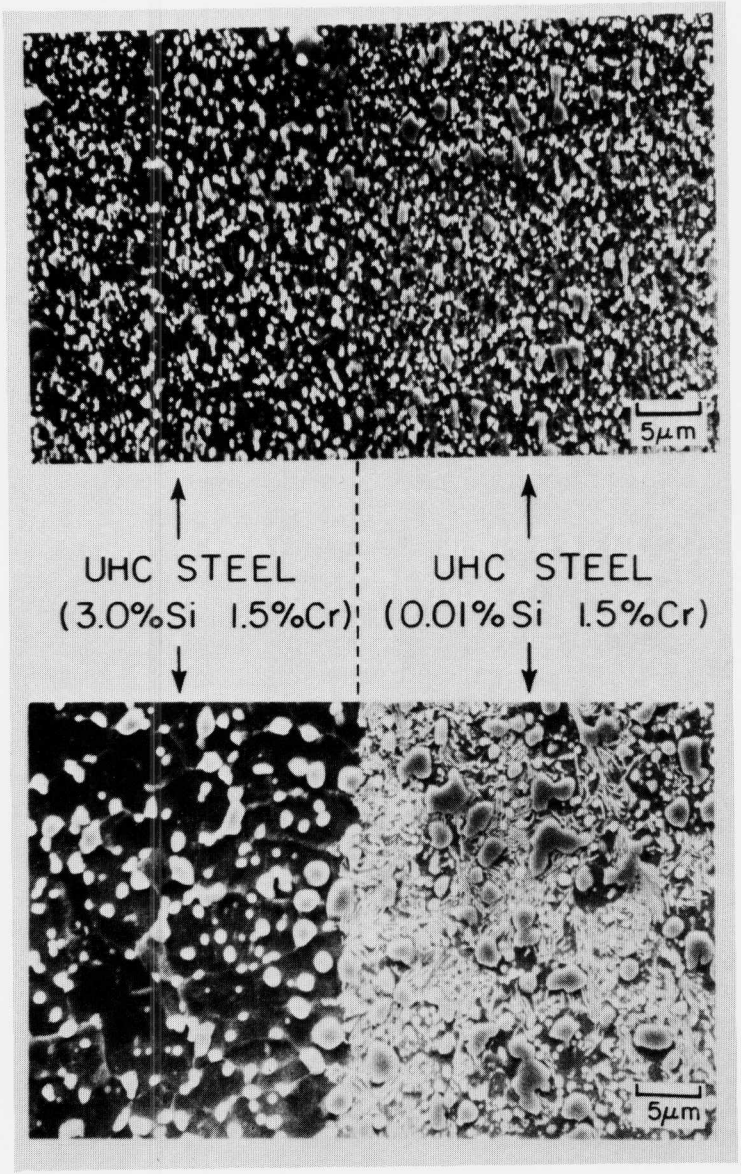

FIGURE 2: The interface region in laminate which consists of 1.25% UHC steels, with 3% Si in the left layer and 0.01% Si in the right layer. (a) The microstructure is seen to be similar in the two layers after roll bonding at 650°C; (b) The microstructure of the same laminate after heat treatment at 770°C for 48 hours followed by air cooling. Note that carbon diffusion during heat treatment led to drastic changes in microstructure yet maintained a discrete interface.

UHC Steel Laminated Composites

A key attribute of UHC steels is that they can be solid state bonded either to themselves or to other ferrous materials at temperatures below the A_1 temperature (14). This property is significant for several reasons. First, the low bonding temperature means that ferrous laminated composites can be prepared without destroying the desired fine structure in the UHC steel. Second, laminated composites of UHC steel can be prepared to permit selective heat treatment; e.g., the UHC steel can be transformed to martensite of exceptional hardness, leaving the other component unaffected (14). Finally, joining of UHC steels by solid state bonding techniques is readily achieved.

High impact strengths have been obtained in laminated composites, the components of which exhibit lower impact strengths than the laminate. An example of such impact behavior for a UHC-steel/mild-steel composite is illustrated in Figure 3. The notch impact strength of the laminated composite is much higher than that observed either for the mild steel or for the UHC steel. Furthermore, the impact transition temperature for the laminated composite is very low, about -140°C, much below that for either of the components that makes up the composite. The high impact resistance of the laminate composite is due to the presence of a good (but not perfect) bond between laminates. If the bond strength is improved, e.g., by a thermal cycle heat treatment, the impact strength is degraded (19).

A laminated composite consisting of a superplastic and nonsuperplastic component can be made to exhibit superplastic behavior. A UHC steel-mild steel laminated composite has been shown to exhibit strain rate sensitivity exponents of over 0.30 and elongations to fracture of over 400% (15-17). The strain rate-stress results show good agreement with constitutive equations for creep which have been developed based on an isostrain creep deformation model. The equations lead to quantitative predictions of material requirements for achieving ideal superplasticity ($m = 0.5$) in laminated composites based on UHC steel. A laminated composite consist-

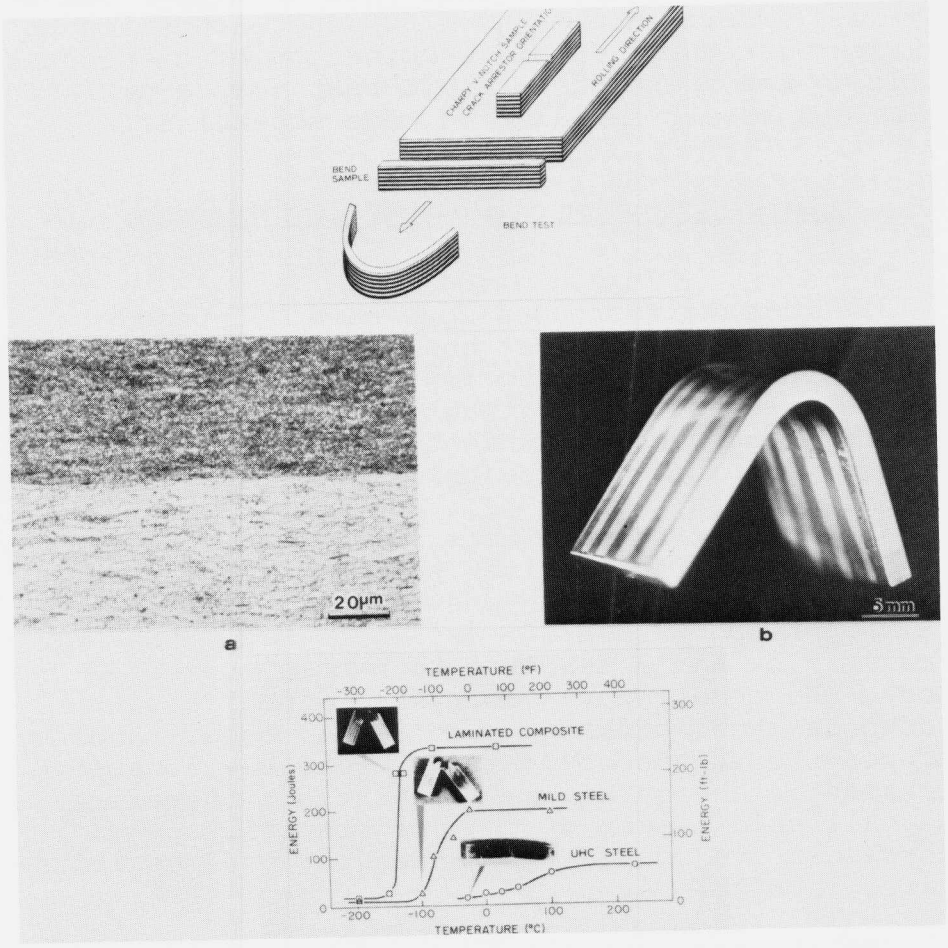

FIGURE 3: [Top] Orientation of mechanical test samples taken from a laminated composite of UHC steel and 1020 steel. [Center] (a) Optical photomicrograph of interface in laminated composite of UHC steel and 1020 showing an excellent metallurgical bond; (b) bend test sample of the laminated composite. [Bottom] Impact properties of UHC steel, 1020 steel, and UHC steel/1020 steel laminated composites including photographs of the tested samples.

ing of a ferritic, stainless-steel-clad, ultrahigh carbon steel is predicted to exhibit ideal superplasticity at 800°C. Studies by Daehn, Kum, and Sherby (23), demonstrate that this condition can be achieved experimentally (m = 0.5 and elongation to failure over 800%). This combination of components leads to the unexpected result that coarse-grained stainless steels can also be made superplastic.

LAMINATED METAL FOR ARMOR APPLICATIONS

Monolithic ferrous alloys have been used extensively as armor over the years because of their good properties and low cost. However, the increased severity of threats, coupled with the need to reduce vehicle weight, has made it necessary to increase the ballistic efficiency of metallic armors. It is well documented that, as the strength of steel armors increases, so does the ballistic limit for a given target thickness (24). Unfortunately, when the tensile yield strength of the target approaches 175 ksi (1200 MPa), the plastic flow has a tendency to become localized around the penetrator. This shear localization (known as shear banding or adiabatic shear banding) reduces the volume of material available to absorb the kinetic energy of the penetration; therefore, the ballistic limits of the targets start to decrease above some target strength level as illustrated in Figure 4.

As the strength levels increase further, the shear localization becomes more and more extreme and eventually little plastic flow or plastic bending of the plate occurs to consume the kinetic energy. Only the energy required to propagate shear banding in a highly localized annular region surrounding the penetrator is absorbed. This shear localization mechanism continues and increases in severity until the strength of the steel armor starts to approach a hardness or strength level at which it can begin to fracture the projectile. In steels, this projectile fracture process initiates at tensile strength levels of about 270 ksi (1,850 MPa). As the armor plate becomes even stronger, the projecile becomes more effectively fractured

and the ballistic limit starts to increase again (24). Unfortunately, when the strength is increased beyond a hardness of about 550 BHN, a brittle fracture mode in the ferrous target is activated, thereby shattering the target and reducing ballistic performance. This shattering effect in a UHC steel hardened to in excess of 600 BHN is illustrated in Figure 5.

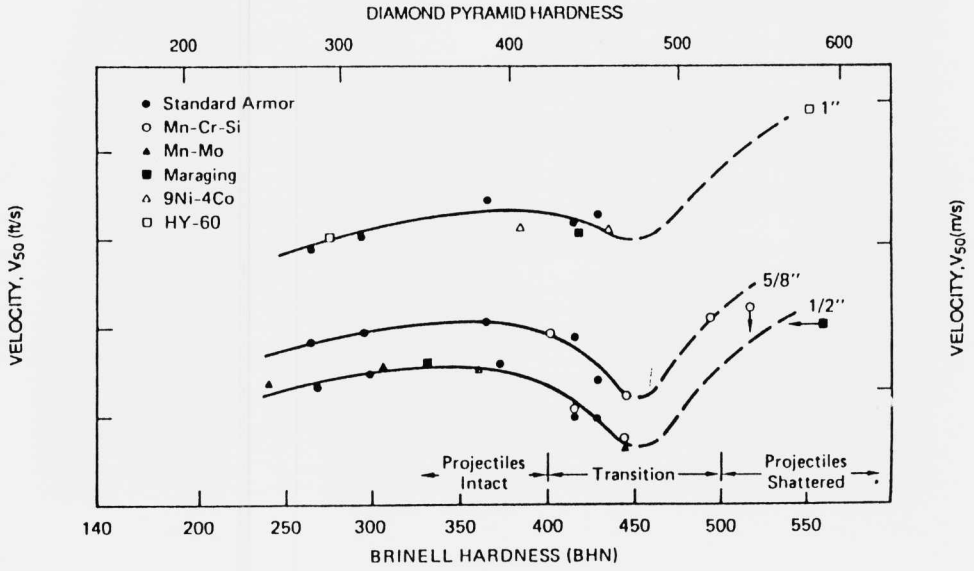

FIGURE 4: Ballistic limit (V_{50}) of steel armors as a function of areal density and obliquity.

To overcome some of the problems associated with monolithic steels, and to use the strengths to best advantage, multilayer, all-metallic laminated composites are being investigated for various components of a hybrid heavy armor package in current programs under way by Honeywell, Failure Analysis Associates, and SRI International (25). These composites consist of alternating layers of at least two materials metallurgically bonded to one another. After bonding and any required fabrication, the composite is heat treated to selectively harden one or more of the components to a very high

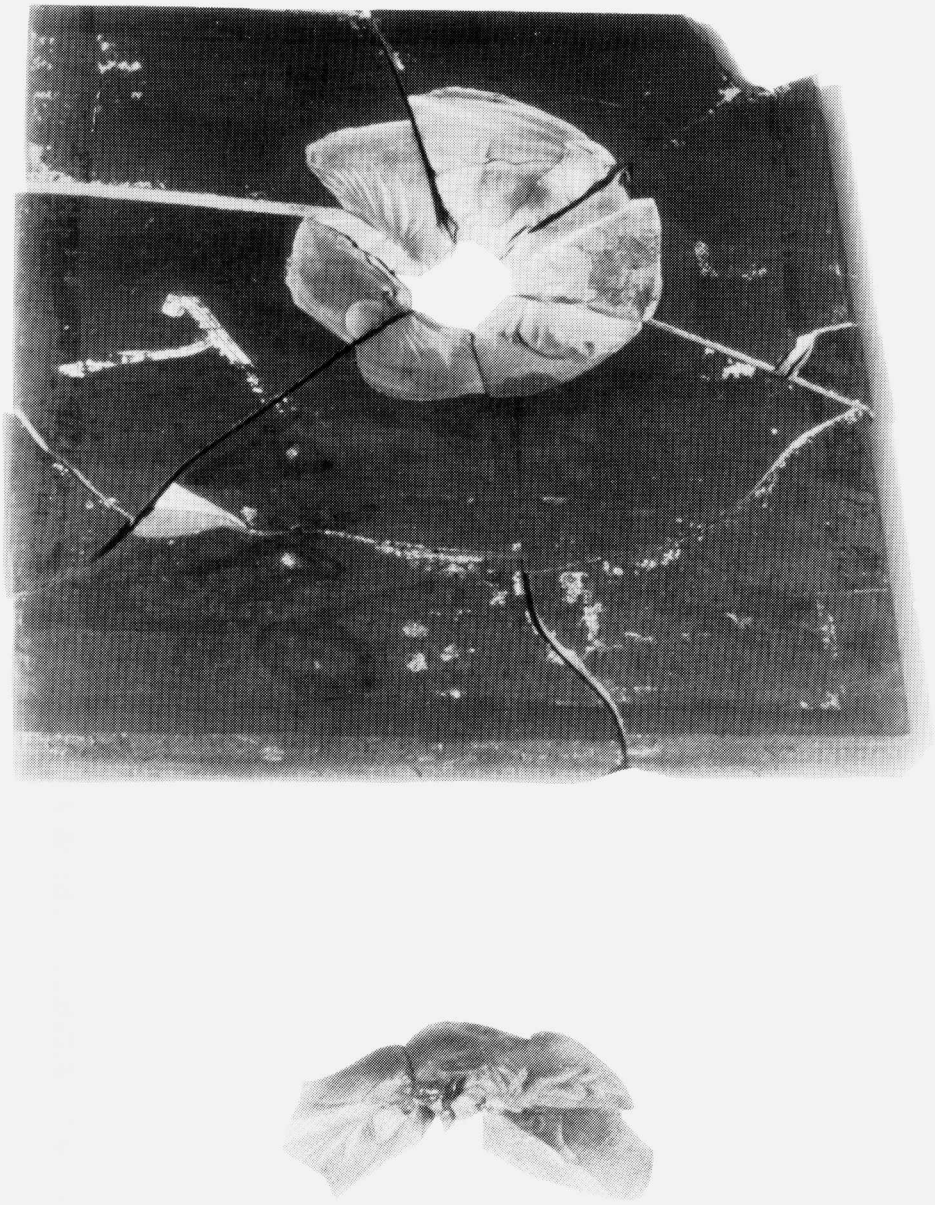

FIGURE 5: Brittle, radial, and conoidal cracking of hardened UHC steels.

compressive yield strength. The hard, brittle components erode and fracture the projectile, whereas the soft, ductile components absorb kinetic energy, give the armor structural integrity, and minimize collateral damage to the hard, brittle material to enhance second-hit capability.

The metallic laminate design concept of placing a hard material on a softer material prevents shear localization from decreasing the energy-absorbing ability of the plate and allows harder front face materials to be used that much more effectively to fragment the projectile. While these harder materials cannot be used in monolithic form due to the lack of second-hit capability and the premature brittle fracture of the plates before the projectile is fragmented, when bonded to the softer component, their performance improves and good second hit capabilities result. The effect of lamination on the performance of metallic armor systems against a small caliber kinetic energy threat is summarized in Figure 6. The multi-hit capability of a UHCS metal laminate target against this threat is illustrated in Figure 7 (25).

In addition to defeating the projectile through erosion and fracture, these laminate composites can also absorb some of the kinetic energy of the projectile at impact velocities near the ballistic limit by a structural bending/plastic deformation mechanism, a mechanism generally not operative in ceramic composite armor systems. The components in these all-metallic laminate systems are also much less expensive than nonmetallic (e.g., ceramic) laminate systems. Furthermore, because the hardening is achieved after bonding and fabrication, these all-metallic laminate composites are much easier to join and shape.

While the geometry of the laminates (e.g., the order, relative thickness, and number of layers) influences the performance of metallic laminate systems, the most important variables influencing performance are the physical and mechanical properties of the hard and soft components. Therefore, in the following paragraphs we discuss the factors influencing the selection of the hard and soft components for metallic laminate systems.

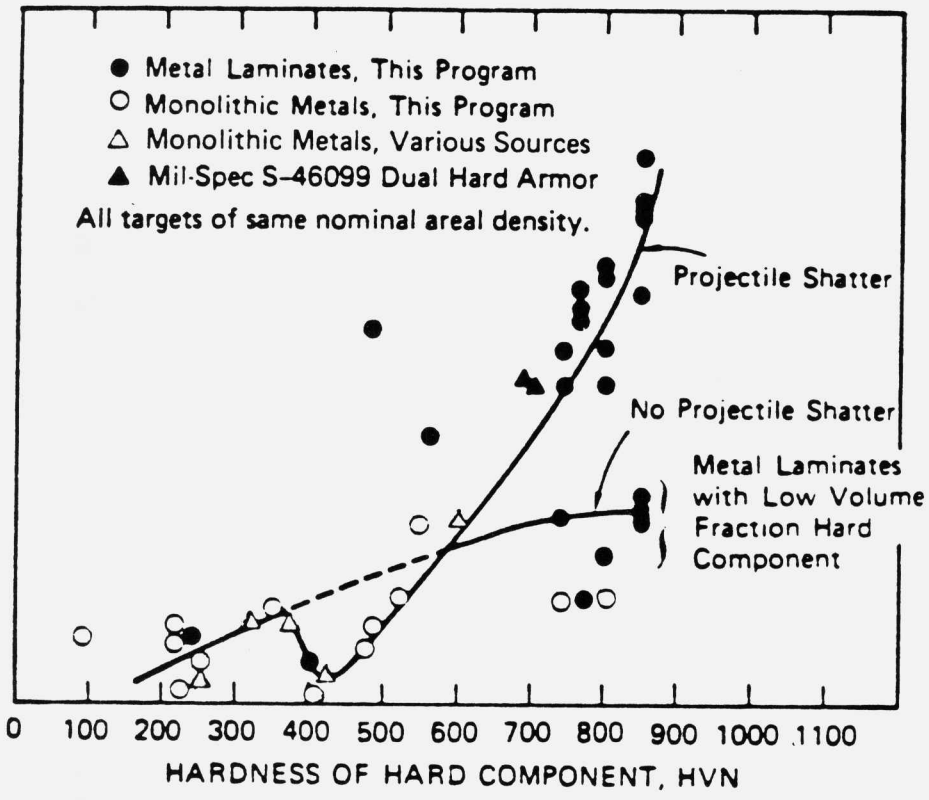

Figure 6: Ballistic Performance of Monolithic and Laminate Composite Targets Against 0.50-Caliber AP-M2 Projectile at 0° Obliquity.

Hard Components

Previous work on composite armor systems has established that materials with high hardnesses or yield strengths effectively break up and erode penetrators if these materials are properly supported and constrained from fracturing prematurely. That ceramic composites have consistently performed better than metallic composites may be due to the fact that the hard components of the metallic systems have not been high enough in the past. An example of such metallic laminate armor of marginal hardness is dual-hard armor (24). UHC steel, however, can be heat treated to high-hardness levels while still retaining some degree of

(a) Front of Target

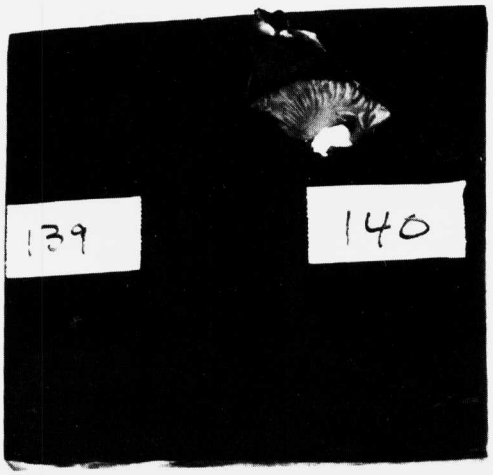

(b) Back of Target

FIGURE 7: Second-hit capability of 52125/A-710 laminates.

ductility. In Figure 8, the ultimate compression strength is plotted as a function of plastic compression ductility for several hard metals and UHC steel.

These data clearly show that the compression strength of the UHC steel is comparable to the strength of WC-12 wt% Co with considerably greater compression ductility. Figure 9 shows the energy-absorbing capability (assuming perfectly plastic behavior and no shear localization) for the various materials shown in Figure 8 as well as several other engineering materials, including ceramics (25). Clearly, the energy-absorbing capability of the UHC is much higher than that of both the cemented carbides and the ceramics, even though these materials are considerably stronger.

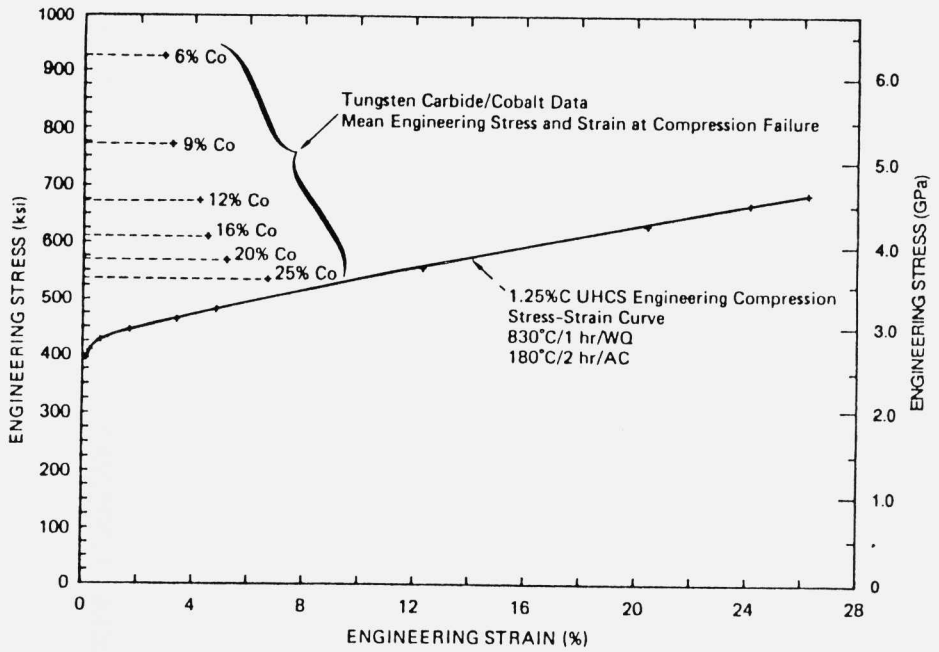

FIGURE 8: Compressive stress-strain relationships for hard materials.

Although it has not been shown that the ballistic performance increases with increasing plastic energy absorbing ability, Figures 8 and 9

illustrate three significant points. First, the ceramics are considerably stronger than the tool steel and the UHC steel, but their strain to failure and their ability to absorb energy when uniformly strained in compression are extremely low. The extremly high strength levels of the ceramics may not be necessary for good ballistic performance of laminated composites, and the

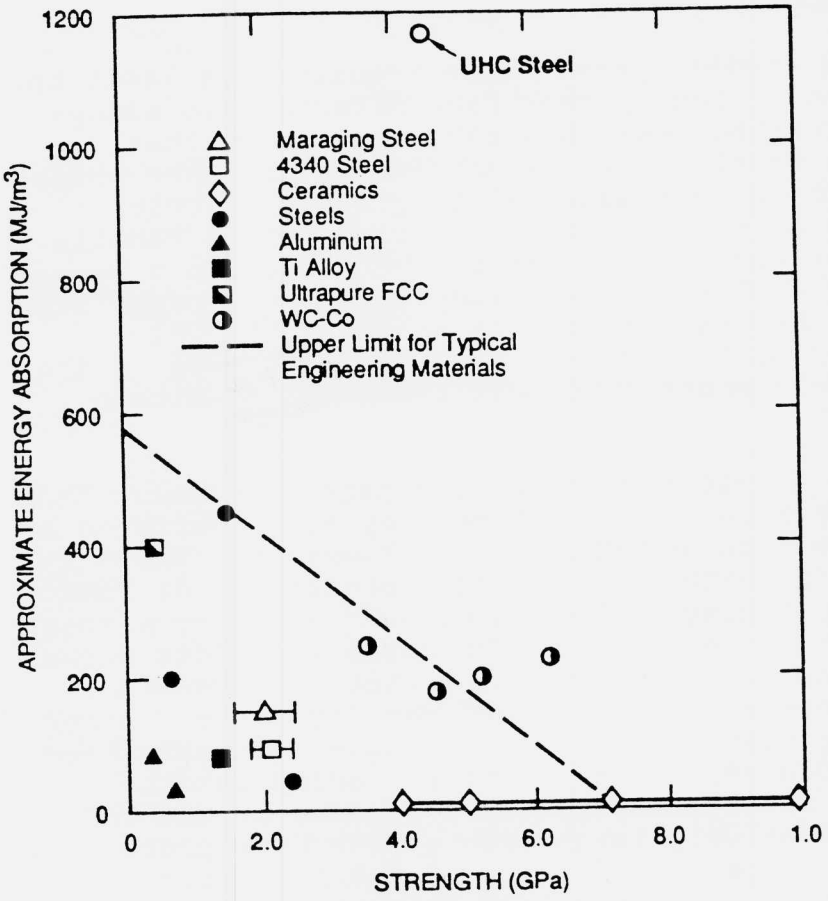

FIGURE 9: Approximate energy absorption by plastic work for engineering materials.

energy-absorbing advantage of these UHC steels over the ceramics can be effectively used if the laminates are properly designed. Second, the tool steels and UHC steels are as strong as some of the cemented carbides, and, therefore, are as strong as most current penetrator materials (26). Third, the UHC steels have strength and ductility properties that are as good as many of the more expensive types of tool steels and many grades of cemented carbide tooling material.

Soft Components

For steels, performance requirements limit the selection of tough, back face materials to alloys with strengths less than 250 ksi. Above this strength level, there is not enough fracture toughness left in most material to prevent brittle cracking of the back face material before kinetic energy is absorbed by plastic bending. In a recent study, 9-4-20 steel was selected for the back face material because of its reasonably high yield strength, ductility, and fracture toughness in its low-temper-temperature heat treatment condition (25).

The 9-4-20-backed UHC laminates typically bend a considerable amount before they are penetrated by the projectile and front face fragments. The 9-4-20 fails by either a tearing (petalling), or sometimes a plugging mechanism brought about by a shear localization mechanism. The overall failure mechanism appears to be similar to that observed in ceramic armors in this areal density range. After the front plate and projectile have been shattered to some degree, the projectile loading is distributed through the conoidal failing of the UHC over a relatively large area of the back plate material. The distribution of the ballistic loading over the large area helps to prevent shear localization and allows a larger portion of the target to absorb the projectile/projectile fragments kinetic energy through plastic bending and deformation of a much larger volume of material than would have been possible if the front face material did not fracture the projectile and dis-

tribute the load. These effects are illustrated in Figure 10.

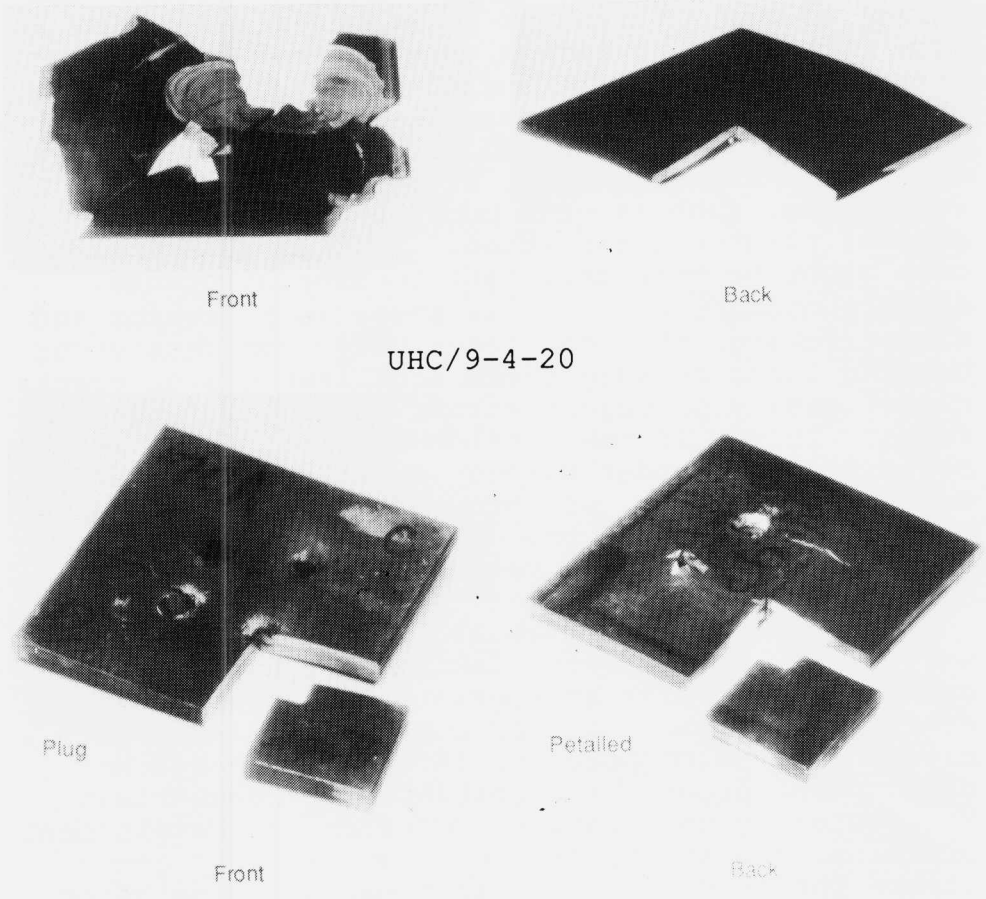

FIGURE 10: Penetration mechanism of UHC/9-4-20 and 4340/9-4-20 laminates.

LAMINATED CASES FOR KINETIC ENERGY PENETRATORS

While the armor development programs were under way, it became apparent the other applications for this metal laminate technology might

exist. Preliminary discussions with the staff of the Air Force Armament Laboratory during 1983 and 1984 suggested that this technology might be applicable to the problem of hardened target penetrator case survivability at higher impact velocities for three reasons. First, if a laminated case could be made much stronger than a conventional monolithic case without sacrificing either internal volume or dynamic fracture toughness, then a laminated case might be more resistant to macrostructural failure mechanisms that can occur at very high impact velocities, such as case buckling, bending, or general plastic deformation. Second, a laminated case might be more resistant to microstructural failure mechanisms, such as shear localization and microcracking, that can occur under compressive or bending loads because shear localizations or cracks cannot easily propagate across the layer interfaces. Third, if the outside surface of a case could be made harder without sacrificing overall fracture toughness, as through lamination, it might be more resistant to the nose erosion that could occur at higher impact velocities.

A serious concern raised at the time, however, was whether or not metal laminates could be fabricated in geometries appropriate for hardened target penetrator cases, that is, a hollow cylinder with a closed end. A cooperative internal research and development program was initiated at Chamberlain Manufacturing Corporation, Research and Development Division, and at SRI International (27) to demonstrate the feasibility of fabricating a laminated case. It was decided to attempt to fabricate full-scale BKEP cases since these are a production item at Chamberlain, using existing tooling and equipment. AISI E4340 steel was selected as one of the components in the laminate, because this material is used to fabricate the conventional BKEP case. The other component selected was AISI 1018 steel because it is a low-carbon, ductile, and readily available material. A two layer, 50/50 volume fraction laminate configuration was chosen because it is the simplest (but not necessarily optimum) geometry.

Using SRI's experience with flat armor plates as a basis, Chamberlain developed the fabrication procedure outlined in Figure 11. The key to success proved to be warm drawing below the transformation temperature of both materials in successive steps, with a wall reduction of about 25% at each step.

Based on this IR&D effort, it appears feasible to fabricate metallic laminate hardened target penetrator cases in a BKEP configuration with desirable properties. Table 1 compares the properties of several candidate penetratory materials, including the conventional 4340 BKEP case material, with the 50/50 metal laminate in the as-oil-quenched condition. The strength and toughness of the laminate are superior to those of the conventional 4340 material. More important, the properties of the laminate are equivalent to the properties of the best available case materials, D6AC and maraging 250, even though the laminate was in no way optimized. For example, if a 70/30 laminate configuration had been fabricated instead of the 50/50 configuration, study data suggest that the strength and ductility of the laminate casing might be comparable to the high performance monolithic materials. If a high performance alloy, such as D6AC had been used as the strong component in the laminate instead of 4340, it is entirely possible that the properties of the laminate would be substantially superior to the monolithic D6AC and maraging 250.

It is believed that a metallic laminate case can be designed with strength, ductility, and impact toughness far superior to any currently available case design. The significance of such an improved case design is that a substantially higher impact velocity could be used with the same explosive charge and the case would survive, and that potentially greater L/D ratios (at constant penetrator weight) can be used with no sacrifice of explosive volume or resistance of the penetrator case to plastic bending or buckling. Development of improved case designs using this technology may also help minimize other problems which reduce penetrator effectiveness and reliability, such as rear section case failure due to the effects of

tail slap, excessive nose erosion, and premature explosive initiation.

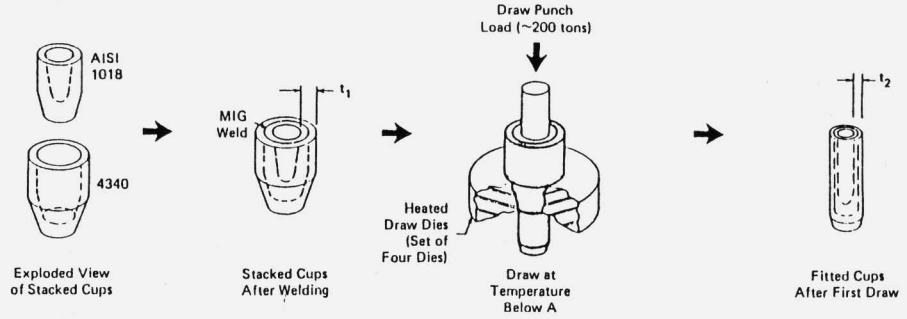

FIGURE 11: Summary of Processing Techniques Used In Forming A Laminated Penetration Case

TABLE 1

PROPERTIES OF CANDIDATE PENETRATOR MATERIALS IN SRI/CHAMBERLAIN IR&D STUDY

	Monolithic 4340	D-6AC[a]	Maraging 250[b]	4340/1018[c] 50/50 Laminate
Yield Strength (ksi)	156	204	230	198
Ultimate Tensile Strength (ksi)	170	210	250	211
Elongation (%)	17	13	11	12
Unnotched Charpy (ft-lb)	195	145	120	>240

[a] 1550°F/OQ/100°F/1 hr/WQ.
[b] Optimum heat treatment.
[c] 1550°F/OQ.

BIMETALLIC LINERS FOR EXPLOSIVELY FORMED PENETRATORS

For an Air Force Study (28), SRI and the staff of the Armament Laboratory at Eglin AFB designed a uniform thickness UHC steel liner with an initial thickness of 6.25 mm (0.25 inches) and an overall diameter of 20.3 cm (8.0 inches).

Because previous experience with UHC steel liners (29) showed that they were highly susceptible to fracturing early in the formation process because of their limited ductility near room temperature, it was decided to use a laminate of fine-grained UHC steel and a softer steel that is more ductile at room temperature. The concept behind this laminate approach was to use the soft steel to help confine and minimize fracture damage to the UHC steel component early in the liner collapse process after the liner had undergone sufficient deformation to adiabatically heat up to several hundred degrees. At this temperature, the UHC steel becomes ductile and is not as susceptible to fracture.

Because the objective of that study was to confine and contain the harder UHC steel, it was decided to sandwich the UHC steel between two layers of A-710 steel. This is a low-alloy, low-carbon, medium-strength high-toughness steel. Previous work (30) with laminated UHC steel/A-710 composites has demonstrated that the composite exhibits substantially improved impact toughness relative to monolithic UHC steel.

A 15.2-cm by 15.2-cm by 0.62-cm-thick plate of fine-grained UHC steel alloy was used in fabricating this laminate. The surface was ground and sandwiched between two A-710 plates of equivalent size and thickness. This 0.75-inch-thick composite was then electron-beam welded along the seams and warm rolled at 700°C into a 0.62-cm-thick plate in multiple passes at about 10% per pass. The net result is a three-layer laminate composite in which the components are metallurgically bonded to each other. (This technique is described in detail in Reference 14.) Three laminated plates, 26 cm by 26

cm by 0.62 cm, were fabricated using this procedure. After the laminated plates were roll bonded, they were annealed and cut into 20.3-cm-diameter blanks for fabrication into liners.

After the liners were formed, they were trimmed and assembled into explosive testing hardware. The results of the tests are summarized in Table 2.

Tests showed that the laminated UHC steel alloy liners fragmented very early in the formation process; jet breakup time is essentially zero. Because of this fragmentation, penetration into the steel target was minimal. Extensive deformation occurred even before fragmentation. Detailed examination indicated that the liners fractured by the initiation and propagation of adiabatic shear bands. Because of the intense deformation, these shear bands apparently initiate on the outer (convex) surface and propagate through the A-710 layer. The study suggests the shear bands were able to readily propagate across the UHCS/A-710 interfaces because of the coherent metallurgical bond between the two components. The shear bands then continued on through the UHC steel layer toward the inner surface of the liner. The intense complex stress state in the liner then caused it to

TABLE 2

SUMMARY OF EXPLOSIVE TESTS FOR UHCS/A-710

Jet Tip Velocity (mm/μs)	Breakup Time (μs[a])	Depth of Penetration (mm)
3.47	0	31.8
3.27	0	Water Tank

[a] Latest time at which a flash X-ray photograph shows the jet to be intact.

fracture along many of these shear bands, and the liner fragmented. Therefore, while the A-710 was able to inhibit brittle fracture of the UHC steel component, it was not sufficiently resistant to adiabatic shear banding to prevent failure by this mechanism.

CONCLUSIONS

The failure of the UHC steel laminate liners has an important implication: both the dynamic fracture and the dynamic deformation characteristics of candidate alloy systems must be determined to fully evaluate their potential. Simply characterizing the dynamic constitutive behavior can be misleading. Models describing the onset and growth of various microfailure mechanisms (such as adiabatic shear banding) must be developed and incorporated along with the constitutive models into codes for predicting the performance of liner materials and configurations. Such failure models and further research are needed to bring advanced materials and concepts into the realm of practical applications.

ACKNOWLEDGEMENTS

Financial support for this work was provided by the Defense Advanced Research Projects Agency, the Army Research Office, the Air Force Armament Laboratory, and the Army Materials Technology Laboratory.

REFERENCES

1. O.D. Sherby, B. Walser, C.M. Young, and E.M. Cady, "Superplastic Ultrahigh Carbon Steels," *Scripta Metall.*, 9, 1975, pp. 569-574.

2. B. Walser, E.S. Kayali, and O.D. Sherby, "Warm Working and Superplasticity in Plain Ultrahigh Carbon Steels," *4th International Conference, Strength of Metals and Alloys*, Nancy, France, August 1976, Vol. 1, pp. 266-270.

3. O.D. Sherby, C.M. Young, B. Walser, and E.M. Cady, Jr., "Superplastic Ultrahigh Carbon Steels," US Patent 3,951,697, April 20, 1976.

4. O.D. Sherby, C.M. Young, B. Walser, E.M. Cady, E.S. Kayali, R.D. Caligiuri, H. Sunada, and J. Wadsworth, "A Summary Report on Superplastic Ultrahigh Carbon Steel," Department of Materials Science and Engineering, Stanford University, Final Report DAHC-15-73-G15, February 1977.

5. O.D. Sherby, J. Wadsworth, R.D. Caligiuri, T. Itoh, J.H. Lin, T. Oyama, B.C. Snyder, M. Tokizane, B. Walser, and R.T. Whalen, "A Summary Report on Ultrahigh Carbon Steels," Department of Materials Science and Engineering, Stanford University, Final Report ONR-N00014-17-C-0149, June 1980.

6. J. Wadsworth and O.D. Sherby, "Influence of Nickel and Vanadium on Superplasticity in Ultrahigh Carbon Steels," *Jour. Mech. Work Technol.*, 2, 1978, pp.53-66.

7. J. Wadsworth and O.D. Sherby, "Influence of Chromium on Superplasticity in Ultrahigh Carbon Steels," *Jour. Mater. Sci.*, 13, 1978, pp. 2645-2649.

8. T. Oyama, J. Wadsworth, M. Korchynsky, and O.D. Sherby, "Influence of Dilute Alloying Additions on the Superplastic Properties of Ultrahigh Carbon Steels," *5th International Conference, Strength of Metals and Alloys*, Aachen, W. Germany, August 1979, Vol. 1, pp. 381-386.

9. B. Walser and O.D. Sherby, "Mechanical Behavior of Superplastic Ultrahigh Carbon Steels at Elevated Temperature," *Met. Trans.*, 10A, 1979, pp. 1461-1471.

10. E. S. Kayali, H. Sunada, T. Oyama, J. Wadsworth, and O.D. Sherby, "The Development of Fine Structure Superplasticity in Cast Ultrahigh Carbon Steels Through Thermal Cycling," *Jour. Mater. Sci.*, 14, 1979, pp. 2688-2692.

11. J. Wadsworth, J.H. Lin, and O.D. Sherby, "Superplasticity in a Tool Steel," *Metals Technol.*, 5, 1981, pp. 190-193.

12. T. Oyama, W. Avery, C. Hua, H-C. Tsai, and O.D. Sherby, "Development of Ultrahigh Carbon (UHC) Steels for Transportation Applications," Department of Materials Science and Engineering, Stanford University, Final Report DTRS-5680-C-00031, July 1980-June 1983.

13. H. Sunada, J. Wadsworth, J. Lin, and O.D. Sherby, "Mechanical Properties and Microstructure of Heat-Treated Ultrahigh Carbon Steels," *Mater. Sci. Eng.*, 38, 1979, pp. 35-40.

14. O.D. Sherby, J. Wadsworth, R.D. Caligiuri, L.E. Eiselstein, B.C. Snyder, and R.T. Whalen, "Superplastic Bonding of Ferrous Laminates," *Scripta Metall.*, 13, 1979, pp. 941-946.

15. B.C. Snyder, "Superplasticity in Ferrous Laminated Composites," PhD Thesis, Department of Materials Science and Engineering, Stanford University, 1982.

16. B.C. Snyder, J. Wadsworth, and O.D. Sherby, "Superplastic Behavior in Ferrous Laminated Composites," *Acta Metall.*, 32, 1984, pp. 919-932.

17. D.W. Kum, "Structure and Mechanical Behavior of Ferrous Laminated Composites Containing Superplastic Ultrahigh Carbon Steels," PhD Thesis, Department of Materials Science and Engineering, Stanford University, 1984.

18. T. Itoh, M. Tokizane, J. Wadsworth, and O.D. Sherby, "Manufacture and Mechanical Properties of Laminated and Monolithic Fine-Grained High Carbon Superplastic Bearing Steel," *Jour. Mech. Work Technol*, 5, 1981, pp. 105-123.

19. D.W. Kum, T. Oyama, J. Wadsworth, and O.D. Sherby, "The Impact Properties of Laminated Composites Containing Ultrahigh Carbon (UHC) Steels," *Jour. Mech. Phys. Solids*, 31, 1983, pp. 173-186.

20. O.D. Sherby, T. Oyama, D.W. Kum, B. Walser, and J. Wadsworth, "Ultrahigh Carbon Steels," *Journal of Metals*, June 1985.

21. T. Oyama, J. Proft, H-C. Tsai, and O.D. Sherby, "Enhancement of Superplasticity in Ultrahigh Carbon (UHC) Steels Through Dilute Alloying Additions," ASM Fall Meeting, Philadelphia, Pennsylvania, October 1983.

22. O.D. Sherby and J. Wadsworth, "Development and Characterization of Fine-Grained Superplastic Materials," *Deformation, Processing, and Structure* (1982 ASM Materials Science Seminar, October 1982, St. Louis, Missouri), edited by G. Krauss, ASM, Metals Park, Ohio, 1984, pp. 355-389.

23. G. Daehn, D.W. Kum, and O.D. Sherby, research in progress, Stanford University, 1985.

24. F.S. Mascianica, "Ballistic Technology of Lightweight Armor," AMMRC Technical Report TR31-20, Army Materials and Mechanics Research Center, Watertown, MA, May 1981, CONFIDENTIAL.

25. L.E. Eiselstein and R.D. Caligiuri, "Application of Laminated Metallic Armors to Heavy Hybrid Armor Systms," *Proceedings, 4th TACOM Armor Coordinating Conference for Light Combat Vehicles*, Monterey, California, March 1988.

26. R.D. Caligiuri, "Evaluation of the Response of Ultrahigh Carbon Steel and Steel Reinforced Composites to Dynamic Loading (U)," SRI International, AD-C034989, March 1982, SECRET.

27. D. Dedic, "Laminated Penetrator Program," Chamberlain IR&D Report 8315-PR-001, Task No. 04-85-022, 1986.

28. R.D. Caligiuri, C.M. Ablow, and C.G. Schmidt, "Influence of Microstructure on the Performance of Explosively Formed Penetrators," SRI Final Report, AF Contract F08635-83-K-0126, March 1986.

29. R.D. Caligiuri, "Production of Ultrahigh Carbon Steel for Evaluation in Explosively Driven Penetrator Applications," Final Report, September 1981 to December 1982, AFAL, Elgin AFB, FL, AFATL-TR-83-47, May 1983.

30. R.D. Caligiuri and L.E. Eiselstein, Unpublished work, 1986.

HETEROGENEOUS PRECIPITATION OF AUSTENITE FOR STABILIZATION

M. GRUJICIC, M. BUONANNO, S.M. ALLEN, G.B. OLSON and M. COHEN
Department of Materials Science and Engineering
Massachusetts Institute of Technology, Cambridge, MA 02139

INTRODUCTION

It is well established, both theoretically and experimentally, that transformation plasticity can give rise to remarkable mechanical behavior in metallic and ceramic materials (1,2). Enhanced ductility and fracture toughness associated with transformation plasticity have been found in both fully austenitic materials as well as in materials with metastable austenite dispersions. A flow-stabilizing influence of transformation plasticity from retained austenite has been shown to be directly related with enhanced uniform ductility in "dual-phase" ferrite/martensite steels (3,4). In a thorough study of martensitic transformation behavior in precipitation-strengthened austenitic TRIP steels, Leâl (5) has clearly shown a transformation-induced enhancement of fracture toughness under conditions of shear-instability-controlled ductile fracture. Haidemenopulos (6) has recently found similiar effects of dispersed austenite in high strength AF1410 steel, where the shear instability also controls fracture toughness. In the case of brittle fracture, the toughening effects of dispersed-phase transformation plasticity have been well demonstrated in ceramic alloys such as partially stabilized zirconia (7,8).

Beneficial effects of transformation plasticity are directly related to thermodynamic stability of the austenitic phase. Leâl (5) has shown that for any given measure of ductility and toughness (uniform strain, fracture strain, and J_{Ic}), there is an optimum austenite stability. This was rationalized in terms of the stress-state dependence of austenite stability due to hydrostatic-stress interaction with the transformation volume change. For an austenitic phase of given composition and particle size (the latter for alloys with dispersed austenite) this optimum stability can in general be obtained at a particular temperature. Often, however, this temperature is very much displaced with respect to ambient temperature, which hampers, practical development of a suitable material. In addition, when the temperature of optimum austenite stability is too high,

various diffusional reactions such as precipitation of deleterious phases, dynamic strain aging, etc., may come into play, impairing beneficial effects associated with the transformation. One would thus like to be able to control austenite stability in such a way that its optimum stability for a given stress-state can be placed at the desired temperature.

In this paper we consider the problem of obtaining austenite of controlled stability in a class of microalloyed ferrite/martensite/austenite "triple-phase" steels with relatively high contents of austenite. These steels are based on the Fe-Mn-C system with microadditions of Si, Cr, Mo, etc. Used for high stretch-formability applications, these steels would require austenite stability optimized to the near-plane-strain stress states of interest in sheet-forming processes. In this paper, however, we primarily deal with an issue of maximizing austenite stability while limiting the total alloy content to the "micro-alloying" regime.

In the first section, we present a thermodynamic analysis for austenite formation from a soft-annealed ferrite/cementite microstructure during inter- and supercritical annealing treatment of a model Fe-1.8 w/oMn-0.1w/oC alloy. The emphasis is placed on tailoring the starting micostructure and annealing conditions in order to achieve austentite of maximum stability.

In the second section we present results of our experimental study on the intercritical annealing behavior of two heats of microalloyed steels.

THERMODYNAMICS OF AUSTENITE FORMATION IN Fe-Mn-C SYSTEM

Despite the fact that both Mn and C are very effective austenite-stabilizing elements, equilibrium austenite in low-carbon (<0.2 wt%), low Mn (<2.0 wt%) steels is not very stable. Using the model recently proposed by Hsu (9), M_S temperature were calculated for a low-carbon/low-manganese composition range of austenite, Fig. 1. It is seen that in order for the M_S temperature to be around room temperature, carbon and manganese contents of austenite have to be far in excess of the desired composition range. Figure 2 shows the M_S temperatures of equilibrium austenites throughout the

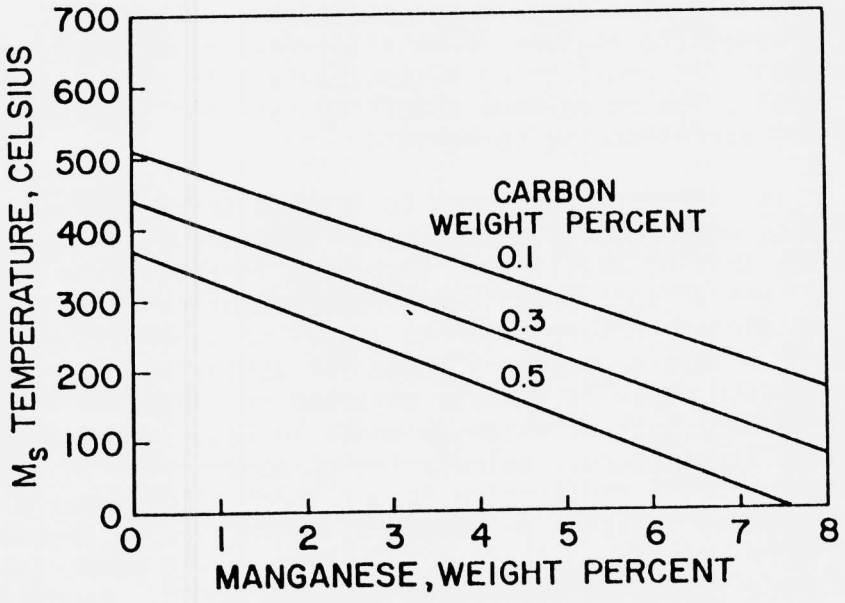

Fig. 1 Effect of carbon and manganese on the M_S temperature in Fe-Mn-C alloys

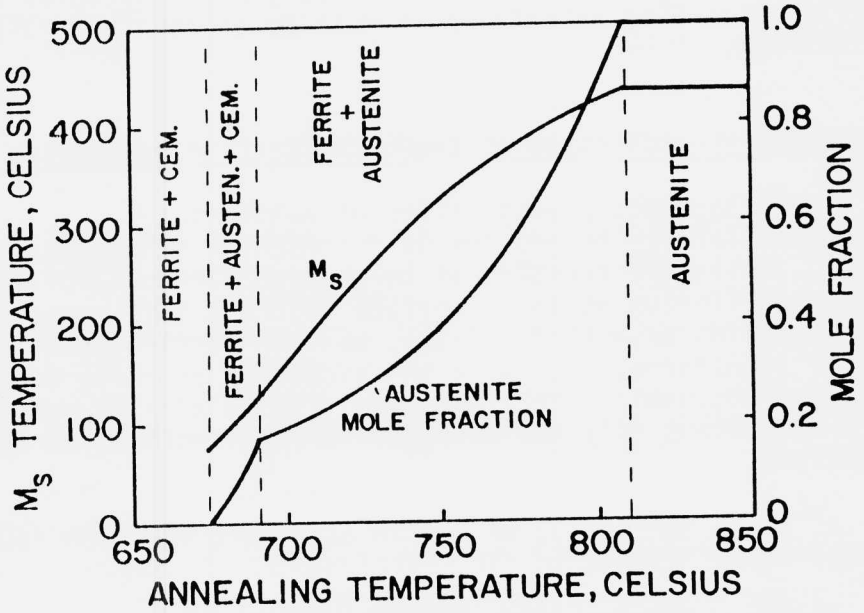

Fig. 2 M_S temperature and mole fraction of equilibrium austenites in a Fe-1.8 wt% Mn-0.1 wt% C alloys

two-phase austenite/ferrite and three-phase austenite/ferrite/cementite regions in an alloy Fe-1.8 wt%-Mn-0.1wt%C. It is seen that equilibrium austenite in this alloy is not very stable, having maximum stability (at near zero volume fraction) corresponding to M_S=74°C.

It is therefore necessary to develop thermomechanical treatments which can give rise to an austenite, having higher stability than of equilibrium austenite in this class of steels. Use of soft-annealed ferrite/cementite steel as a starting microstructure prior to inter- or supercritical annealing offers a promising route for achieving this goal. The cementite phase is greatly enriched in manganese and of course carbon, both of which as shown in Fig. 1 are strong austenite stabilizers. Calculation of composition in the ferrite/cementite equilibrium in our model alloy shows a high manganese fraction on the metal sublattice in cementite, which increases from 0.21 to 0.27 on decreasing tempering temperature in the range between 650 and 500°C. Should this high manganese content be inherited by austenite during inter- or supercritical treatment, it would ensure a high stability of austenite. In the following we present a thermodynamic analysis of austenite formation from a soft annealed ferrite/cementite microstructure. We analyze the austenite formation via heterogeneous precipitation at both ferrite/cementite interfaces as well as at ferrite grain boundaries.

Austenite Precipitation at Cementite/Ferrite Boundaries

Heterogeneous precipitation of austenite at cementite/ferrite boundaries is represented schematically in Fig. 3. While the question as to whether paraequilibrium or local equilibrium at the interface controls this reaction still remains unsettled (10-12), we have studied both regimes of transformation. With the exception of a few details, both thermodynamic conditions give rise to similar results. Here we present only the paraequilibrium treatment of this reaction.

As shown in Fig. 3, we can in principle envision four phases participating in the reaction:

PCEM - cementite having the amount of alloying elements fixed by the tempering temperature (temperature of soft annealing);

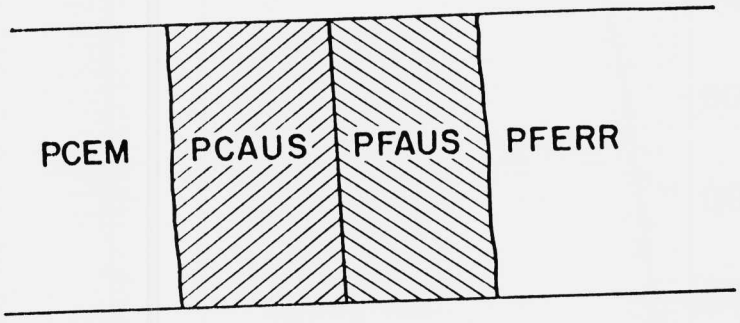

Fig. 3 Schematic representation of formation of paraequilibrium austenites at a ferrite/cementite boundary. See the text for explanation of phase names.

PCAUS - austenite having the alloy content of PCEM, with which it is in equilibrium relative to carbon (paraequilibrium);

PFERR - ferrite having the alloy content fixed by the tempering temperature, and

PFAUS - austenite having the alloy content of PFERR with which it is in paraequilibrium.

Figures 4 and 5 show the paraequilibrium phase diagrams for the PCEM/PCAUS and PFERR/PFAUS systems respectively. The initial in carbon content PFERR at 650°C, $^{\circ}x_C^{PFERR}$ is indicated in Fig. 5. Also the carbon content, x_C^{PFERR}, in PFERR adjusted for the PFERR/PCEM equilibrium at each temperature of inter- or supercritical annealing is also shown in this figure (the paraequilibrium PFERR/PCEM phase diagram is not shown here).

The tendency for precipitation of the two austenite phases, PCAUS and PFAUS, is shown in Fig. 6 where the driving forces for precipitation are plotted versus temperature.

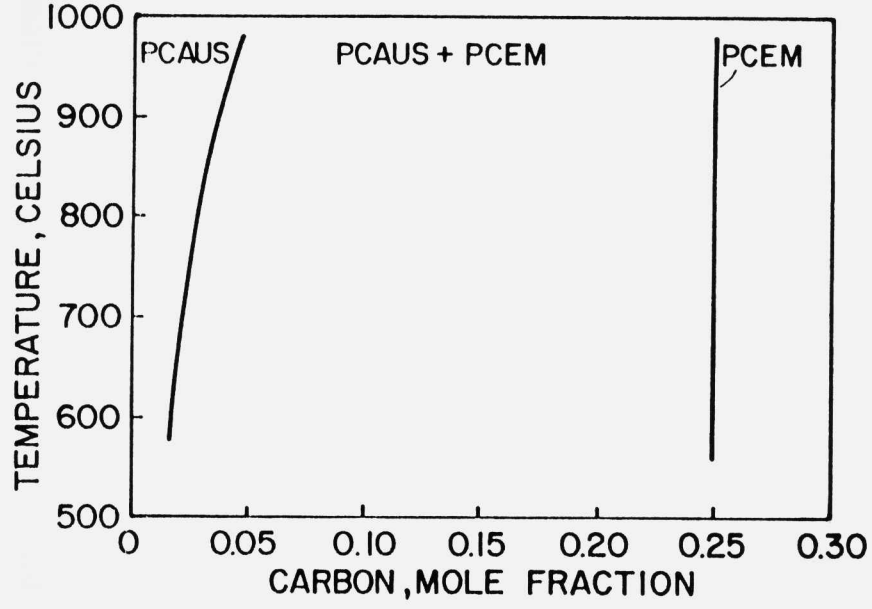

Fig. 4 Paraequilibrium phase diagram for austenite and cementite having 25% of Mn occupying the metal sublattice

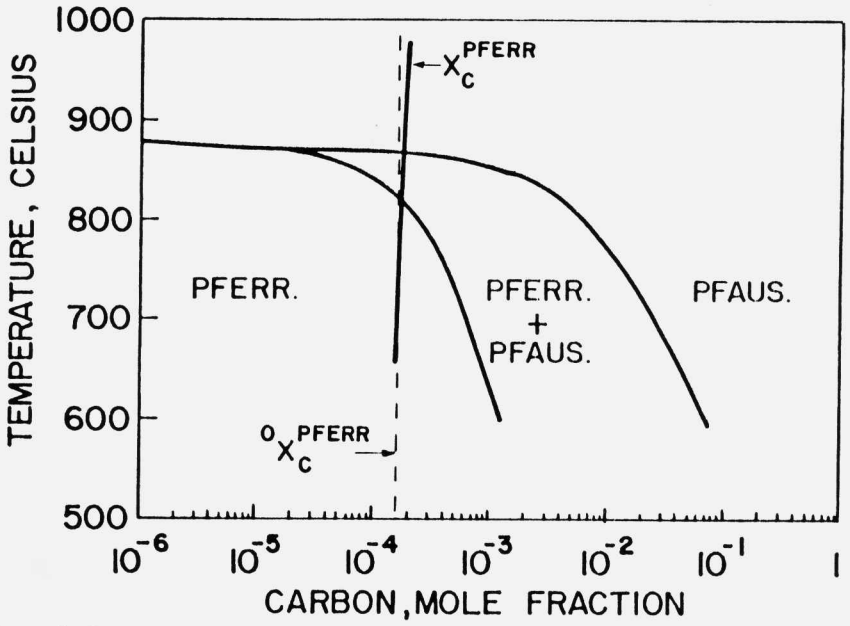

Fig. 5 Paraequilibrium phase diagram for ferrite and austenite having 1.6% of Mn occupying metal sublattice

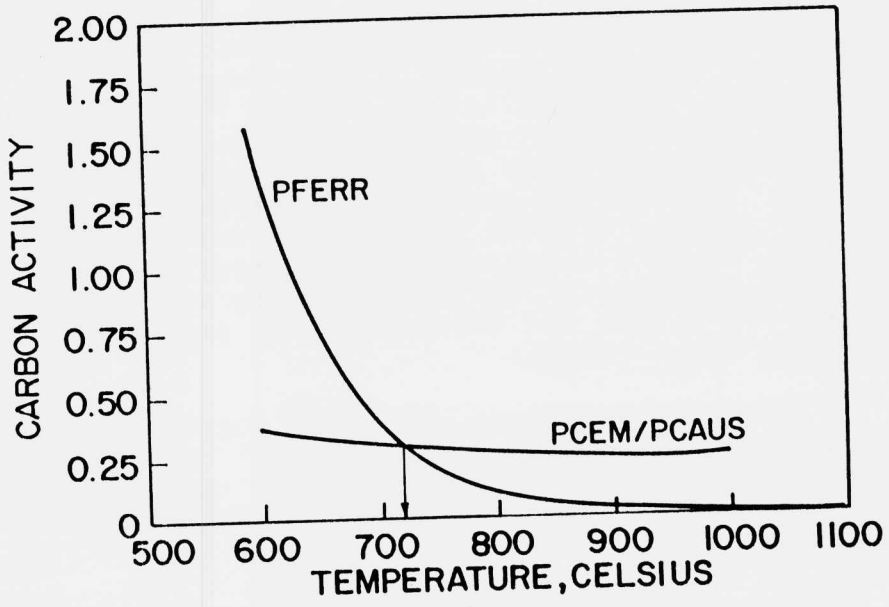

Fig. 6 Effect of temperature on the carbon activity in ferrite (PFERR) and on that set of cementite-austenite (PCEM/PCAUS) paraequilibrium

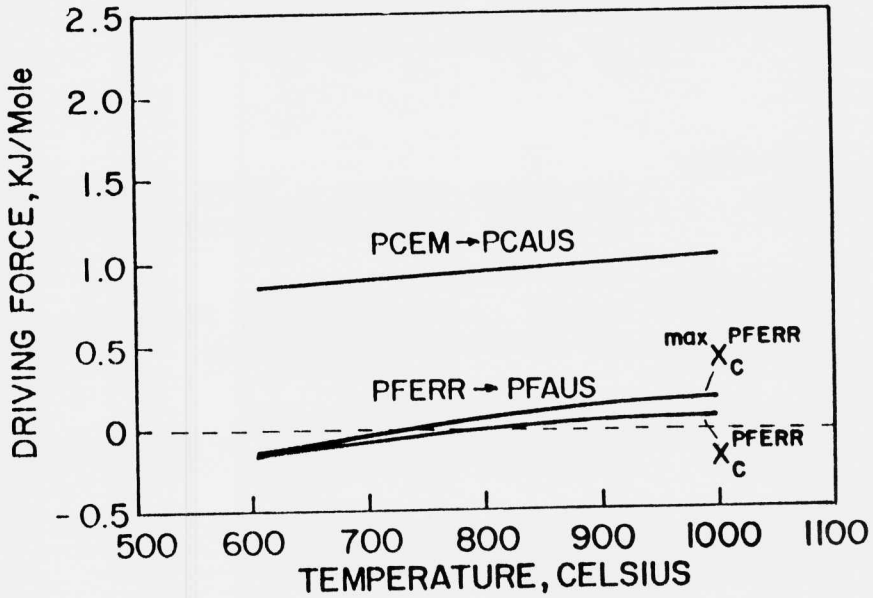

Fig. 7 Effect of temperature on the driving force for nucleation of austenite in cementite (PCEM→PFAUS). See the text for explanation of X_C^{PFERR} and $\max X_C^{PFERR}$.

Figure 7 shows the free energy change accompanying formation of two austenite phases. Comparison of the driving forces and free energy changes for the two reactions suggests that PCAUS is more likely to nucleate at each temperature and, once nucleated, would tend to grow into the PCEM phase converting it into austenite, while maintaining paraequilibrium at the PCEM/PCAUS interface and conveying excess carbon into the PFERR. This reaction will thus proceed when and until the carbon activity in PFERR is lower than that in PCEM and PCAUS. Figure 8 illustrates the variation of carbon activity in PFERR and at PCEM/PCAUS boundary with temperature. It is seen that the reaction can proceed only at temperature above - 720°C.

As the reaction proceeds, the cabron content in the PFERR phase increases until it becomes equal to that set by PCEM/PCAUS equilibrium. At this point, the reaction ceases and further growth of austenite relies on the partitioning of alloying elements.

Using a simple relation for mass balance in carbon, one can estimate the extent of PCEM→PCAUS conversion, e, at each temperature:

$$e = \frac{({}^{max}X_C^{PFERR} - X_C^{PFERR})\,(1 - f^{PCEM})}{(0.25 - X_C^{PCAUS})\,f^{PCEM}}$$

where ${}^{max}X_C^{PFERR}$ = the carbon content in PFERR corresponding to a halt in PCEM→PCAUS conversion,

X_C^{PFERR} = initial carbon content in PFERR adjusted for PCEM/PFERR equilibrium,

X_C^{PCAUS} = carbon content in PCAUS in equilibrium with PCEM, and

f^{PCEM} = mole fraction of PCEM.

Figure 9 shows the extent of PCEM→PCAUS conversion as a function of temperature. It is seen that temperatures as high as 970°C have to be applied in order to complete the reaction.

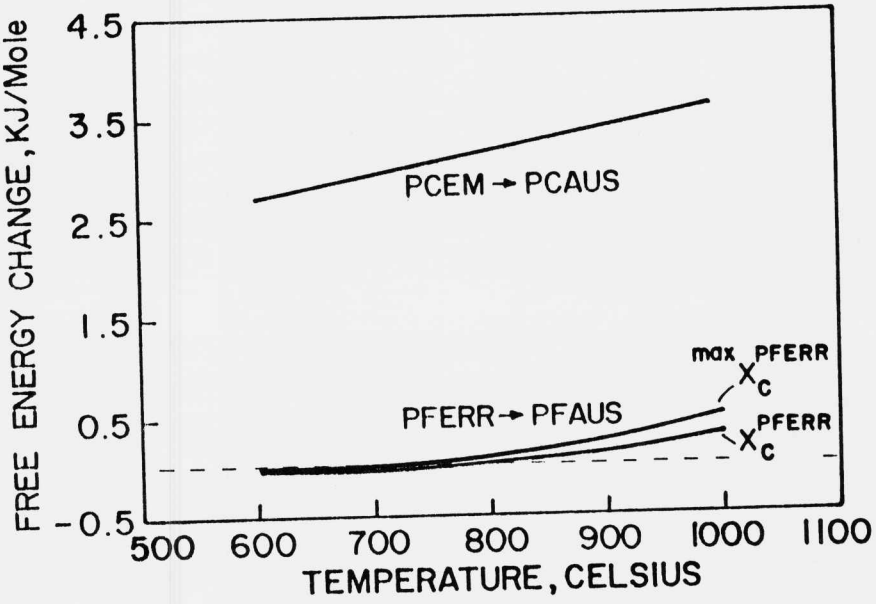

Fig. 8 Effect of temperature on the free energy change attending nucleation of austenite in cementite (PCEM→PCAUS) and in ferrite (PFERR→PFAUS). See the text for explanation of X_c^{PFERR} and $\max X_c^{PFERR}$.

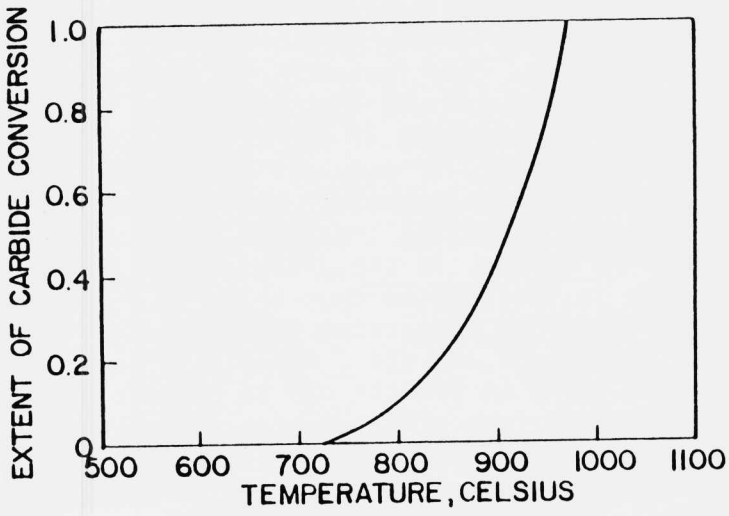

Fig. 9 Extent of cementite/austenite conversions a function of temperature of inter- or supercritical annealing

As the PCEM→PCAUS conversion proceeds, the carbon content in PFERR increases and so does the tendency for precipitation of PFAUS. This is indicated in Fig. 6, where the variation of driving force for precipitation of PFAUS from PFERR is plotted with PFERR enriched in carbon to the extent of $^{max}X_C^{PFERR}$ corresponding to a halt of the PCEM→PCAUS conversion. As expected, the driving force has increased compared to that of the X_C^{PFERR} and becomes more comparable to that for PCEM→PCAUS conversion. The latter is particularly the case at higher temperatures and this point is worth further analysis.

In order to achieve greater extents of PCEM→PCAUS conversion, one has to go to a high temperature (supercritical) annealing treatment. At these temperatures, the likelihood for formation of less stable PFAUS increases. In fact temperatures corresponding to a full completion of PCEM→PCAUS reaction, correspond to supercritical temperatures for PFERR. PFERR then can transform into PFAUS via a massive transformation without requiring any diffusion of carbon. In order to avoid massive formation of less stable PFAUS austenite, it is necessary to lower temperature of complete cementite conversion. Inspection of equation (1) shows that e is most sensitive to variation of $(^{max}X_C^{PFER} - X_C^{PFERR})$ term. Maximizing this term ensures higher extent of cementite conversion at each temperature and thus lower temperature at which this conversion is complete. Elements which lower the Henrian activity coefficient of carbon in ferrite increase the $(^{max}X_C^{PFERR} - X_C^{PFERR})$ term, giving rise to a larger e. For instance, an increase in Mn content of the ferrite from 1.6 wt% (Mn content in ferrite in equilibrium with cementite at 650°C in our alloy) to 1.7 wt% lowers the temperature of complete PCEM→PCAUS conversion by about 25 degrees. An incomplete Mn partitioning to cementite during soft annealing treatment along with an overall increase of Mn content in the alloy, which yields a high amount of Mn in the ferrite thus helps to lower the temperature of complete conversion of cementite. Additional elements like Cr, Mo, W, etc., which also lower the Henrian activity of carbon in ferrite can be beneficial. Besides their tendency to form other carbide phases, these elements are effective cementite stabilizers and thus have a strong tendency to partition out of the ferrite phase. The ensuing stabilization of cementite then makes its conversion into austenite more difficult and requires higher temperatures. Should these elements be added to an alloy, the soft annealing treatment should be conducted in such a way that

their partitioning into cementite is minimized. Slower diffusers like W and Mo are then preferred to Cr.

Heterogeneous Austenite Precipitation on Grain Boundaries

Heterogeoeous precipitation of austenite at ferrite grain boundaries is a commonly observed mode of austenite formation in the class of steel under consideration (see next section). An easy accommodation of shape misfit and surface-energy anisotropy of the nucleating particle makes grain-boundary nucleation energetically favorable. Yet, the driving force for austenite nucleation has to be positive and, as indicated in Fig. 6, this is the case for nucleation of PFAUS only at relatively high temperatures of ~800°C. It is then surprising that grain boundary nucleation of austenite is commonly observed at much lower temperatures. A possible explanation of this behavior can be linked to a tendency of Mn and C to cosegregate to grain boundaries, making the latter preferred places for austenite nucleation beyond the thermodynamic prediction shown in Fig. 6. In a steel of similar chemistry as our model alloy, Cai et al. (13) have found a grain-boundary segregation coefficient for manganese as high as 1.25. A corresponding carbon-segregation coefficient of 1.1 has been calculated under the assumption of equal carbon activity in bulk and at grain boundaries. For this extent of grain-boundary segregation, the temperature at which nucleation of the PFAUS phase becomes thermodynamically feasible is lowered by as much as 40 degrees. Mn/C cosegregation can thus be responsible for the frequent observation of austenite grain-boundary nucleation and should therefore be minimized. Alloy additions like Mo, which tend to compete with Mn for available sites at grain boundaries and is not an austenite stabilizer, can be beneficial in this respect.

EXPERIMENTAL STUDY OF HETEROGENEOUS AUSTENITE PRECIPITATION AT 740°C

Preliminary study of heterogeneous austenite precipitation during intercritical annealing at 740°C has been conducted on the two steels whose compositions are given in Table 1. In this section we present a brief summary of the key results.

TABLE 1

COMPOSITION OF ALLOYS USED IN THE PRESENT STUDY

	C	Mn	Si	V	Cr	Ni	Mo	Ti	Al
Alloy A	0.1	1.86	0.25	-	-	-	-	-	0.024
Alloy B	0.1	1.45	0.52	0.059	1.0	0.53	0.49	0.02	0.042

TABLE 2

HEAT TREATMENT OF ALLOY B

CRT Series	Austenitize at 954°C for 1 hr Brine Quench Cold-roll (70%) Temper, Air cool
T Series	Cold Roll (70%) Austenitize at 954°C for 1 hr Brine Quench Temper, air cool

Alloy A

After quenching from 900°C, alloy A was tempered at 550, 600 and 650°C for times of 6, 60 and 600 min. Figure 10 shows the extent of manganese enrichment and Figure 11 the average diameter of cementite particles as functions of temperature and time of tempering.

Specimens with the highest extent of Mn enrichment (650°C/600 min.) were intercritically annealed for periods of 100, 1000 and 10,000 seconds at 740°C.

Upon heating for 100 seconds the recrystallization of ferrite takes place along with formation of austenite. Austenite (martensite upon quenching) mainly decorates the boundaries of newly formed ferrite grains.

At longer times of 1,000 and 10,000 seconds ferrite recrystallization appears to have reached its completion. Coarsening and dissolution at cementite particles take place along with the growth of austenite (martensite) which by this time forms a needle-like network.

Heterogeneous austenite nucleation at cementite particles was quite scarce. Figure 12a shows a bright image of a single austenite particle (completely black) which appears to have formed by in situ conversion of a cementite particle in the vicinity of another cementite (smaller) particle. Use of [042] fcc reflection for dark-field imaging, Figure 12b lit up larger particle, confirming its austenitic structure, Figure 12c. As predicted by thermodynamic analysis in the previous section for a temperature of 740°C, the extent of cementite conversion is very small (Fig 9), which explains the rarity of heterogeneous austenite precipitation at cementite particles.

Ferrite recrystallization, which was found to promote austenite formation on grain boundaries, is a serious problem leading to a structure with less stable austenite that transforms to martensite during cooling. It is thus essential to have starting microstructure with fully recrystallized ferrite.

Alloy B

Two different thermomechanical treatments, T and CRT, were employed in the case of alloy B prior to tempering at 650°C, Table 2.

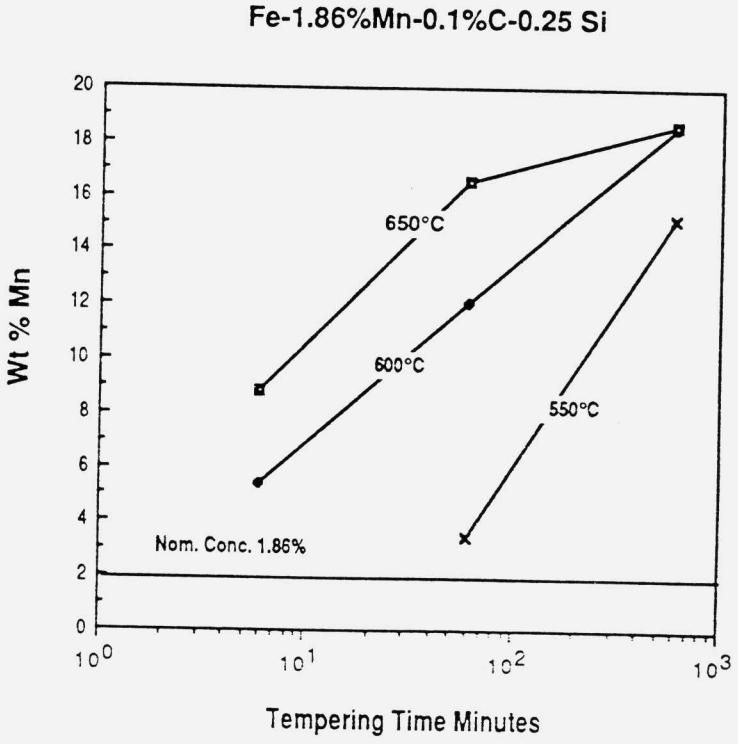

Fig. 10 Effect of temperature and time of tempering on the Mn content of cementite particles in alloy A

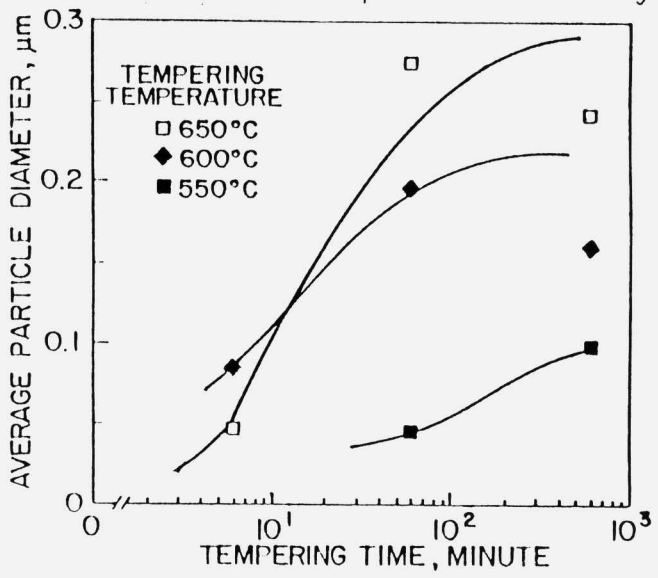

Fig. 11 Effect of temperature and time of tempering on the average size of cementite particles in alloy A

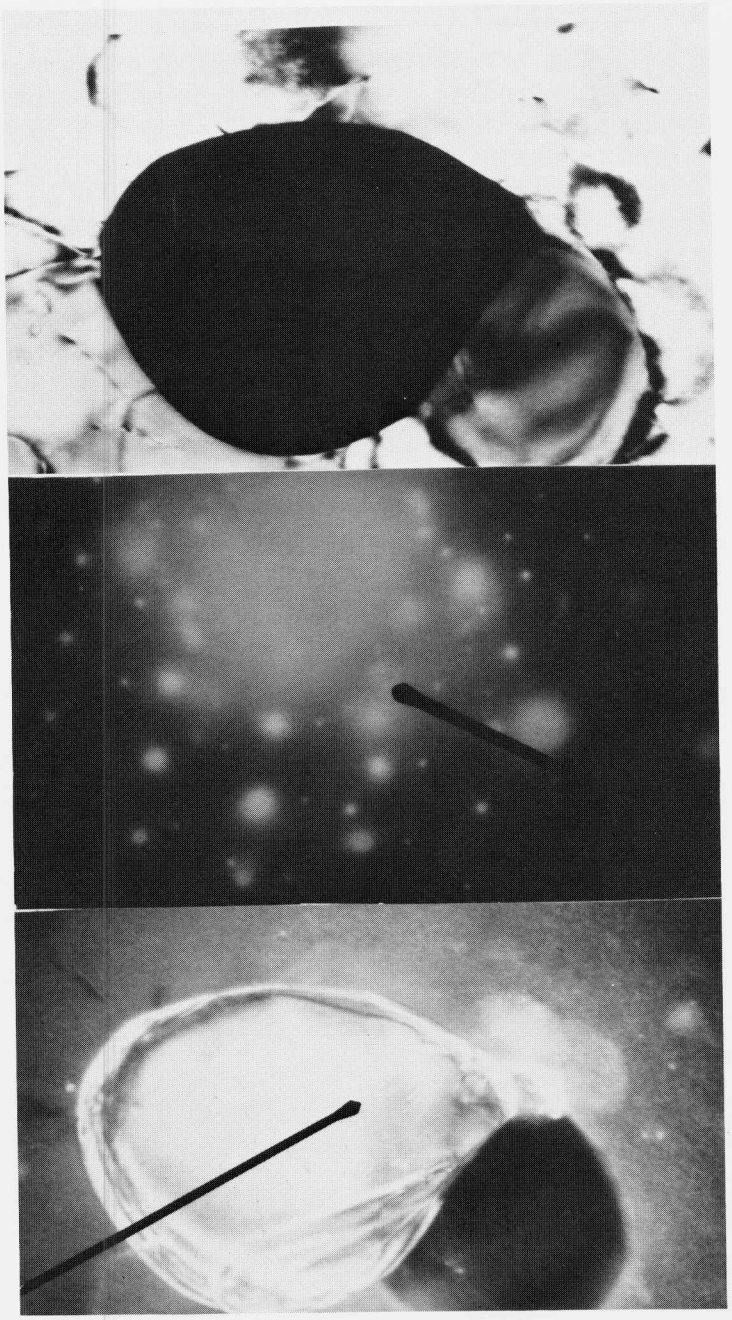

a)

b)

c)

Fig. 12 STEM micrograph of alloy A intercriticaly treated at 740°C for 1200 seconds. a) the bright field image shows an austenite particle (black) in the vicinity of a smaller cementite particle, b) the corresponding diffraction pattern. The pattern which has been indexed belongs to a FCC structure,c) The dark field image obtained using the [042] FCC spot as indicated in (b).

EDXA analysis of carbide particles after tempering at for 1 hr is summarized in Table 3. It is worth noticing that somewhat higher levels of Cr (~22 wt%) are found in cementite particles in the CRT series compared to (~17%)Cr in the T series. The Mn level does not seem to be very different in two series, ~10wt%. Upon intercritical annealing for 10 seconds, the CRT series shows no sign of heterogeneous austenite precipitation on cementite particles. A typical austenite (martensite) structure, resulting from heterogeneous nucleation on grain boundaries, is shown in Figure 13. The T series on the other hand, showed some evidence of cementite conversion to austenite. Figure 14 shows austenite particles, labelled 1,2, and 3 in the vicinity of an untransformed cementite particle labelled 4. Heterogeneous precipitation of austenite (martensite) at grain boundaries was still a more common observation.

Fig. 13 STEM micrograph (bright field image) of Alloy B (CRT series) after intercritical treatment at 740°C for 100 seconds. A pool of austenite has transformed to martensite at the grain broundary.

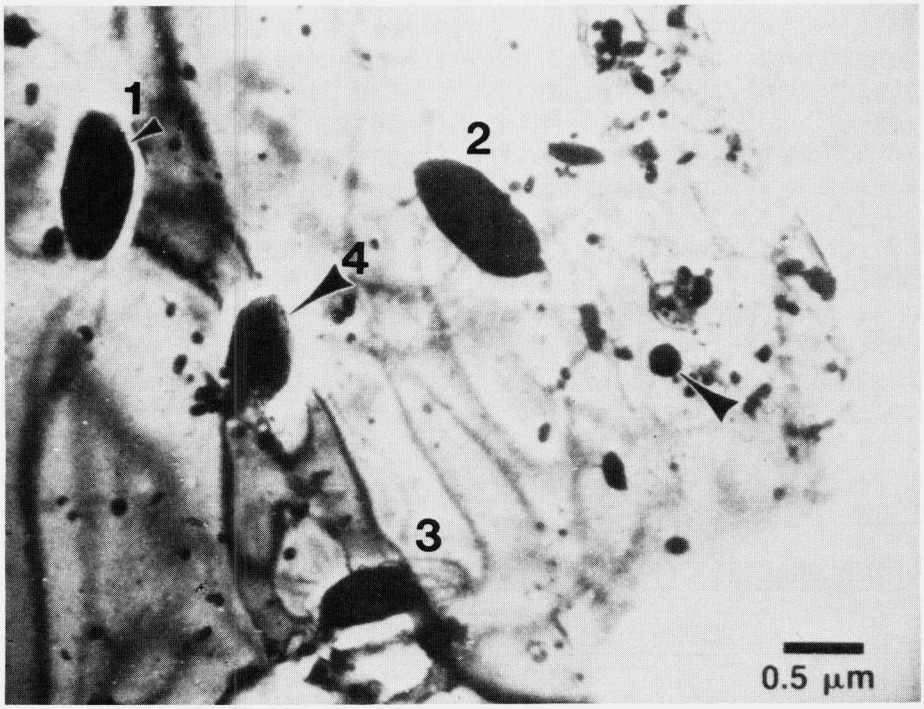

Fig. 14 STEM micrograph (bright field image of Alloy B (T Series) after intercritical treatment at 740°C for 1000 sec. Particles 1,2 and 3 are austenite particles. Particle 4 is a cementite particle

The observed difference in behavior of steel B in the two heat treated conditions with respect to formation of austenite at cementite particles can be related to a difference in Cr content of the cementite particles. A lower chromium content of cementite, which is tantamount to a higher chromium content in ferrite, ensures a lower carbon activity which, according to the previous analysis, then leads to greater cementite conversion. It should be noted that, in both series, the extent of chromium partitioning is too high thereby giving rise to higher cementite stability and requiring higher temperatures for cementite conversion.

CONCLUSIONS

Among various modes of austenite formation, the in-situ cementite/austenite conversion is thermodynamically most likely to take place during an inter- or supercritical treatment of a tempered ferrite/Mn-enriched cementite microstructure in low Mn, low-C steels; ensuing autenite is very stable due to its higher Mn content. Increased amount of this austenite, through a complete cementite/austenite conversion can be achieved only at high (supercritical) temperatures. At these temperatures, the likelihood for formation of undesirable, less stable austenite at grain boundaries or via massive transformation of ferrite increases. In this regard addition of elements which lower the Henrian activity of carbon in ferrite such as Mn, Cr, Mo, W etc. is beneficial. Another important parameter controlling the extent of grain-boundary formation of austenite is the degree of recrystallation of the the ferrrite matrix. As shown experimentally, an incompletely recrystallized ferrite matrix promotes extensive formation of grain-boundary austenite.

TABLE 3

EXDA ANALYSIS OF CEMENTITE PARTICLES IN ALLOY B AFTER TEMPERING AT 650°C FOR 1 HOUR

	Mn	Cr	Mo	V	Ti
T-Series	10.08	9.91	3.13	1.26	-
	10.20	14.00	2.83	1.00	-
	10.86	15.73	1.94	0.37	-
	13.73	19.20	2.99	0.72	0.17
	15.94	23.76	3.70	1.28	0.06
CRT-Series	9.32	14.10	1.06	0.54	-
	14.56	29.94	3.49	1.34	-
	15.26	22.61	1.41	1.10	-

ACKNOWLEDGEMENT

This work has been supported by the National Science Foundation under Grant #DMR-8418718.

REFERENCES

(1) G.B. Olson,"Transformation Plasticity and the Stability of Plastic Flow," in Deformation Processing and Structure, ASM, Metals Park, OH 1983, p. 391.

(2) G.B. Olson and M. Cohen, "Martensitic Transformation as a Deformation Process," in Mechanical Properties and Phase Transformations in Engineering Materials, ed. S.C. Antolovich, R.O. Ritchie and W.W. Gerberich, The Metallurgical Society of AIME, 1986, p. 367.

(3) T. Narutani, G.B. Olson and M. Cohen, unpublished research, MIT, Cambridge, MA 1982.

(4) A.K. Sachdev, Acta Metall., 31 (1983) 2037-2042.

(5) R.H. Leal, "Transformation Toughening of Metastable Austenitic Steels," Sc.D. Thesis, MIT, June 1984.

(6) G. Haidemenopoulos, "Transformation Plasticity of Dipersed Austenite in High-Strength Martensitic Steels," Doctoral Thesis in Progress, MIT, Sept. 1987.

(7) R.C. Gavrie, R.H. Hannick and R.T. Pascoe, Nature, 253 (1975) 703.

(8) A.G. Evans and A.H. Heuer, J. Amer. Cev. Soc., 63 (1980) 241.

(9) H. Chang and T.Y. Hsu (Xu Zuyao), Acta Metall. 34 (1986) 333.

(10) M. Hillert, K. Ni Lsson and L.-E Torndahl, J. Iron Steel Inst., 209 (1971) 49.

(11) P.A. Wycliffe, G.R.Purdy and J.D. Embury, Can. Metall. Quart., 20 (1981), 339.

(12) S. Estay, L. Chengji, and G.R. Purdy, ibid, 23 (1984) 121.

(13) X.L. Cai, A.J. Garratt-Reed and W.S. Owen, Metall, Trans A, 16A (1985) 543.

Fig. 1 Effect of carbon and manganese on the M_S temperature in Fe-Mn-C alloys

Fig. 2 M_S temperature and mole fraction of equilibrium austenites in a Fe-1.8wt% Mn-0.1 wt% C alloys

Fgi. 3 Schematic representation of formation of para-equilibrium austenites at a ferrite/cementite boundary. See the text for explanation of phase names.

Fig. 4 Paraequilibrium phase diagram, for austenite and cementite having 25% of Mn occupying the metal sublattice

Fig. 5 Paraequilibrium phase diagram for ferrite and austenite having 1.6% of Mn occupying metal sublattice

Fig. 6 Effect of temperature on the carbon activity in ferrite (PFERR) and on that set of cementite-austenite (PCEM/PCAUS) paraequilibrium

Fig. 7 Effect of temperature on the driving force for nucleation of austenite in cementite (PCEM→PFAUS). See the text for explanation of X_C^{PFERR} and $max X_C^{PFERR}$.

Fig. 8 Effect of temperature on the free energy change attending nucleation of austenite in cementite PCEM→PCAUS) and in ferrite (PFERR→PFAUS). See the text for explanation of X_C^{PFERR} and $max X_C^{PFERR}$.

Fig. 9 Extent of cementite/austenite conversions a function of temperature of inter- or supercritical annealing

Fig. 10 Effect of temperature and time of tempering on the Mn content of cementite particles in alloy A

Fig. 11 Effect of temperature and time of tempering on the average size of cementite particles in alloy A

Fig. 12 STEM micrograph of alloy A intercriticaly treated at 740°C for 1200 seconds. a) the bright field image shows an austenite particle (black) in the vicinity of a smaller cementite particle, b) the corresponding diffraction pattern. The pattern which has been indexed belongs to a FCC structure, c) The dark field image obtained using the $[0\bar{4}2]$ FCC spot as indicated in (b).

Fig. 13 STEM micrograph (bright field image) of Alloy B (CRT series) after intercritical treatment at 740°C for 100 seconds. A pool of austenite has transformed to martensite at the grain boundary.

Fig. 14 STEM micrograph (bright field image of Alloy B (T Series) after intercritical treatment at 740°C for 1000 sec. Particles 1,2, and 3 are austenite particles. Particle 4 is a cementite particle.

DISPERSED-PHASE TRANSFORMATION TOUGHENING IN ULTRAHIGH STRENGTH STEELS

GREGORY HAIDEMENOPOULOS, GREGORY B. OLSON and MORRIS COHEN,
Department of Materials Science and Engineering,
Massachusetts Institute of Technology, Cambridge, MA 02139

ABSTRACT

Previous work on TRIP steels has shown dramatic increases in toughness associated with the transformation of homogeneous metastable austenite. These concepts are now applied in Ultrahigh-Strength steels where the austenite is present as a dispersed phase either retained from the initial quench or precipitated during tempering or intercritical annealing.

The transformation plasticity effects associated with dispersed, retained austenite in 4340 steel have been investigated experimentally. The stability of retained austenite was characterized quantitatively as a function of stress state. Controlled experiments, using high-magnetic-field cryogenic treatments to vary the amount of retained austenite, demonstrated a flow-stabilizing effect in pure shear deformation.

On the other hand, precipitated austenite is more promising for dispersed-phase transformation toughening, since the stability of austenite can be controlled with compositional variations and processing. Size refinement and chemical enrichment of the austenite particles with γ-stabilizing solute elements are the two most potential mechanisms promoting austenite stabilization. These phenomena are studied experimentally in the high Ni-Co secondary hardening martensitic steels, and preliminary results indicating substantial toughness improvements are presented here.

INTRODUCTION

The interaction of deformation-induced transformation of a dispersed, metastable phase with fracture-controlling processes such as microvoid-induced shear localization, can lead to substantial improvements in fracture toughness. This

toughening mechanism is then termed Dispersed-Phase Transformation toughening. It should be differentiated from the transformation toughening found in TRIP steels where the transforming phase is homogeneous austenite. In the ultrahigh-strength steels under consideration in this paper, the transforming phase is dispersed metastable austenite either in the form of retained austenite or precipitated austenite. The conventional retained austenite is the austenite that remains untransformed after quenching from the solution temperature. On the other hand, the "precipitated" austenite forms upon tempering or intercritical annealing. An important difference between these two forms of dispersed austenite is the stability against martensitic transformation. Substantial transformation toughening can be achieved only when the austenite has an optimum stability which is quite high. This high stability can be achieved by size refinement and compositional enrichment of the precipitated austenite, parameters which can be controlled using multistep heat treatments. This controlled metastability is not possible with conventional retained austenite. However, study of transformation plasticity effects associated with retained austenite give insight into its effects on mechanical behavior and help clarify the still controversial role of retained austenite on fracture toughness. For this reason the VAR 4340 steel was chosen to study the effects of retained austenite, while precipitated austenite is examined in high Ni-Co secondary hardening steels.

The next section provides a background discussion of transformation plasticity, transformation toughening, and austenite stabilization. Retained and precipitated austenite are then treated separately.

BACKGROUND

Dispersed-Phase Transformation Plasticity

Deformation can stimulate the kinetics of solid-state phase transformations through both the thermodynamic effect of applied stress and the production of new catalyzing defects by plastic strain. For the case of martensitic transformations, these interactions are depicted in the stress-temperature diagram of Fig. 1. Spontaneous transformation triggered by pre-existing nucleation sites occurs on cooling to the M_S^{σ} temperature. Stress-assisted nucleation on the same sites will occur at the stress denoted by the solid line indicated. At a temperature designated M_S^{σ}, this

stress reaches the yield stress σ_y for slip in the parent phase. Above M_s^σ, new potent nucleation sites introduced by plastic strain trigger strain-induced nucleation. The temperature M_s^σ thus defines an approximate boundary between the temperature regimes where the two modes of nucleation dominate; near the M_s^σ both modes operate. Due to transformation plasticity, the observed yield stress follows the stress for stress-assisted transformation below the M_s^σ. A reversal of the temperature dependence of the flow stress thus provides a convenient determination of the M_s^σ temperature. The M_s^σ temperature characterizes the stability of the parent phase against deformation-induced transformation. M_d is the maximum temperature above which martensitic transformation cannot be induced by deformation. Both the M_s^σ and M_d temperatures are strong functions of stress state due to the transformational volume change.

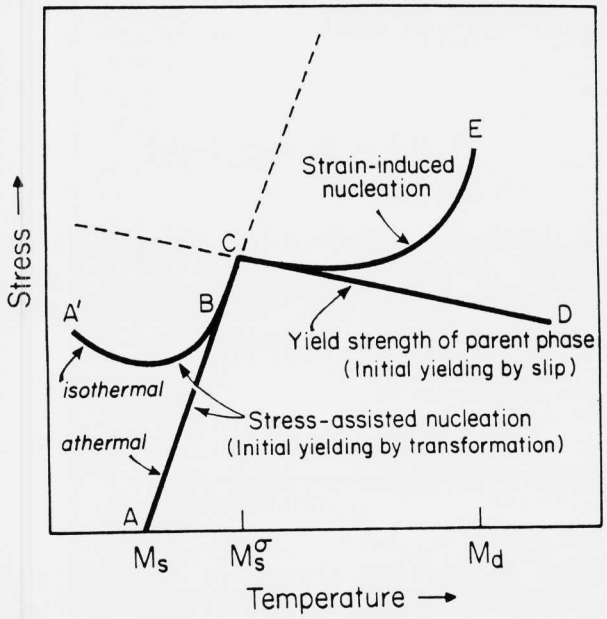

Fig. 1 Schematic representation of interrelationship between stress-assisted and strain-induced martensitic transformation.

For the case of stress-assisted nucleation, the applied elastic stress assists the transformation kinetics by modifying the effective potency distribution of the pre-existing nucleation sites. Based on a dislocation-dissociation model of classical heterogeneous martensitic nucleation

via elastic interactions with internal stress concentrations [1], the potency of a nucleation site can be expressed in terms of the thickness n (in number of crystal planes) of the nucleus that can be derived from the defect by barrierless dissociation. The critical n for nucleation at a given thermodynamic driving force per unit volume Δg^{ch} is:

$$n = - \frac{2\gamma_s/d}{\Delta g^{ch} + E^{Str} + w_f} \qquad (1)$$

where γ_s is the nucleus specific interfacial energy, d is the crystal interplanar spacing, E^{Str} is the elastic strain energy per unit volume associated with distortions in the nucleus interface plane, and w_f is the frictional work of interfacial motion. Based on this model, Cohen and Olson [2] derived the cumulative structural defect potency distribution $N_V(n)$, from the Cech and Turnbull small particle experiments in Fe-30 Ni [3]:

$$N_V(n) = N_V^o \exp(-\alpha n) \qquad (2)$$

where α is a constant distribution shape factor and N_V^o is the total number of nucleation sites of all potencies. Combining Eq. (1) and Eq. (2), the thermodynamic potency distribution $N_V(\Delta g)$ can be expressed as:

$$N_V(\Delta g) = N_V^o \exp \frac{2\alpha\gamma_s/d}{\Delta\gamma^{ch} + E^{Str} + W_f} \qquad (3)$$

The effect of applied stress on the potency distribution can be found by adding a mechanical driving force term Δg^{σ} to the chemical driving force term Δg^{ch} of Eq.(3), to obtain the total driving force

$$\Delta g = \Delta g^{ch} + \Delta g^{\sigma} \qquad (4)$$

At a given stress level, the value of Δg^{σ} changes with the orientation of the nucleus relative to the stress axis.

The mechanical driving force due to a uniaxial elastic stress σ is then expressed as:

$$\Delta g^{\sigma} = \frac{\sigma}{2} \{\gamma_o \sin 2\theta \cos\alpha + \varepsilon_o(1 + \cos 2\theta)\} \qquad (5)$$

where γ_o and ε_o are the transformation shear and normal strains, θ is the angle between the applied stress axis and the normal to the habit plane, and α is the angle between the shear direction of the transformation and the maximum shear direction of the applied stress resolved on the habit plane.

In considering stress effects on the potency distribution two limiting cases should be considered. A fully-biased distribution corresponding to the assumption by Patel and Cohen [4] that all operating nucleation sites are of the optimum orientation for maximum interaction with the applied stress such that $\Delta g^{\sigma} = \Delta g^{\sigma}_{max}$ for all active sites. An opposite extreme is a fully-random distribution, based on the assumption made by Olson, Tsuzaki, and Cohen [5] that the nucleation sites are randomly oriented. The actual behavior should be bounded by these two extremes. Olson and Tsuzaki also found that in the stress-assisted regime the effect of the applied stress is approximately one third of that predicted by the fully-biased distribution model. Therefore, the potency distribution of nucleation sites $N_V(\sigma)$, under an applied elastic stress σ is given by the following expression:

$$N_V(\sigma) = N_V^o \exp \frac{2\alpha\gamma s/d}{\Delta g^{ch} + \Delta g^{\sigma}_{max} + E^{Str} + W_f} \qquad (6)$$

where for the fully-random distribution of nucleation sites, the term Δg^{σ}_{max} should be replaced by $\Delta g^{\sigma}_{max}/3$.

The stress-assisted transformation of a well-spaced dispersion of metastable particles in a stable matrix is controlled by the pre-existing nucleation sites for which the potency distribution under an applied elastic stress σ is given by Eq. (6). For an average particle volume V_p, the fraction of particles f to transform via sites of a

potency with a cumulative number density N_V, will be.

$$f = 1-\exp\ (-N_V \cdot V_p) \qquad (7)$$

From Eq. (1), the stress σ required to operate a nucleation site of potency n_o is linearly related to a parameter of the form:

$$\phi = [\sigma(-\partial\Delta g/\partial\sigma) - (\Delta g^{ch}+E^{Str}+W_f)](d/2\gamma_s)=n_o^{-1} \qquad (8)$$

For the potency distribution of Eq. (2), f and ϕ are lated by:

$$\phi = \alpha/\ell n[-N_V^o\ V_p/\ell n(1-f)] \qquad (9)$$

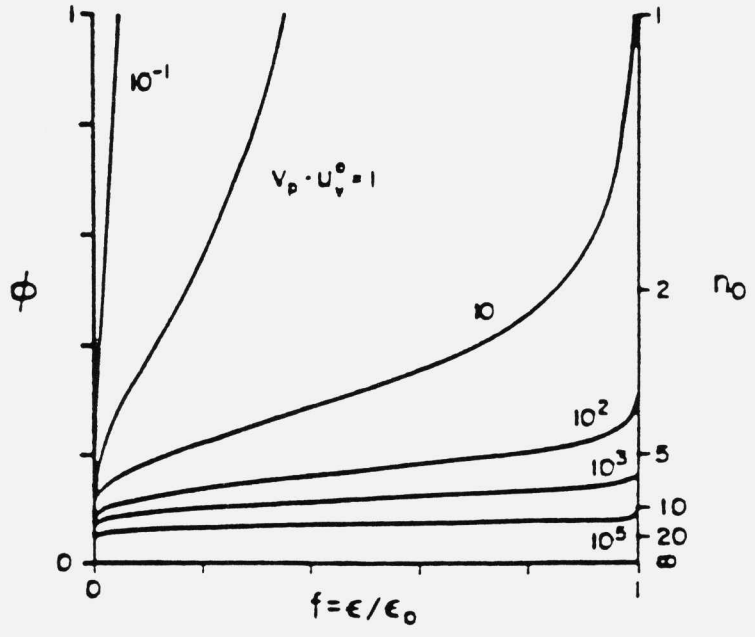

Fig. 2 Computed σ-ε curve shapes for dispersed-phase transformation plasticity from non-interacting particles of various size [5].

Taking the plastic strain ε to be proportional to f with complete transformation giving a strain ε_o, the form of the σ-ε curves predicted for various values of V_p normalized to $(N_V^o)^{-1}$ are shown in Fig. 2. For small particles, a high strain-hardening rate arises from early exhaustion of the most potent sites, and further strain requires operation of less potent sites at higher stresses. The sigmoidal shape of the σ-ε curves for stress-assisted transformation has been also observed for transformation plasticity in certain ceramic systems. Recent experiments by Chen and Reyes [6] have deomonstrated sigmoidal σ-ε curves under combined pressure and uniaxial stress, in MgO-partially stabilized zirconia ceramics.

Despite the high strain-hardening rates associated with site exhaustion, stress-assisted transformation ($T<M_S^\sigma$) represents a softening phenomenon relative to the flow behavior of the parent phase in the absence of transformation. Above M_S^σ, where strain-induced nucleation dominates the transformation behavior, transformation and slip act as parallel deformation mechanisms. While a softening effect is still associated with the operation of the transformation as a deformation mechanism (dynamic softening), a hardening effect also arises from the transformation product as an obstacle to slip (static hardening). These two effects have been separated by prestrain experiments, providing empirical constitutive relations for transformation plasticity [7]. A general characteristic of transformation plasticity is that dynamic softening has the dominant effect at low strains, while the static hardening dominates at high strains as the rate of transformation diminishes. The combined effect of ideal "exponential hardening" behavior imparts maximum flow stability.

The flow stabilizing influence of transformation plasticity has been demonstrated experimentally for retained austenite in dual-phase steels [8]. High-magnetic-field cryogenic treatments were used to vary the amount of austenite, in an intercritically annealed 0.11C-0.55Si-1.4Mn steel. The tensile σ-ε curves are shown in Fig. 3. Curve A represents the as-heat-treated material, while curve B depicts the magnetic-field-treated control material. Curves AT and BT represent specimens identically treated as A and B but tempered for 1h at 180°C to fully age the dislocation substructures in order to eliminate possible complications arising from additional mobile dislocations introduced by

the magnetically-induced martensitic transformation in the B specimen. The amount of retained austenite as a function of plastic strain is also plotted in the same figure. The data in Fig. 3 allow comparison of the flow behavior of materials with the same UTS and identical martensite contents at the UTS but with a difference in initial austenite content of $\Delta f = 0.05$. The transformation plasticity associated with transformation of this amount of austenite provides an additional increment of uniform ductility of 4 to 5% strain. The curve-shaping influence of relatively modest austenite contents is clearly a potent mechanism for enhanced control of the stability of plastic flow.

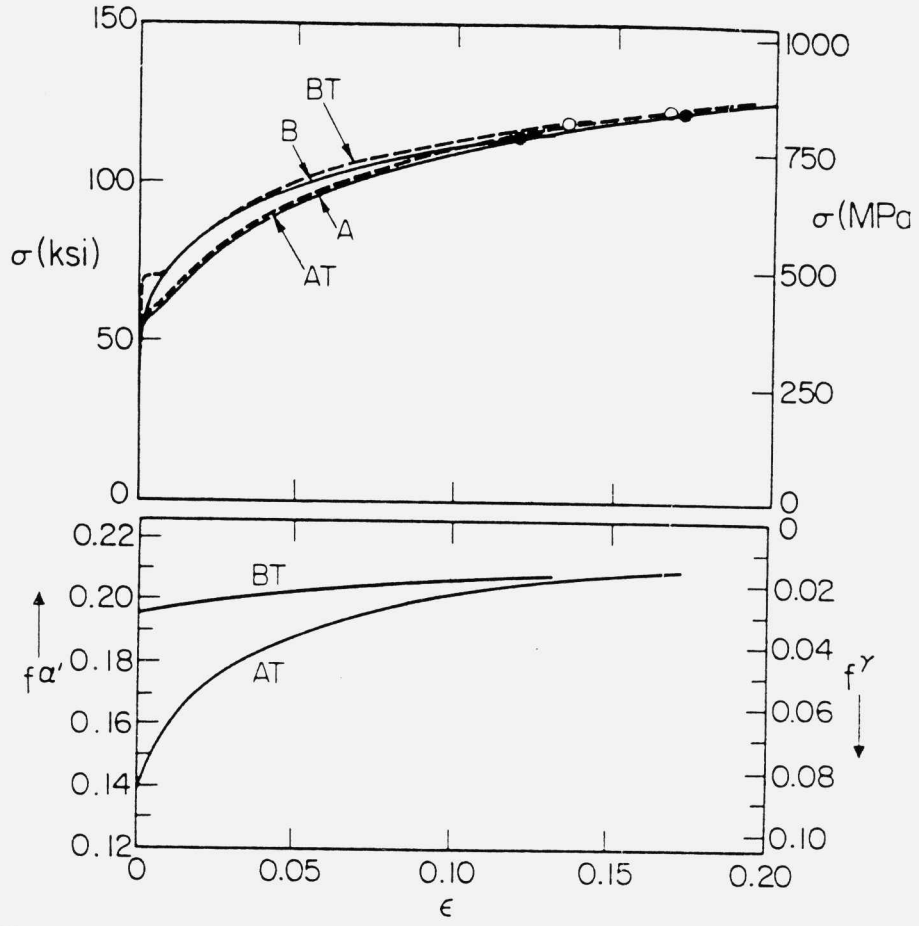

Fig. 3 True σ-ε curves and corresponding martensite contents during tensile deformation of dual-phase steel; curve A, as heat treated; curve B, magnetic-field treated; curves AT and BT, tempered 1/2 hr. at 180°C. Solid and open points indicate necking strains [8].

Transformation Toughening

The concept of dispersed-phase transformation toughening has been thoroughly investigated only for brittle solids failing by cleavage [9]. The most familiar example is the partially-stabilized zirconia ceramics (PSZ), where the metastable tetragonal precipitate is biased to transform to the nonoclinic product phase by the intensified stress field ahead of a crack-tip. The toughness improvement in these systems has been rationalized in terms of the additional dissipative work of the applied stress [10]. More recent models [11], indicate that the observed toughening is due to a reduction in the effective local stress intensity, caused by the volume change of the transformed particles which are left in the wake of the moving crack tip.

In ductile solids such as ferrous alloys, transformation toughening of homogeneous materials has been investigated and led to the development of TRIP steels [12]. Recent experiments in metastable austenitic steels have demonstrated that the flow-stabilizing influence of transformation plasticity can substantially enhance fracture toughness when fracture is controlled by shear instability [13]. Fig. 4 summarizes the measured increment of J-integral toughness enhancement ΔJ_{Ic} relative to the toughness of the stable austenite $J_{Ic}{}^{A}$, as a function of relative transformation stability, for a series of precipitation-hardened metastable austenitic steels. The relative transformation stability is expressed by a normalized temperature parameter, θ, given by:

$$\theta = \frac{T - M_s{}^{\sigma}}{M_d - M_s{}^{\sigma}} \qquad (10)$$

with $\theta > 1$ ($T < M_d$) corresponding to stable austenite and $\theta \leq 0$ ($T \leq M_s{}^{\sigma}$) corresponding to stress assisted transformation. Both the $M_s{}^{\sigma}$ and M_d temperatures were experimentally determined for the stress state ahead of the crack tip. The shape of the $\Delta J_{Ic}/J_{Ic}{}^{A}$ vs θ behavior for shear instability controlled fracture is consistent with the effect of transformation plasticity on flow stability, indicating an optimum amount of crack-tip transformation near the $M_s{}^{\sigma}$

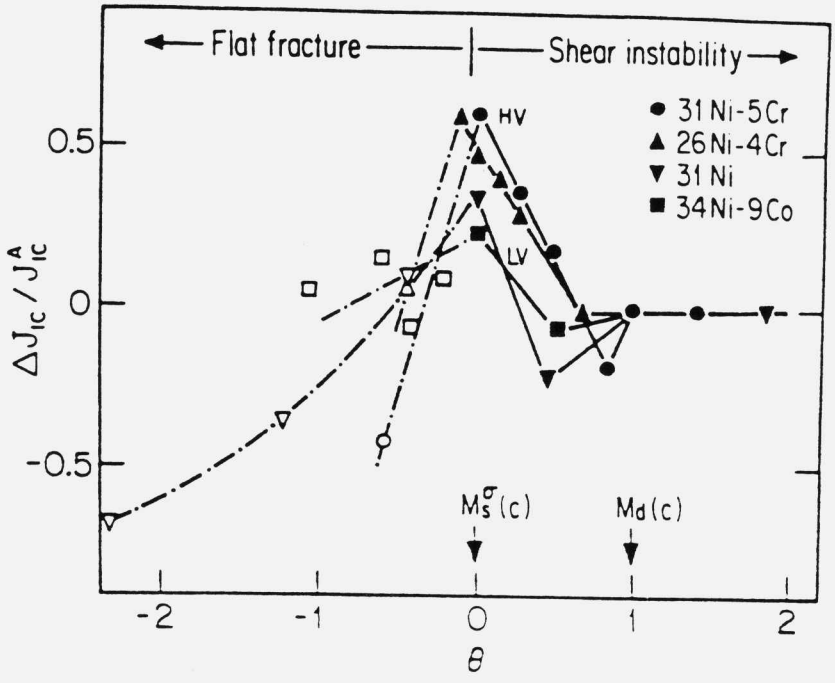

Fig. 4 Relative enhancement of J-integral toughness vs normalized temperature for TRIP steels [13].

temperature. Curves labeled HV in Fig. 4 represent alloys with a relatively high transformation volume change of 4%, while LV represents a lower volume change of 2.5%. Toughness enhancement is clearly increased by a larger volume change. However, extrapolation of observed behavior to $\Delta V=0$ suggests that even in the absence of dilatation, the σ-ε curve-shaping effect of transformation plasticity will delay shear instability.

Recent observations [14] of martensite forming around void-nucleating carbide particles during tensile deformation of a homogeneous metastable austenitic steel, suggest that transformation toughening can arise by delaying microvoid nucleation to higher strains.

AUSTENITE STABILIZATION

The transformation behavior of the dispersed austenite is determined by the stability of the austenite particles. A quantitative measure of the austenite stability is the critical driving force required to transform the austenite particle*. Invoking Eq. (4) and rearranging Eq. (8) we get (11):

$$\Delta g_C = (\Delta g^{ch} + \Delta g^{\sigma})_C = - E^{Str+Wf} + \frac{2a\gamma_s}{d[\ell n \ell n(1-f)^{-1} - \ell n(N_V^0 V_p)]}$$

where Δg_C is the critical driving force for transformation to a fraction f.

From Eq.(11) the most important parameters controlling the stability of the dispersed austenite can be identified. Size refinement (decreasing V_p) increases Δg_C and therefore enhances the stability of dispersed austenite. On the other hand, compositional enrichment of the austenite particles with γ-stabilizing solute elements reduces the chemical driving force. Solute enrichment also increases W_f, the frictional work of interfacial motion due to solution hardening of the austenite by the solute elements.

The size effect has been verified experimentally by Rigsbee [15]. He has shown that during strain-induced transformation the average untransformed austenite particle size decreased rapidly with plastic strain. These submicron-size austenite particles were precipitated during intercritical annealing of a low-alloy steel. There is recent evidence [16,17] that size refinement and compositional enrichment can be achieved by using a dispersion of alloy-enriched carbides as a nucleation site for the austenite. In a heat treatment developed by Rao [16], a microalloyed steel with 0.16C and 1.5 Mn (w/o) was tempered below the A_1 temperature to partition Mn and C and to form fine, lenticular cemenite particles. During intercritical annealing austenite nucleated on the cementite particles which dissolved, thus enriching the austenite with C and Mn and enhancing the austenite stability.

A different approach was taken by Kim and Morris [18] in enriching the austenite particles with γ-stabilizing solutes.

*The assumption is made here that the particle transforms completely from a single nucleation event.

In their 5.5 Ni steel a two-step heat treatment was used to stabilize the austenite. The austenite formed during the second low-temperature step on the lath boundaries of the martensite which had been previously enriched in Ni during the first high-temperature step.

In assessing the effects of particle size and composition on the transformation behavior, a measurable quantity is needed to characterize the stability of dispersed austenite. For deformation-induced martensitic transformation, the M_S^{σ} temperature represents a single-parameter characterization of the austenite stability. It was discussed earlier in this paper, that the M_S^{σ} temperature is a function of stress state. Therefore it has to be determined for each stress state of interest. These measurements are discussed in the next section.

RETAINED AUSTENITE

Materials and Experimental Procuedures

The alloy system selected to study the transformation plasticity effects associated with retained austenite was a VAR 4340 steel. The composition of the alloy is shown in Table 1. Controlled experiments were designed in order to isolate the role of retained austenite. For this purpose high-magnetic-field, cryogenic treatments were used to reduce the amount of retained austenite in otherwise identically heat treated specimens. Two solution treatments were used, 870°C and 1200°C for 1h. The specimens were oil-quenched and tempered at 200°C for 1h. The amount of retained austenite was determined by measuring the saturation magnetization of pre-weighted samples, using a vibrating sample magnetometer. Table 2 shows the four different treatments used, the resulting volume fraction of retained austenite and corresponding hardness. Tension, compression, thin-wall torsion and K_{Ic} testing was carried out using an INSTRON 1125 testing machine. Tensile specimens were consistent with TR-6 specifications. Cylindrical compression specimens were used with 15mm length and 6mm diameter. K_{Ic} fracture toughness was determined using three-point bend specimens (L-T orientation) according to ASTM E-399 [19].

TABLE 1

COMPOSITION OF VAR 4340 STEEL (in wt%)

C	Ni	Mo	Cr	Mn	Si	P	S
0.42	1.74	0.21	0.89	0.46	0.28	0.009	0.001

TABLE 2

CONTROLLED TREATMENTS FOR 4340 STEEL

AUSTENITIZING TEMPERATURE	TREATMENT	VOLUME FRACTION RETAINED AUSTENITE	HARDNESS RC
870°C	200°C/1HR	4.0	54.0
870°C	20 TESLA/1HR-196°C 200°C/1HR	2.5%	53.5
1200°C	200°C/1HR	9.1	53.3
1200°C	20 TESLA/1HR/-196°C 200°C/1HR	6.8	53.4

Characterization of Retained Austenite Stability M_S^σ Temperature

It was mentioned earlier that the M_S^σ temperature provides a quantitative characterization of the stability of dispersed austenite. For this purpose, the M_S^σ temperature was measured in uniaxial tension, M_S^σ(u.t), and uniaxial compression, M_S^σ(u.c.). A single specimen technique, originally developed by Bolling and Ritchman [20] was used. The temperature dependence of the 0.2% flow stress in tension and compression are shown in Fig. 5a for the material containing 9% retained austenite (1200°C austenitizing temperature). Both flow stresses increase with decreasing temperature as expected from the thermally-activated flow theory. However, the tensile flow stress undergoes a plateau region, starting at about 40 to 50°C. At this temperature yield-point phenomena appear, which increase in magnitude with decreasing temperature. These yield points should not be attributed to strain aging, which being thermally activated, should disappear with decreasing temperature.* They are, instead, attributed to mechanical relaxations associated with the transformation of retained austenite. It is important to note the absence of a complete reversal of the flow stress such as the one shown schematically in Fig. 1. This can be explained by the fact that the 0.2% flow stress is a composite flow stress, controlled by the flow properties of both martensite and retained austenite. Therefore, the M_S^σ (u.t.) temperature corresponds to the onset of the plateau region and yield-point phenomena (40-50°C). Smooth yielding dominates the compressive flow stress down to about -15°C where again the yield-point phenomena appear. As before, we get M_S^σ (u.c) = -20 to -30 C.

The corresponding results for the material that contains 4% retained austenite (870°C austenitizing temperature) are shown in Fig. 5b. A plateau region is absent in this case due to the much lower amount of retained austenite. However, the tensile flow stress undergoes an inflection at about 10 to 20°C. The transition from smooth yielding to yield-point phenomena also occurs in the same temperature range, indicating that M_S^σ(u.t) = 10 to 20 C. No yield-points were observed for the compressive flow stress indicating that M_S^σ (u.c)< -50 C.

*The hold between each loading cycle was kept constant in these tests.

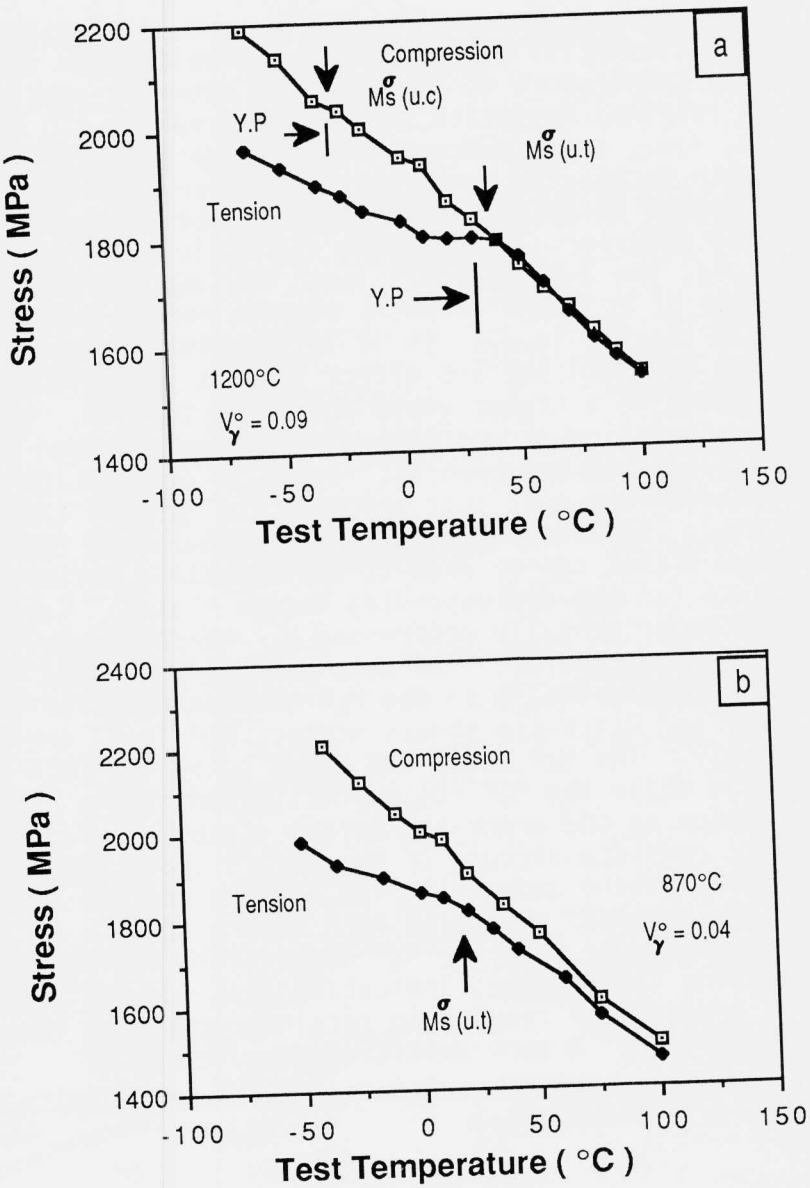

Fig. 5 Temperature dependence of 0.2% tensile and compressive flow stresses determined with the single-specimen technique, indicating the M_S^σ temperatures. Y.P. indicates the occurence of yield-point phenomena. Fig. 5a is for the 1200°C austenitizing temperature, while Fig. 5b is for the 870°C austenitizing temperature.

From the flow stresses in tension and compression, the strength-differential effect (S-D)* was calculated and plotted vs temperature in Fig. 6. The material that contains 4% retained austenite exhibits the normal S-D effect behavior, i.e., a few percent in magnitude and increasing slowly with decreasing temperature. However, the material that contained 9% retained austenite exhibits a quite different S-D behavior. Approaching the M_S^σ(u.t.) from high temperature, the S-D undergoes local minimum and then assumes high values of up to 7% where it shows a second local minimum at the M_S^σ (u.c). It is interesting to note that around the M_S^σ(u.t) the S-D effect assumes negative values, corresponsing to a higher yield stress in tension. Such "pre-transformation strengthening" has been observed also in TRIP steels and has been attributed to dislocation core structure rearrangement just prior to the general transformation [21]. The local minima in the temperature dependence of the S-D effect can be used to approximately define the M_S^σ temperature for the corresponding stress states. Table 3 shows the experimentally determined M_S^σ temperatures for tension and compression. Two more entries are shown in the same table corresponding to the M_S^σ temperatures for the pure shear and crack-tip stress states, M_S^σ (p.s) and M_S^σ(C), respectively. The M_S^σ (p.s) was taken to be 1/2 [M_S^σ (u.t) +M_S^σ (u.c)] while the M_S^σ (C) was estimated from a simple extrapolation to the crack-tip stress state. Table 3 gives a relatively complete picture of the stress state dependence of the M_S^σ temperature underlying the varying degress of stability of the retained austenite with stress state. It is interesting to note that the M_S^σ temperature varies with the austenitizing temperature, indicating that the low austenitizing temperature results in retained austenite of a higher stability. A more sensitive measurement of M_S^σ temperature based on monitoring the elastic limits is presented in the appendix.

Plastic Flow Stabilization in Pure Shear

One of the most important effects of tranformation plasticity is the stabilization of plastic flow. In pure shear deformation, the strain-induced transformation of

*The S-D effect is defined as $SD=2(\sigma_c-\sigma_t)/(\sigma_c+\sigma_t)$ where σ_c and σ_t are the compressive and tensile flow stresses respectively.

TABLE 3

M_s^{σ} TEMPERATURES FOR RETAINED AUSTENITE IN 4340 STEEL
DETERMINED BY THE SINGLE-SPECIMEN TECHNIQUE

Austenitizing Temperature	Volume fraction Ret. Austenite	Tension M_s^{σ} (u.t)	Compression M_s^{σ} (u.c)	Pure Shear M_s^{σ} (p.s)	Crack-tip M_s^{σ} (c.)
1200°C	0.09	45+5°C[1] 47+27°C[2]	-25+5°C[1] -37+17°C[2]	7.5°C	>150°C
870°C	0.04	15+5°C[1]	<-50°C[1]	<-17°C	>150°C

1. Determined from onset of plateau region and yield-point phenomena
2. Determined from loal minima in the S-D effect

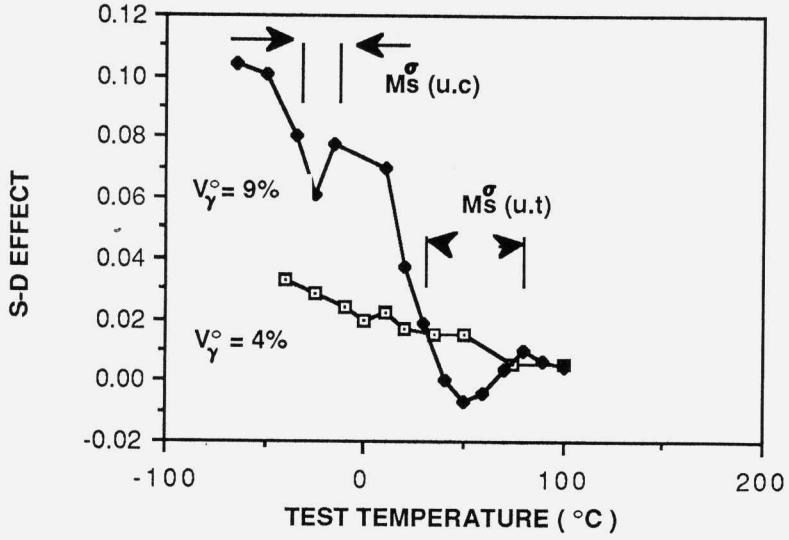

Fig. 6 Temperature dependence of the strength-differential (S-D) effect for two different volume fractions of retained austenite in 4340 steel. Arrows indicate M_S^σ temperature ranges.

retained austenite can delay shear localization to higher strains. These effects were investigated with controlled experiments where the amount of retained austenite was varied using the high-magnetic-field cryogenic treatments described and summarized in Table 2. Thin-wall torsion testing was performed for the four conditions listed in Table 2. The tests were run at room temperature, i.e., above the estimated M_S^σ (p.s) shown in Table 3 to ensure a high stability of retained austenite against stress-assisted transformation. The shear stress-strain curves to the point of instability are shown in Fig. 7a and Fig. 7b for the 870°C and 1200°C austenitizing temperatures, respectively. A delay in shear instability is associated with the higher amounts of retained austenite. The increase in shear-instability strain is of the order of 25 to 30%. It should be emphasized that the amount of retained austenite

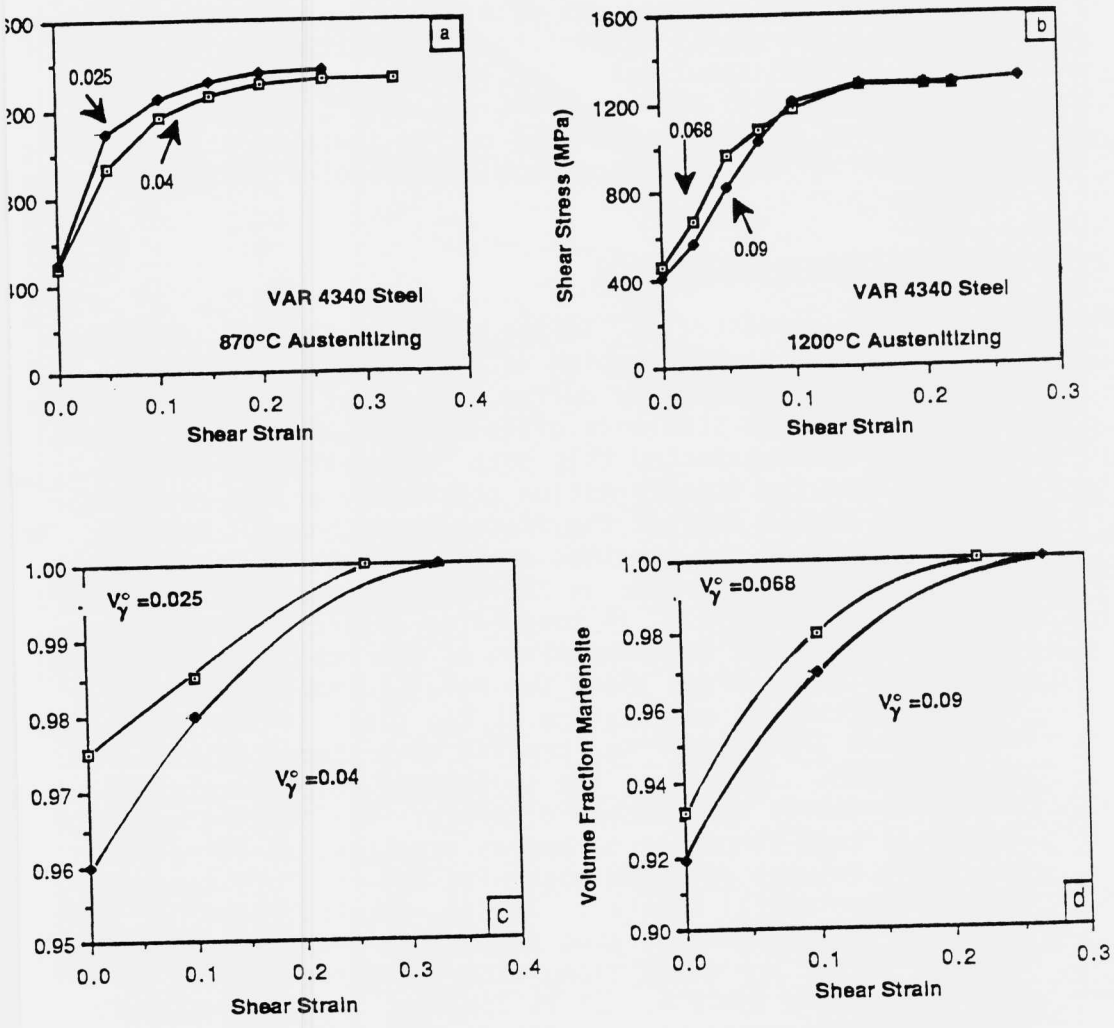

Fig. 7 Stress-strain curve (a,b) and corresponding martensite contents (c,d) during pure-shear deformation of 4340 steel. (a),(c) are for the 870°C austenitizing while (b),(d) are for the 1200°C austenitizing temperature.

was the only variable in these experiments. The specimens have otherwise received identical heat treatments resulting in identical hardness.* Retained austenite content as a function of shear strain was determined by saturation magnetization measurements after interrupted straining of identically treated specimens. The results are shown in Fig. 7(c) and Fig. 7(d) for the 870°C and 1200°C austenitizing temperatures, respectively. The curves indicate a complete exhaustion of the transformation at the point of shear instability.

Implications on Toughening

It was demonstrated, in the previous section, that the strain-induced transformation of the retained austenite delayed shear instability during pure shear testing. Since fracture in these steels is often controlled by shear localization, it is expected that such "delocalizing" effects arizing from the transformation plasticity of the retained austenite should enhance the fracture toughness. However, the stability of the retained austenite for the crack-tip stress-state is very low, as indicated by the high M_S^{σ} (C) temperature in Table 3. A toughening effect asociated with the strain-induced transformation of the retained austenite would only be observed above the M_S^{σ} (C) temperature, i.e., above 150°C. This temperature is too close to the tempering temperature (200°C) for K_{Ic} testing of a stable material to be performed. Therefore, the toughening role of retained austenite cannot be assessed directly. K_{Ic} testing was performed at room temperature, and as expected, no correlation was found between retained austenite and fracture toughness beyond experimental scatter. The K_{Ic} results, together with the shear instability strains determined from the thin wall torsion tests, are given along with the corresponding M_S^{σ} temperatures in Table 4. It is apparent from this table that retained austenite is sufficiently stable for the pure-shear stress state but unstable for the crack-tip stress state, when testing is performed at room temperature. Transformation toughening can result only by lowering the M_S^{σ} (C) below room temperature by stabilizing the austenite. This can be achieved in the "precipitated" austenite which can be stabilized by size refinement and compositional enrichment, using multi-step heat treatments.

*Any additional mobile dislocations introduced by the magnetically induced martensitic transformation are fully "aged" after tempering to 200°C for 1h.

TABLE 4

SHEAR INSTABILITY STRAINS AND K_{IC} FRACTURE TOUGHNESS FOR 4340 STEEL

Aust. Temp.	Vol. Fraction Retained Aust.	Shear M_S^{σ}(p.s)	Shear Instab. Strain	Crack-Tip M_S^{σ}(c)	K_{IC} (Ksi.in$^{1/2}$)
870°C	0.04	<17°C**	0.34	>150°C**	48/4 (+1.5,-1.0)
870°C	0.025		0.27		47.1 (+1.8,-2.1)
1200°C	0.09	7.5°C	0.28	>150°C	84.5*
1200°C	0.068		0.22		84.4 (13.8,-10.)

* The reported value is K_Q
**Estimated values

PRECIPITATED AUSTENITE

Precipitated austenite is the form of dispersed austenite that precipitates on tempering or intercritical annealing. We have already discussed the roles of size refinement and compositional enrichment in the stability of precipitated austenite. We next discuss multi-step heat treatments for austenite stabilization, and some preliminary results on the transformation toughening associated with precipitated austenite.

Materials and Experimental Procedures

The alloys selected for this study were a conventional AF1410 steel and a modified 1410-4Mo steel. The compositions of the steels are shown in Table 5. Austenite precipitation during tempering was monitored with resistivity and saturation magnetization measurements. The austenite volume fraction was measured with standard X-ray diffraction techniques. The austenite dispersions were identified using bright field/dark field imaging (BF/DF) in a JEOL 200CX TEM operating at 200 KV. The chemical composition of the austenite particles was measured using high resolution STEM microanalysis in a VG HB5 STEM operating at 100 KV. Convergent beam electron diffraction (microdiffraction) was used to identify the austenite particles in the STEM. Standard Charpy specimens were used to measure the notch toughness of the heat treated specimens.

Single Tempering Treatments

Austenite precipitation during tempering was monitored by measuring the resistivity and saturation magnetization changes of heat treated specimens relative to the as-quenched condition. Fig. 8 shows the changes in relative resistivity with tempering time for the 1410-4Mo tempered at 500°C. The upper curve in Fig. 8 shows the relative resistivity at 500°C. After an initial drop of the resistivity due to carbide precipitation, the resistivity rises due to austenite precipitation. The resistivity continues to increase with time as more austenite precipitates at 500°C. The intermediate curve in Fig. 8 shows the resistivity changes that occur after the specimens have been tempered

TABLE 5

COMPOSITIONS (in wt%) of AF1410 and 1410-4Mo STEELS

	C	Co	Ni	Mo	Cr	Mn	Si	P	S
AF14120	0.16	14.25	10.15	1.05	2.10	0.02	0.01	0.003	0.002
1410-4Mo	0.29	14.05	10.20	3.88	0.01	<0.01	<0.01	0.005	0.003

and then cooled to room temperature (25°C). After an initial drop of the resistivity as before, a local maximum is observed at 8h of tempering time. This is because the austenite that forms after 8h of tempering at 500°C is unstable and transforms to martensite when cooled to room temperature, thus decreasing the resistivity after 8h. The bottom curve shows the resistivity changes with tempering time for specimens tempered at 500°C and then cooled to liquid nitrogen temperature. The behavior is similar with that of the previous curve, however, the peak height at 8h has decreased in magnitude indicating further transformation of the precipitated austenite upon cooling to -196°C. This experiment demonstrates that on simple tempering relatively stable austenite precipitates between 5 and 8h, but since this austenite transforms on cooling to -196°C, it is not expected to be stable enough for transformation toughening effects.

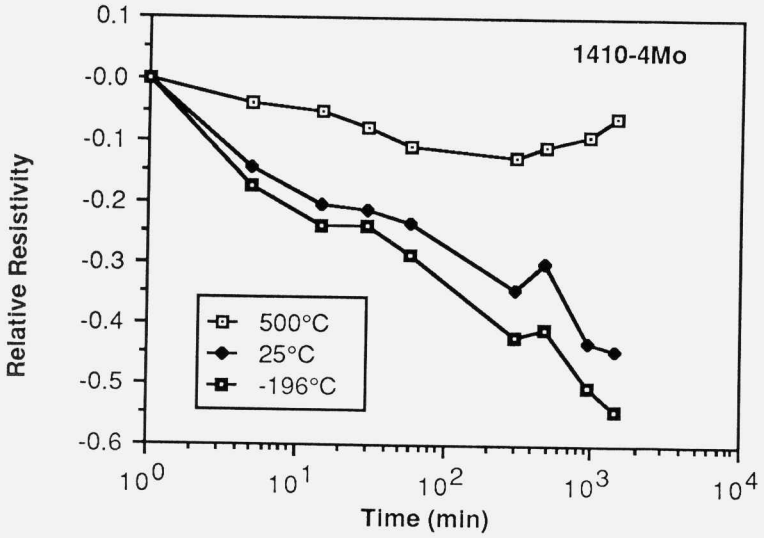

Fig. 8 Relative restivity as a function of tempering time for 1410-4Mo steel tempered at 500°C. The three curves correspond to measurement performed at 500°C. 25°C, and -196°C, respectively.

The austenite precipitation behavior in 1410-4Mo was monitored also with saturation magnetization measurements. Fig. 9 shows the relative resistivity and magnetization changes with tempering time for specimens tempered at 500°C and then cooled to room temperature. Due to the paramagnetic nature of the austenite, the saturation magnetization decreases when austenite precipitates. The minimum in the saturation magnetization curve corresponds to stable austenite precipitation and occurs at 8h consistent with the behavior of the resistivity.

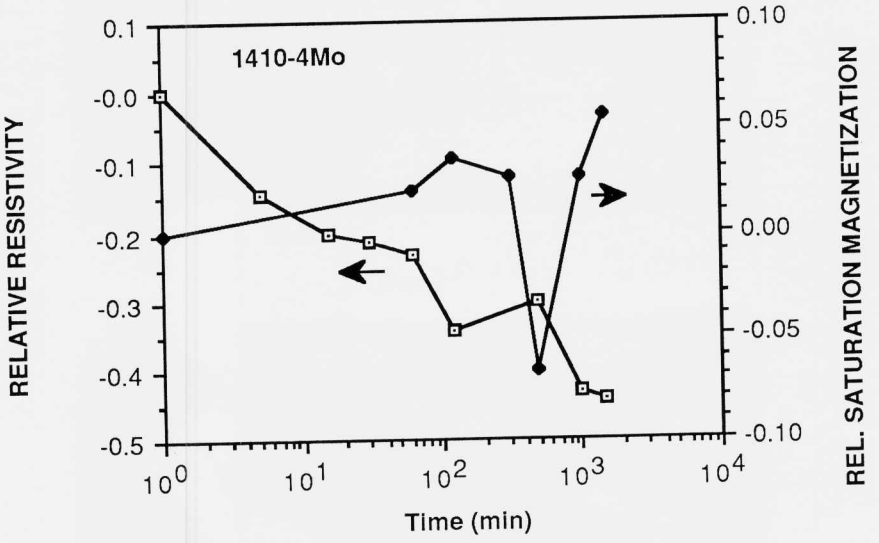

Fig. 9 Relative resistivity and saturation magnetization as a function of tempering time for 1410-4Mo steel tempered at 500°C and cooled to room temperature.

TEM observations revealed that the austenite in the 1410-4Mo precipitates on the lath boundaries of the martensitic matrix. Fig. 10 shows a BF/DF image of interlath austenite films for specimens tempered for 8h at 500°C. Note that at this tempering time the size of the films is still quite small. However, after tempering above 8h the films grow and lose stability. This is shown in Fig. 11 which corresponds to 13h at 500°C and indicates that particles link together at the same lath boundary and form a relatively long austenite film resulting in loss of austenite stability. These TEM observations are consistent with the resistivity results discussed earlier, indicating loss of austenite stability after 8h of tempering.

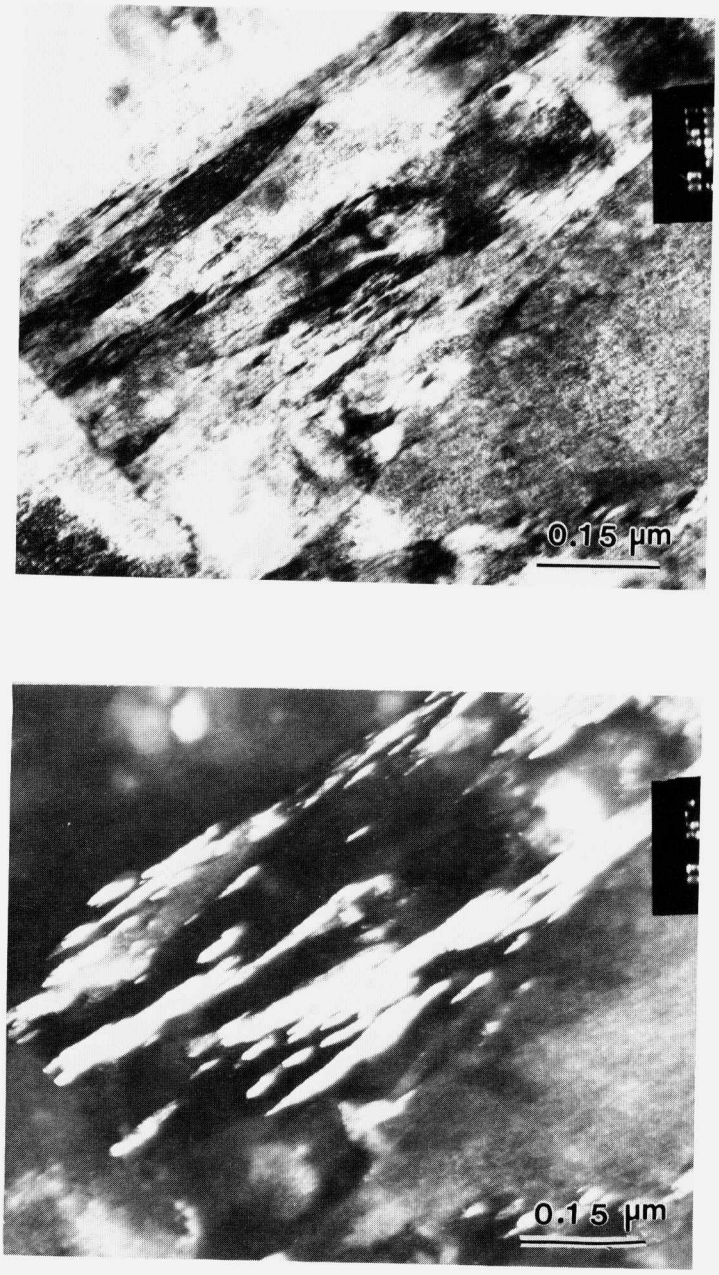

Fig. 10 TEM micrograph showing a Bright/Dark field image of interlath austenite films. 1410-4Mo steel tempered at 500°C for 8h.

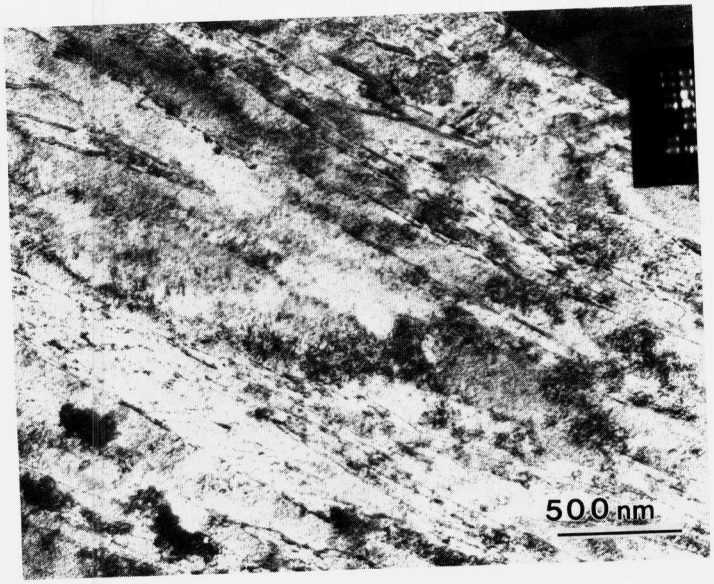

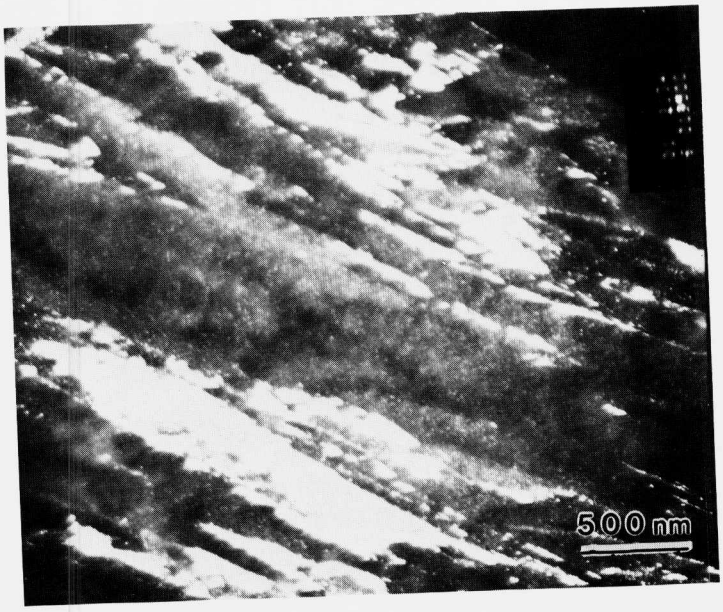

Fig. 11 TEM micrograph showing a Bright/Dark field image of interlath austenite films. 1410-4Mo steel tempered at 500°C for 13h.

Austenite volume fraction was measured using X-ray diffraction techniques and the results are shown in Fig. 12 for AF1410 steel. Fig. 12a shows the volume fraction of austenite as a function of tempering temperature for 5h of tempering time. The curve labeled RT corresponds to measurements performed after the specimens were quenched to room temperature from the indicated tempering temperature. The curve labeled LN corresponds to measurements performed after the specimens were further cooled to liquid nitrogen temperatures. The difference between these two curves gives a good indication of the thermal stability of the precipitated austenite. Austenite that forms between 500 and 600°C is very stable and loses stability for higher tempering temperature. Fig. 12b shows the volume fraction of precipitated austenite vs tempering time for 500°C and 650°V tempering temperatures. Fig. 12b indicates that stable austenite precipitates at short tempering times. The above results suggest that stable austenite dispersions form on simple tempering when low temperatures and short tempering times are used. However, under these conditions the amount of austenite is relatively low. A combination of high amounts and stability can be achieved only through multi-step heat treatments aimed at size refinement and compositional enrichment of the austenite dispersion. This topic is treated in the next section.

Multi-Step Heat Treatments for Austenite Stabilization

Heat treatment for austenite stabilization is directed at size refinement and compositional enrichment of the austenite particles in stabilizing solutes. Two methodologies were used to achieve this goal.

First, a fine dispersion of intralath austenite can form if a second dispersed phase can be used as a nucleation site for the austenite. Furthermore, if this phase can be previously enriched in stabilizing solutes, then the austenite will inherit a considerable amount of these elements and be chemically stabilized. In the present study, a dispersion of alloy enriched cementite was used for heterogeneous nucleation of the austenite. The cementite was precipitated at a low temperature step (420°C) while the austenite was formed at a higher temperature step (510°C). The resulting austenite is termed cementite-nucleated austenite.

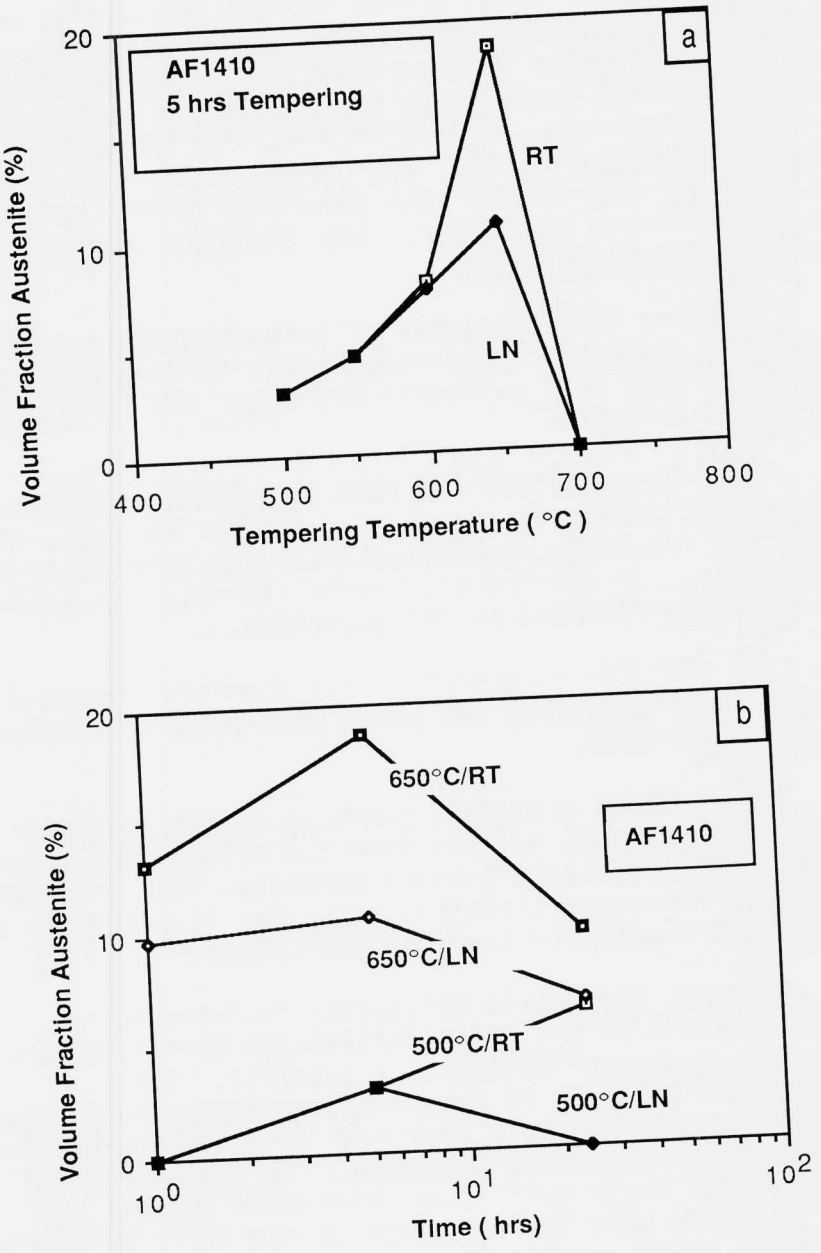

Fig. 12 Volume fraction of precipitated austenite in AF1410 steel as a function of tempering temperature (a) and tempering time (b). Curves RT correspond to material quenched to room temperature, while LN corresponds to material quenched to liquid nitrogen temperature.

On the other hand, a fine uniform dispersion of intralath austenite can form directly by increasing the driving force for austenite precipitation. This was achieved by a short-time high temperature step (600°C/15 min) followed by a lower temperature step (510°C/8h). An additional feature of this treatment is that the diffusivity of Ni is enhanced at the high temperature step resulting in high Ni-enrichment of the austenite particles. The resulting austenite is termed direct-nucleated.

A common characteristic of both treatments is the formation of interlath austenite. Later in this section we will show that this austenite has lower stability than the intralath austenite.

Table 6 summarizes the heat treatments used for austenite stabilization in the AF1410 steel. The table also lists the resulting hardnesses after the completion of these treatments. In all the treatments the solution temperature was 830°C/1h followed by oil quenching.

The 510°C/5h treatment is the standard treatment for AF1410 steel providing the best combination of strength and toughness to date.

The 510°C/8h treatment produces stable austenite on simple tempering as evident from the resistivity, magnetization and TEM results discussed earlier. This treatment was used as a reference treatment since the last step in all multi-step treatments used was 510°C/8h.

The next two double treatments in Table 6, 420°C/1h+510°C/8h and 420°C/5h+510°C/8h correspond to the cementite-nucleated austenite treatments. The 600°C/15min+510°C/8h is the direct-nucleated austenite treatment and the triple treatment 420°C/1h+600°C15min +510°C/8h is a combined treatment. It is interesting to note that these multi-step treatments possess the same hardness with the exception of the 420°C/5h+510°C/8h treatment which results in considerable hardening. We will now focus on the 420°C/5h+510°C/8h and 600°C/15min+510°C/8h treatments because they reflect the general characteristics of cementite-nucleated and direct-nucleated austenite treatments.

TABLE 6

HEAT TREATMENTS FOR AUSTENITE STABILIZATION IN AF1410 STEEL

TREATMENT	HARDNESS (R_C)	REMARKS
510°C/5h	48	Standard Treatment
510°C/8h	46	Slightly Overaged
420°C/1h 510°C/8h	48	Cementite-Nucleated Austenite
420°C/5h 510°C/8h	51.5	"
600°C/15min 510°C/8h	48	Direct-Nucleated Austenite
420°C/1h 600°C/15min 510°C/8h	48	Combined Treatment

NOTE: Austenitizing temperature 830°C/1h

Cementite-nucleated austenite treatment (420°C/5h+510°C/8h)

As mentioned before, the purpose of this treatment is to produce a fine dispersion of stable intralath austenite by heterogeneous nucleation on alloy-enriched cementite. Table 7 shows high resolution STEM microanalysis results obtained for this treatment. At 420°C/5h a dual dispersion of cementite forms: Mo-rich and Cr-rich cementite. Then at 510°C, the Mo-rich cementite dissolves completely to form the M_2C carbide strengthening dispersion while the Cr-rich cementite stabilized by Cr does not dissolve. A fine dispersion of intralath austenite nucleates then on the Cr-rich cementite particles at 510°C. Fig. 13 shows a STEM micrograph indicating multiple nucleation of austenite particles from a single cementite particle. The compositions of the austenite particles together with the compositions of the cementite particles that they nucleated on are given in Table 7. The results indicate a considerable Ni enrichment of the austenite particles to about 19w/o and a concurrent depletion of Ni in the cementite particle indicating solute transfer from the cementite to the austenite. The resulting

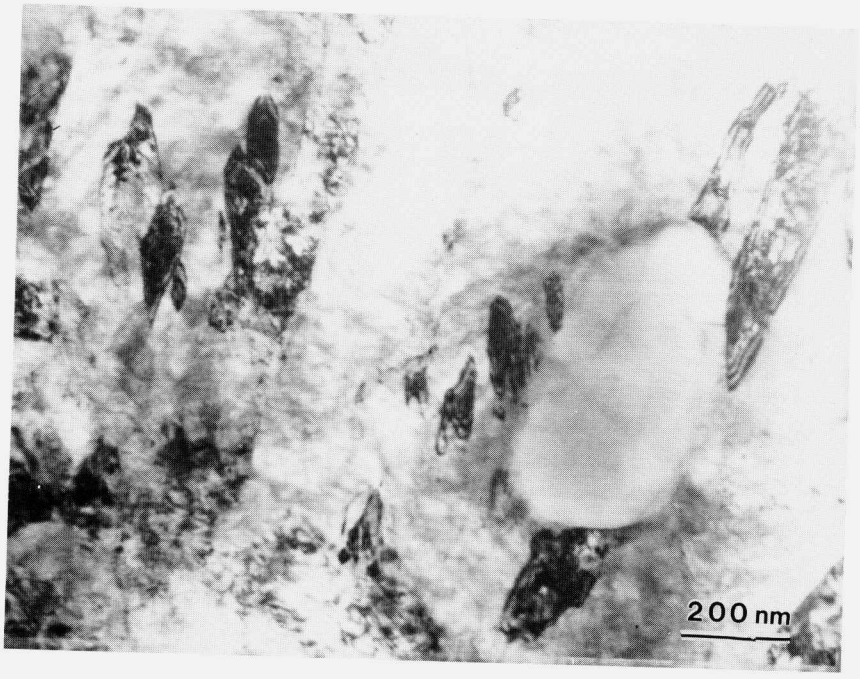

Fig. 13 STEM micrograph indicating austenite particles nucleating on a cementite particle. AF1410 steel, 420°C/5h+510°C/8h treatment.

TABLE 7

STEM MICROANALYSIS OF 420°C/5H + 510°C/8H TREATMENT

	420°C/5h			510°C/8h		
	Mo-rich Cementite	Cr-rich Cementite	Intralath Austenite	Cementite	Interlath Austenite	Isolated Cementite
Size	30-50 nm	30-70 nm	< 100 nm	300 nm	100-200 nm	50 nm
FE	14.91	30.00	69.1	31.3	70.7	55.0
Co	3.93	2.76	10.19	3.2	11.9	7.45
Ni	1.00	2.74	18.80	0.3	14.1	4.6
Cr	15.46	61.00	1.85	60.6	3.3	30.56
Mo	64.56	3.35	0.00	4.40	0.00	2.45

*Compositions are in w/o

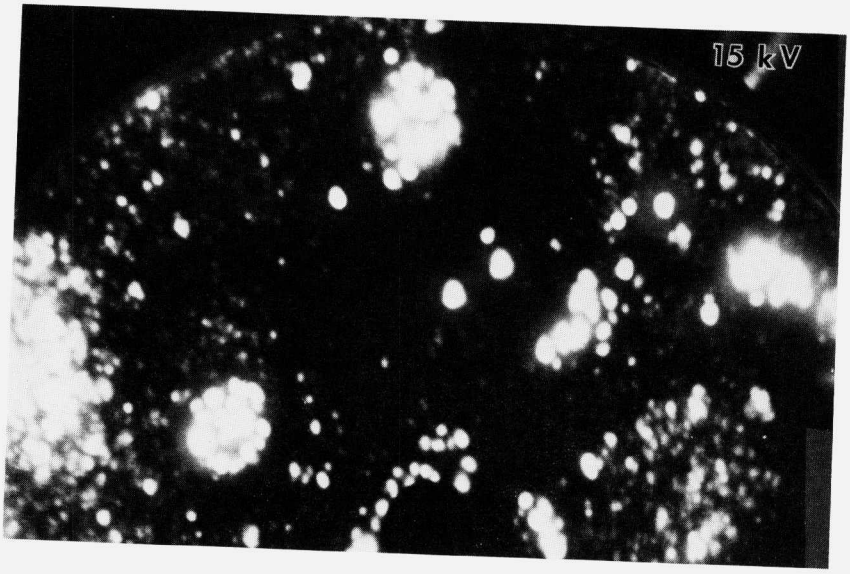

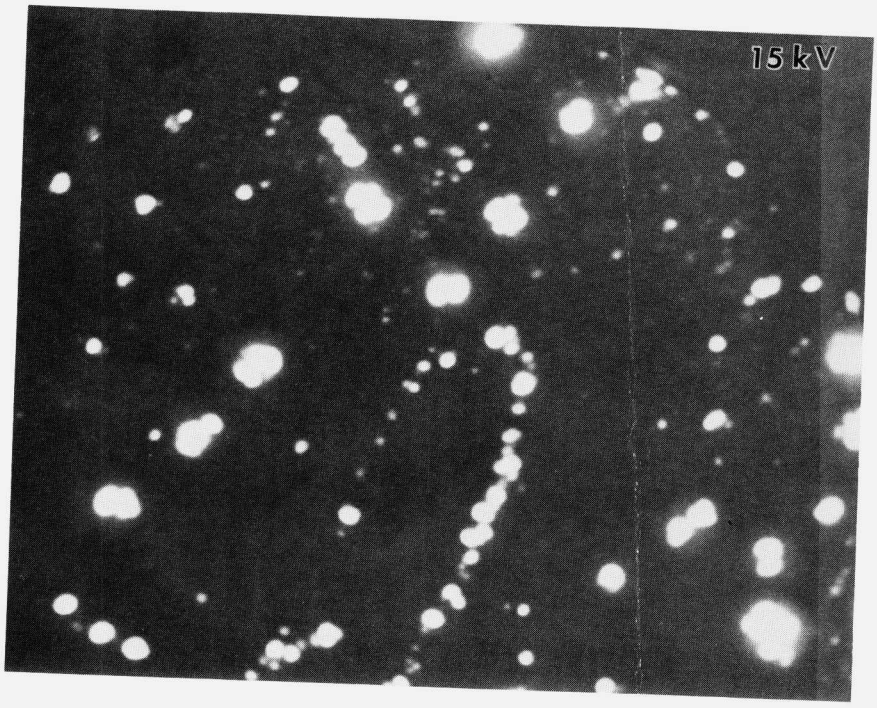

Fig. 14 FIM images of M_2C carbides in AF14120 steel treated at 510°C/8h in (a) and 420°C/5h+510°C/8h in (b). Note the much finer M_2C dispersion in (b).

austenite dispersion is very fine (<100nm) and enriched in Ni. Also present in the microstructure are interlath austenite particles which nucleate on the lath boundaries of the martensitic matrix. These austenite particles are also quite small but with a lower Ni enrichment (14 w/o) than the intralath austenite particles. A shortcoming of this treatment however is the isolated cementite particles which remain undissolved and can act as void-nucleating particles degrading the fracture toughness of the material.

A very important characteristic of the treatment is the resulting hardening (51.5 Rc compared to 46 Rc for the 510°C/8h). This is most likely due to an increased driving force for M_2C carbide precipitation resulting in a much finer dispersion and decreased mean free path of the M_2C carbides. This is indicated in Fig. 14 which shows FIM images of M_2C carbides for the two treatments. The increase in driving force is attributed to a reduction in Cr in solution due to the formation of Cr-rich cementite during the first step of the treatment.

Direct-nucleated austenite (600°C/15 min+510°C/8h)

As mentioned earlier, the purpose of this treatment is both to increase the driving force for austenite precipitation and enhance the diffusivity of Ni. The combination of these effects produces an ultrastable austenitic dispersion. Fig. 15 shows a TEM micrograph indicating the presence of a very fine uniform intralath (10-20nm) austenite dispersion. Fig. 16 shows a BF/DF high magnification image of the intralath austenite particles. An interlath austenite dispersion also forms heterogeneously on the lath boundaries of the martensitic matrix. This dispersion is not as fine as the intralath dispersion.

The composition of the austenite particles was measured by high resolution STEM microanalysis and the results are shown in Table 8. The results for the 510°C/8h as well as the cementite-nucleated austenite treatments are shown for comparison. A substantial NI enrichment of the intralath austenite particles (up to 30 w/O) together with their very small size should make these particles extremely stable.

Fig. 15 TEM micrograph showing ultra-fine intralath austenite dispersion in AF1410 steel formed by the direct-nucleated austenite treatment" (600°C/15min+510°C8h).

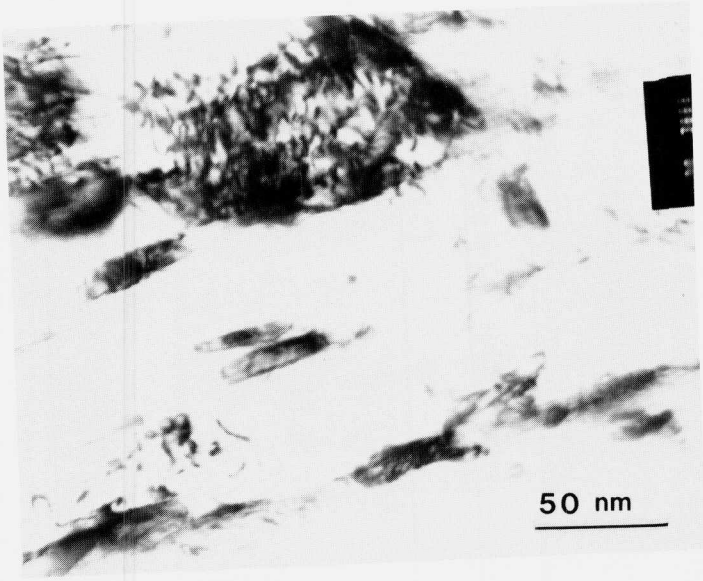

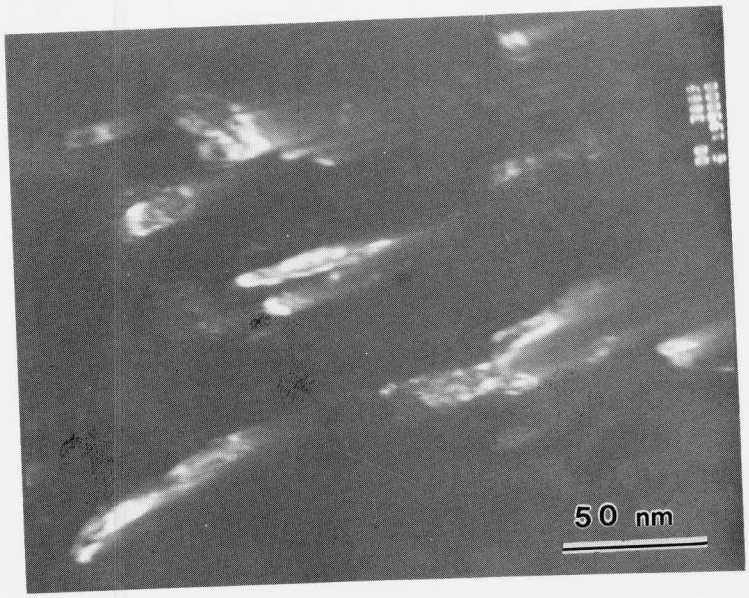

Fig. 16 TEM micrograph showing a Bright/Dark field image of intralath austenite particles in AF-1410 steel. Direct-nucleated austenite treatment (600°C/15min+510°C/8h).

TABLE 8

STEM MICROANALYSIS OF PRECIPITATED AUSTENITE IN AF1410 STEEL

	Single Treatment	Cementite-nucleated		Direct-nucleated	
	510°C/8h	420°C/5h + 510°C/8h		600°C/15min + 510°C/8h	
	Interlath	Interlath	Interlath	Interlath	Interlath
Size(nm)	200	100-200	< 100	100-200	10-20
Ni	14.0	14.1	18.8	16.57	29.1
Co	13.2	11.9	10.19	14.85	10.5
Cr	2.8	3.3	1.85	4.2	4.2
Mo	1.0	0.0	0.0	2.1	1.9
Fe	69.0	70.7	69.1	62.28	54.3

*Compositions are in w/o

FRACTURE TOUGHNESS

Room temperature Charpy-V-notch impact testing was performed as a preliminary assessment of the transformation toughening potential of the precipitate austenite. Testing was performed for all treatments listed in Table 6 and the resulting impact energy is shown vs hardness in Fig. 17.

The direct-nucleated austenite treatment provides considerable toughening (77 ft-lb) relative to the standard treatment (62 ft-lb) with no loss of hardness. We attribute the 15 ft-lb toughness imcrement to dispersed-phase transformation toughening arising from the ultra-stable austenite dispersion.

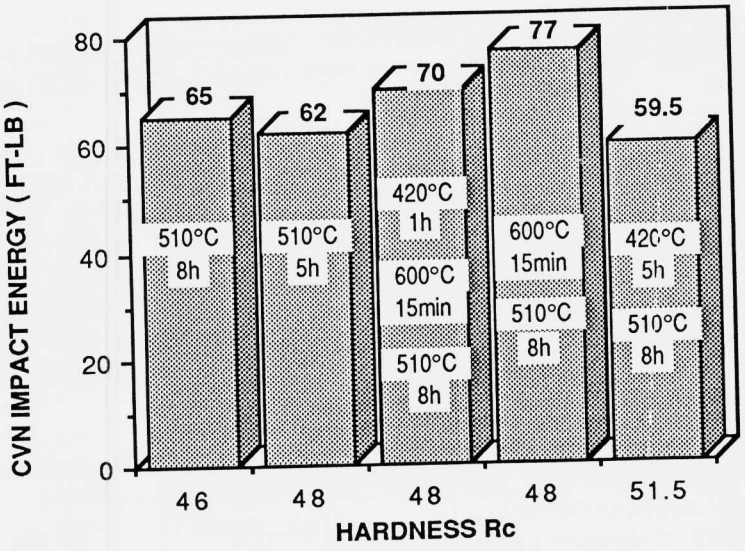

Fig. 17 CVN impact energy as a function of hardness (Rc) for various heat treatments in AF 1410 steel.

The cementite-nucleated austenite treatment results in a decrease in toughness due to the cementite left undissolved.

A similar situation exists with the 420°C/1h+510°C/8h treatment. Although the combined triple treatment gives a higher toughness than the standard treatment, it does not provide the high toughness of the direct-nucleated austenite treatment due to undissolved cementite from the first step.

Table 8 shows that the highest Ni enrichment of the austenite particles is achieved with the direct-nucleated austenite treatment. The average austenite particle size is also the lowest with this treatment. These factors in combination with the absence of undissolved cementite produce substantial toughening effects with technological importance to this class of ultrahigh-strength high-toughness steels.

CONCLUSIONS

Two forms of dispersed austenite, retained austenite in 4340 steel and precipitated austenite in AF1410 steel have been investigated for dispersed-phase transformation plasticity and toughening effects. Major conclusions are:

1. In pure shear deformation, shear instabilities were delayed by the strain-induced transformation of retained austenite.

2. The stability of the retained austenite, characterized by the M_S^{σ} temperature is a strong function of the stress state. It was found that the retained austenite is optimally stable for the pure shear stress state but too unstable for the crack-tip stress state. Thus, despite its flow-stabilizing effects in pure shear, the retained austenite did not produce measurable toughening at room temperature.

3. Size refinement and compositional enrichment of the austenite particles are the most important parameters controlling austenite stability. High stability can be achieved with precipitated austenite which forms on tempering high-Ni secondary-hardening-steels.

4. Multi-step heat treatments were designed for precipitation of stable austenite dispersions. From the treatments investigated, a double treatment termed the direct-nucleated austenite treatment provided substantial toughening (77 ft-lb) with no loss of hardness relative to the standard treatment for AF1410 (62 ft-lb at 48 Rc). This toughening effect is attributed to the precipitation of an ultra-fine and compositionally enriched austenite dispersion. The results indicate that dispersed-phase transformation toughening shows significant technological potential in this class of ultra-strength steels.

REFERENCES

1. G.B. Olson and M. Cohen, Metall. Trans. 7A (1976) 1897.

2. M. Cohen and G.B. Olson, "Martensitic Nucleation and the Role of the Nucleating Defect," in New Aspects of Martensitic Transformations, First JIM International Symposium (JIMIS-1) Kobe, Japan Suppl. Trans. JIM (1796) 93.

3. R.E. Cech and D. Turnbull, Trans. AIME, 206 (1956) 124.

4. J.R. Patel and Morris Cohen, Acta Metall. 1 (1953) 531.

5. G.B. Olson, K. Tsuzaki, and M. Cohen, "Statistical Aspects of Martensitic Nucleation," in Turnbull Symposium: Phase Transformations in Condensed Systems ed. G.S. Cargill, F. Spaepen, and K.N. Tu, MRS, in press.

6. I-W Chen and P. Reyes, J. Am. Ceram. Soc. 69, No. 3 (1986) 181.

7. T. Narutani, G.B.Olson, and M. Cohen, Proc. Int. Conf. Mart. Transf. ICOMAT-82, Leuven, Belgium, J. de Physique 43 (1982) C4-429.

8. T. Narutani, G.B. Olson, and M. Cohen, unpublished research, MIT, Cambridge, MA, 1982.

9. A.G. Evans and R.M. Cannon, Acta Met. 34 (1986) 761.

10. A.G. Evans and A.H. Heuer, J. Am. Cer. Soc. 63 (1980) 241.

11. B. Budianski, J.W. Hutchinson, and J.C. Lambropoulos, Int. J. Solids and Structures 19 (1983) 337.

12. W.W. Gerberich, P.L. Hemmings, and V.F. Zackay, Metall. Trans. 2 (1971) 2243.

13. R.H. Leal, "Transformation Toughening of Metastable Austenitic Steels'" Ph.D. Thesis, MIT, June 1984.

14. C.C. Young, "Sharp-Crack Transformation Toughening in Phospho-Carbide Srengthened Austenitic Stels," Doctoral Thesis Research in Progress, MIT, 1987.

15. J.M. Rigsbee in ICOMAT-79, Cambridge, MA, (1979).

16. B.V.N. Rao, U.S. Patent 4, 544, 422 (1985).

17. M.A. Buonanno, "Austenite Stabilization in Low-Alloy Steels". S.M. Thesis MIT 1987.

18. J.I. Kim, C.K. Syn, and J.W. Morris, Jr. Metall. Trans. 14A (1983) 93.

19. Annual Book of ASTM Standards, E399: Test for Plane-strain Fracture Toughness of Metallic Materials, 1984.

20. G.F. Bolling and R.A. Ritchman, Acta Met. 18 (1970) 673.

21. G.B. Olson and M. Cohen, Met. Trans. 13A (1982) 1907.

22. H. Muir, B.L. Averbach, and Morris Cohen: Trans. ASM 47 (1954) 23.

APPENDIX

TRANSFORMATION MICROYIELDING IN 4340 STEEL

In this appendix we present transformation plasticity effects in the microyielding region associated with retained austenite in 4340 steel.

In homogeneous metastable austenitic steels the characteristic M_S^σ temperature (see Fig. 1) can be conveniently determined from the reversal in the temperature depenbdence in the macroscopic (0.2%) flow stress. However, when the austenite is in the form of a dispersed phase and in moderate amounts, as retained austenite in 4340 steel, a complete reversal in the temperature dependence of the flow stress does not occur making the determination of the M_S^σ rather difficult. This is because of the composite nature of the flow stress.

On the other hand,the elastic limit is a more sensitive parameter that is completely controlled by the transformation in the stress-assisted region. Therefore, a r eversal in the temperature dependence of the elastic limit can be used to determine the M_S^σ temperature dependence retained austenite. At the same time the stress-strain behavior can be studied in the microyielding region and compared with existing models for stress-assisted transformation.

The elastic limit was measured using a technique also used by Muir et al. [1]. It involved a loading-unloading procedure to determine the load producing the first detectable residual strain after unloading. The residual strain was measured with accuracy of 20 $\mu\varepsilon$ using strain gages. The material used was a VAR 4340 steel, austenitized at 1200°C and tempered at 200°C for 1h. The volume fraction of retained austenite was determined by saturation magnetization measurements and was 9%.

The temperature dependence of the elastic limit is shown in Fig. A-1. The 0.2% flow stress and intermediate strain offsets are also shown in the same figure. A complete reversal of the temperature dependence of the elastic limit occurs at 40°C which is the tensile M_S^σ temperature. The 0.2% flow stress does not undergo a reversal.

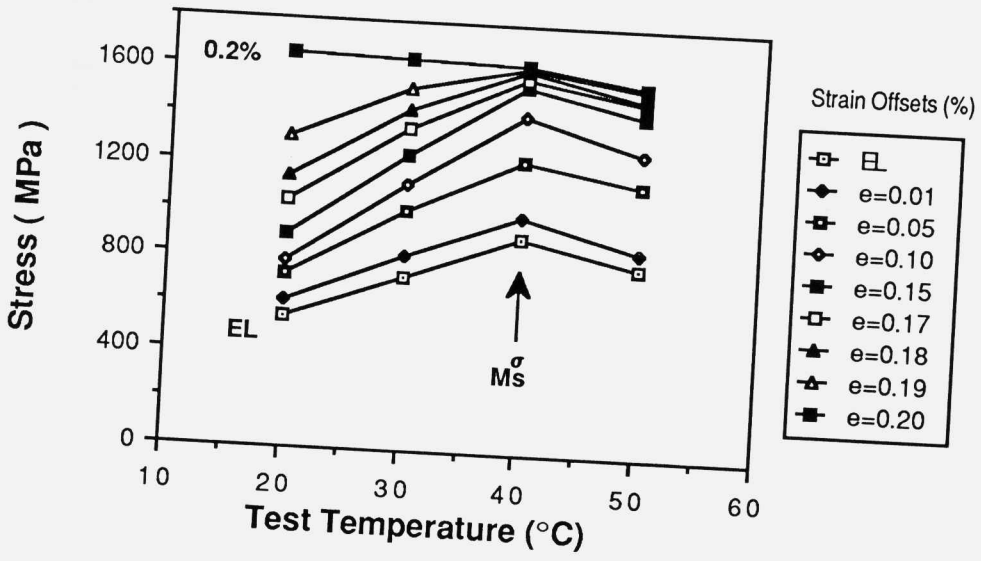

Fig. A-1 Temperature dependence of the elastic limit (EL) and strain offsets between the elastic limit and the 0.2% flow stress in uniaxial tension for 4340 steel containing 9% retained austenite. The arrow indicates the M_s^σ temperature.

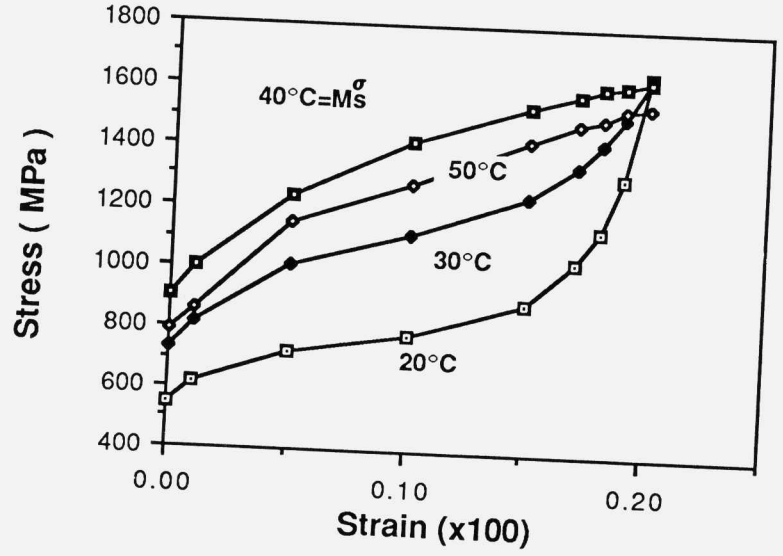

Fig. A-2 Stress-strain curves in the microyielding above and below the tensile M_s^σ temperature; 4340 steel containing 9% retained austenite.

Fig. A-2 shows stress-strain curves obtained in the microyielding region for temperature above and below the M_S^σ temperature. Above the M_S^σ the stress-strain curves have the normal downward curving shape while below the M_S^σ temperature, the stress-strain curves have a sigmoidal shape characteristic of stress-assisted transformation.

Using an existing model describing stress effects on the nucleation-site potency distribution [2] and the assumption of a fully biased distribution of nucleation sites for the transformation [3], the stress-strain curve for 20°C was fitted providing (Fig. 20) Δg_{ch}=-1687J/Mol and $N_V^O V_p$=1.25x10^4 where Δg_{ch} is the chemical driving force, $N_V O$ is the total number of nucleation sites of all potencies, and V_p is the average austenite particle size. The value of the chemical driving force is rather low indicating a considerable carbon enrichment of the austenite. A model considering a fully random distribution of nucleation sites is now under investigation.

Acknowledgments

This research has been supported by NSF-MRL Grant #DMR84-18718 through the MIT Center of Materials Science and Engineering as part of the Steel Research Group program.

Section III: Hydrogen Embrittlement Resistance

Keywords
— solid solution softening hydrogen
BCC deformation

HYDROGEN EMBRITTLEMENT OF HIGH-STRENGTH STEELS

C. J. McMAHON, Jr.
Department of Materials Science and Engineering,
University of Pennsylvania, Philadelphia,
Pennsylvania, 19104.

INTRODUCTION

Hydrogen in solution in the crystal lattice affects both the deformation and the cohesive behavior of iron and its alloys. Therefore, the phenomenon of hydrogen embrittlement of steels is not simple to rationalize or to characterize quantitatively. Fracture may occur by a shear process, in which case the effects of hydrogen on dislocation mobility and the tendency of slip to occur in concentrated bands are the dominant factors. Alternatively, it may occur through a failure of cohesion when a sufficiently high stress is reached, which is what one usually means when referring to embrittlement. Years of observations have established that hydrogen-induced brittle fracture of ferritic steels usually occurs along interfaces, rather than by transcrystalline cleavage. Since interfaces are also commonly contaminated by segregated solutes, often embrittling impurities, it is generally unclear how much of the embrittlement is due to the hydrogen and how much to the impurities. Also unclear is the extent to which hydrogen, itself, segregates preferentially to interfaces and how impurities might influence this.

The present paper is addressed mainly at the brittle-fracture problem and, in particular, at the combined effects of hydrogen and segregated impurities. It includes recent work aimed at separating the hydrogen and impurity contributions by measuring each in mechanical tests. It has been found that inherent physical constraints allow only incomplete success in such an effort, but an understanding of the reasons for this provides useful insights into the significance of such test results.

HYDROGEN EFFECTS IN α-IRON

Deformation Behavior

Both enhancement and diminution of dislocation mobility due to hydrogen charging of iron can be observed under different circumstances, and this area is still a subject of controversy [1]. In particular, experimental observations of the effects of hydrogen charging on bulk specimens, reviewed in [1], and on TEM foils [2,3] have produced conflicting results; it has been suggested [1] that this might be resolvable in terms of the dominance of surface effects in the latter case. For the case of bulk specimens, Kimura and coworkers (see [1]) and Meshii and coworkers [4] have given convincing evidence that hydrogen can occupy, and travel with, dislocation cores and cause the following effects in high-purity iron:

1. Hardening at <200K, presumably due to pinning of kinks on screw dislocations.

2. Softening at 200 to 300K, presumably due to an enhancement of kink-pair formation.

The effects can be quite different in less-pure iron, depending on the amount and type of solute present, so these results cannot be used to predict the behavior of alloy steels. However, they do show that dislocation cores carry hydrogen, which is consistent with observations of sweep-in [5] and sweep-out [6] of hydrogen during plastic deformation of steels.

It is well known that the deformability of metals depends on the mobility of screw dislocations, because of the importance of cross-slip in the process of dislocation multiplication. Computer modeling of dislocation cores has shown [7] that the lack of screw mobility at low temperatures in bcc metals is due to the non-planar nature of the core, in the sense that the <111>-type atomic displacements are not homogeneously distributed around the core, but are concentrated on certain planes, mainly {110} and {112}, which contain the <111> dislocation line. Such a dislocation core is relatively immobile, and the core must become more nearly planar (e.g., due to stress-induced

rearrangements) in order for glide to occur. This non-planarity can also be smeared out by thermal lattice vibrations, which accounts for the decrease in yield stress at higher temperatures and for the brittle-ductile transition with increasing temperature in bcc metals.

Since the actual core configuration, and thus the mobility, of a modeled screw dislocation depends on the shape of the interatomic potential used [7], and since hydrogen can occupy the core, thereby altering the potential, it follows that one should anticipate an effect of hydrogen on screw dislocation mobility.

There have been numerous observations of hydrogen-induced shear instability, or a tendency for slip deformation to concentrate in bands, particularly in high-strength steels [e.g.,8]. This is presumably due, at least partly, to core-entrained hydrogen, but it appears not yet to be possible to give an atomistic rationalization of this from the experiments on simpler materials. We will show later that this provides an alternative fracture mechanism in steels in which impurity-induced embrittlement is sufficiently small.

Cohesion

It has already been noted [9] that, since cohesion is also a function of the interatomic potential, hydrogen cannot affect dislocation mobility without at the same time also changing cohesion. Furthermore, the well-established fact that hydrogen has a very large apparent atomic volume when in solution in the iron lattice, causing an extraordinary lattice expansion (considering that it comprises only a screened proton), leads one to anticipate a reduction in cohesion, since the metal ion cores are displaced from their energy minima. The innumerable observations of hydrogen embrittlement support the idea of a reduction of cohesion but do not prove it. In principle, a similar effect could be caused by the inhibition of dislocation emission from a crack tip, thereby allowing the attainment of higher crack-tip stresses. However, experimental observations do not support this interpretation of the hydrogen effect. For example, Birnbaum and coworkers [10] have shown

by direct TEM observations that crack-tip plasticity is enhanced by the presence of hydrogen, rather than retarded. In addition, recent computer-modeling studies by Daw and Baskes [11] using the embedded-atom method have indicated that hydrogen promotes crack growth in nickel by enhancing the separation of atomic bonds at the crack tip. Fatigue-crack growth measurements in nickel crystals by Vehoff and Klameth [12] have led to the supporting conclusion that the action of hydrogen occurs within 10 nm of the crack tip. Thus, the available evidence is very compelling that hydrogen embrittlement of nickel, and, we believe, iron, occurs through a direct reduction of cohesion of the lattice. This assumption has been the basis of the model which has been developed over a period of years by Troiano and coworkers [13,14], Oriani and coworkers [15,16] and Gerberich and coworkers [17,18], and it is the one adopted in our own work [19-24].

SEGREGATION EFFECTS IN STEELS

Carbon

There is ample evidence in the literature that carbon is essential for intergranular cohesion in iron and ferritic steels. In fact, a routine method of producing intergranular fracture in iron for experimental purposes is to decarburize it in hydrogen gas. There appears to be only one example in the literature [25] of a polycrystalline iron so pure that, when decarburized, it failed by transcrystalline cleavage at a low temperature, and this involved a bamboo-type microstructure, the grain boundaries of which may not have been representative of typical polycrystals. Thus, it may be that the intergranular weakness in carbon-free iron is an impurity effect, even when the impurity level is too small to detect by Auger electron spectroscopy; however, more work is needed to establish this as a certainty. The role of carbon in iron grain boundaries has not yet been modelled by atomistic calculations, but this should be possible with, for example, the embedded-atom method. It is essential to realize that not all segregation effects produce intergranular weakening and that any study of weakening by segregated impurities must be interpreted in terms of the net

effect of the impurities and whatever carbon is present. Usually, the latter is ignored.

Impurity-Induced Embrittlement

With the exception of carbon and boron, it would appear from the literature that any element which segregates to grain boundaries in iron weakens them. This is so because the method commonly used to analyze grain boundaries chemically is Auger electron spectroscopy, which requires that the boundaries be openable by fracture in UHV. Any element that segregates and has a neutral or strengthening effect obviously cannot be studied by this method. Thus, it is not known, for example, whether molybdenum, which we now know segregates to grain boundaries in iron [26], has any direct effect, because the segregation was detected in decarburized samples, and the intergranular weakness could have been merely the effect of decarburization.

The elements which are known to segregate individually and cause embrittlement are indicated in Fig. 1. The Group VI elements are the most potent, increasingly so as the period number increases [27]; these elements are dangerous when present (unscavenged) in amounts well below 100 wt ppm. Phosphorous is also quite surface active and embrittling when present at the several-hundred wt ppm level; antimony and tin are also powerful embrittling elements when present in iron at the level of thousands of wt ppm; however, to produce embrittlement of steel when present at the few-hundred wt ppm level, it appears that the presence of several percent nickel is required. It is generally, but not universally [28], believed that nickel cosegregates with these elements, as rationalized by the regular-solution model of Guttmann [29], and that this is required to enhance their intergranular concentration and, perhaps, to make effect more embrittling [27].

VII_B	IV_A	V_A	VI_B
			O
		P	S
Mn			Se
	Sn	Sb	Te

Fig. 1 Elements known to segregate individually to grain boundaries in iron and cause intergranular embrittlement.

Silicon is still not well understood; in a steel with several percent nickel, segregation of both nickel and silicon were found, along with significant embrittlement [30]. However, silicon (several thousand wt ppm) without nickel does not seem to act on its own [31]. Silicon does enhance the embrittlement of alloy steels by phosphorous; the mechanism of this is not understood, either.

Manganese has long been known to have deleterious effects with regard to temper embrittlement [32], but the mechanism has been difficult to discover. It is now known [33] that manganese segregates on its own in iron and weakens grain boundaries dramatically; thus it is properly classified as an embrittling element. This is rather curious, because it is not only an important alloying element in steels, but it is also a transition metal next to iron in the periodic table, and one would have expected better mutual compatibility. This would be another interesting area for an atomistic study.

HYDROGEN-IMPURITY INTERACTIONS

The focus of the hydrogen-embrittlement studies at the University of Pennsylvania has been on the reasons for the intergranular nature of the embrittlement in high-strength steels. This has grown out of a broad study of intergranular embrittlement in general. One steel which was studied extensively and which illustrates the range of hydrogen effects quite well is the 5% nickel steel, called HY130. This steel was shown to be

highly susceptible to temper embrittlement as commercially formulated [19], but highly resistant when manganese and silicon were omitted from laboratory heats [21]. In the embrittled condition it exhibited intergranular failure in an acidic solution at low stress intensities under a static load, but transgranular fracture at much higher K levels when not aged to allow temper embrittlement before the test [19]. The same kind of result was found in hydrogen gas using both constant load and fixed-displacement specimens in which crack-growth rates were measured as a function of K and the degree of prior temper embrittlement. The threshold value of K for crack growth was found to decrease sharply in the early stages of temper embrittlement, as shown in Fig. 2, and this was accompanied by a transition from transgranular to intergranular cracking. From this it was concluded that the combined effect of hydrogen and impurities was responsible for both the intergranular fracture and the low K_{th} values.

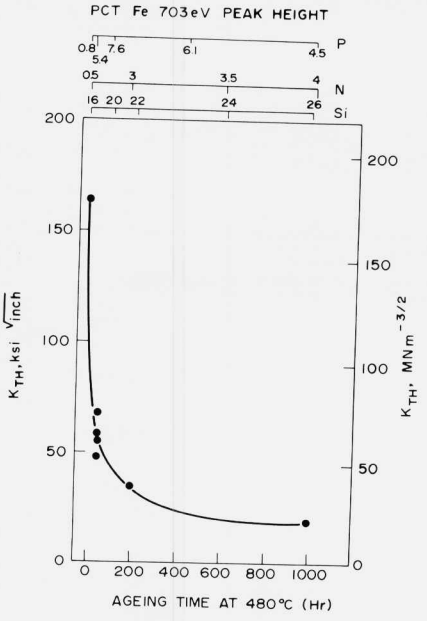

Fig. 2 Reduction of threshold stress intensity for crack extension in hydrogen gas with aging at 480°C in HY 130 steel, due mainly to intergranular segregation of phosphorus [21].

This phenomenon was illuminated further by the work of Takeda [22], who studied two laboratory heats, the compositions and strengths of which are given in Table 1. The absence of temper embrittlement susceptibility in the heat (A), from which manganese and silicon were omitted, is illustrated in Fig. 3a, and the contrast in the effects of aging on the threshold K values in 0.21 MPa hydrogen at room temperature is shown in Fig.3b. It was found that in hydrogen the pre-cracks in heat A began to extend by a Mode II bifurcation at the crack tip, while the crack extension in the other heat (F) after only 50h aging occurred by a partly transgranular mode, and in macroscopic cracking Mode I. This is illustrated schematically in Fig. 4, which also shows the microscopic fracture modes for each case. Thus, it was clear that hydrogen-induced cracking in the absence of impurity effects was essentially innocuous; it occurred only at quite high K values in a way which actually reduced the value of K_I, and by a plasticity-related mechanism which is not a brittle mode of fracture at all.

Table 1 Chemical Compositions of HY 130 Steels (wt pct)

Heat	C	Si	Mn	P	S	Sn
A	0.14	0.03	0.02	0.004	0.005	0.002
F	0.13	0.36	0.90	0.004	0.006	0.001

Heat	Ni	Cr	Mo	V	Al	N
A	4.90	0.51	0.50	0.075	0.300	0.002
F	4.97	0.48	0.50	0.079	0.025	0.002

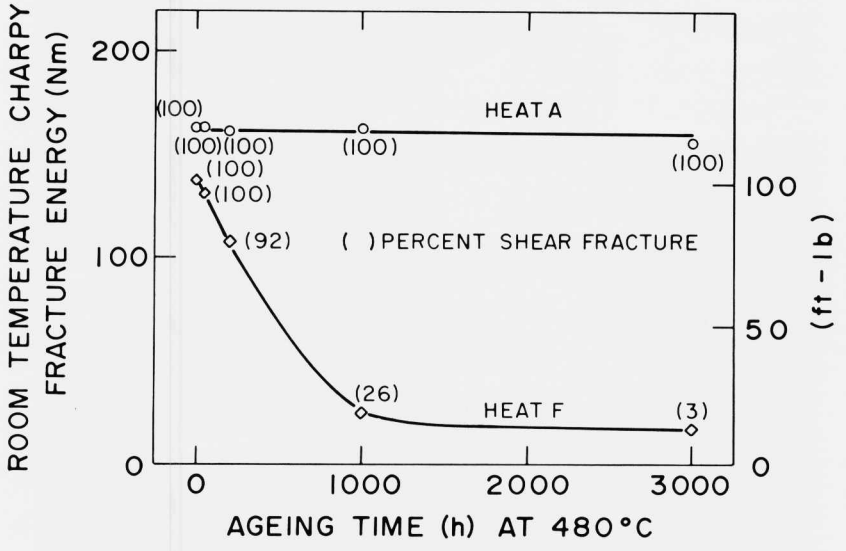

Fig. 3a Comparison of high susceptibility to temper embrittlement of lab heat F of HY 130 (containing manganese and silicon) to the low susceptibility of heat A (no manganese or silicon) [22].

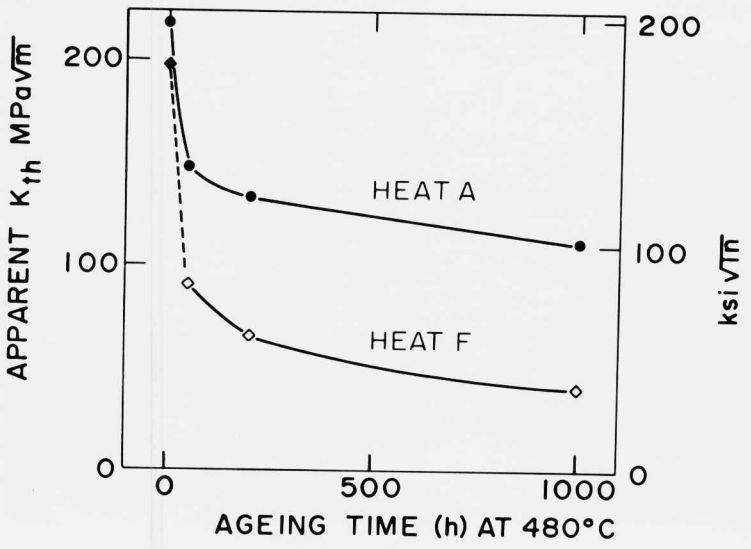

Fig. 3b Corresponding comparison of the effect of aging on the threshold stress intensity for crack extension in hydrogen gas [22].

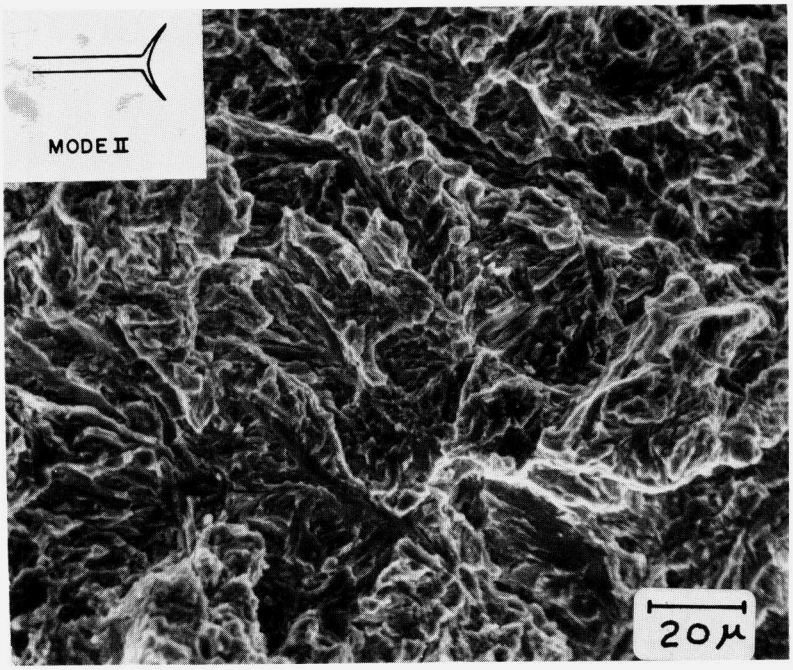

(a)

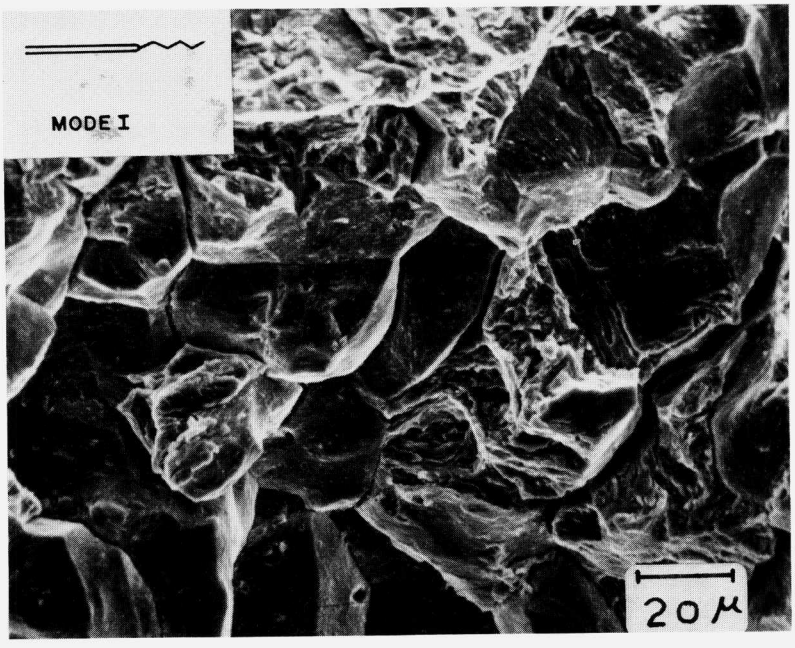

(b)

Fig. 4 Comparison of fracture morphology in initial crack extension in hydrogen gas in (a) heat A and (b) heat F [22].

The decohesion model of hydrogen embrittlement posits that hydrogen reduces the cohesive energy of the crystal lattice as the hydrogen concentration increases and that, because of its large atomic volume, hydrogen diffuses to the region of maximum hydrostatic tension in a stressed specimen. Thus, a notch or crack serves not only to raise the local tensile stress, but also to concentrate the hydrogen and so to lower the stress needed for decohesion. Hence, assuming a linear relationship, the fracture stress in hydrogen should be given by [34]

$$\sigma_{fr} = \sigma_o - \Delta\sigma/\Delta C_H \; k \sqrt{p_H} \exp \frac{PV}{RT} \qquad (1)$$

where σ_o is the fracture stress in the absence of hydrogen, p_H the partial pressure of hydrogen, k Sievert's law coefficient, P the hydrostatic tension, and V the atomic volume of hydrogen in the lattice.

Results on 4340-type steels give qualitative support to this model [20,23]. First, it was found possible, by using high-purity melting stock and eliminating manganese and silicon, to produce a laboratory heat which was extraordinarily resistant to hydrogen-induced cracking [20], and this resistance was found to degrade monotonically as the above elements were added and as the concentrations of phosphorus and sulfur were allowed to increase [23]. The cracking resistance also decreased as the yield strength increased, as illustrated by Fig. 5, which shows results for two steels with different levels of the above elements tested at room temperature in 0.11 MPa hydrogen gas. Since the hydrostatic tension, P, in eq. 1 is given by $(\sigma_{11}+\sigma_{22}+\sigma_{33})/3$ and is approximately $3\sigma_Y$ for this elastic-plastic material, the effect of increasing σ_Y is to increase the hydrogen concentration in the region of the crack tip, as well as to allow the crack-tip stress to approach more closely the cohesive limit. Again in this material, the value of K_{th} was found to fall monotonically with the extent of intergranular fracture, as shown in Fig. 6.

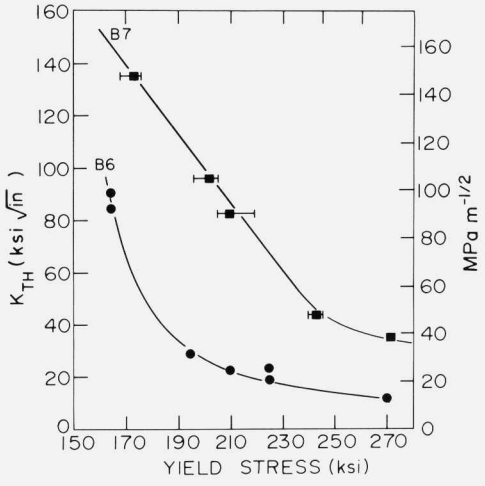

Fig. 5 Decrease in threshold stress intensity for crack extension in hydrogen gas with increasing yield stress in lab heats of 4340-type steel; B6 is with, and B7 without, manganese and silicon [23].

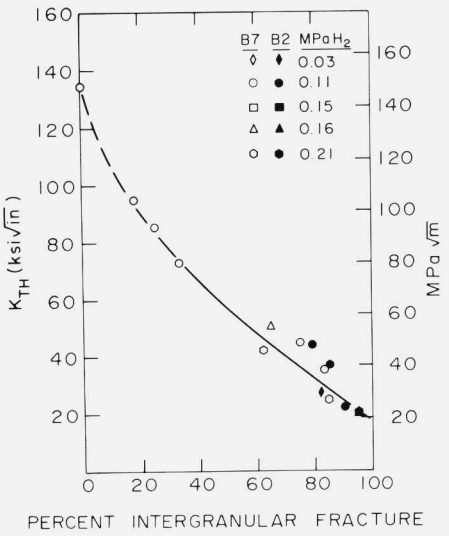

Fig. 6 Correlation of decrease in Kth with increasing intergranular fracture in hydrogen gas for heat B7 and a commercial heat, B2, of 4340 steel [23].

In addition to the intergranular purity and the yield strength, the third variable is, of course, the hydrogen activity, here characterized by the partial pressure. Figure 7 shows how K_{th} varied with the calculated crack-tip hydrogen concentration (cf. eq. 1) in the high- and low-purity steels tested at various yield strengths and hydrogen pressures. The effect of hydrogen is, for the most part, nonlinear, but it is clearly monotonic, and, most importantly, it is qualitatively similar to the effects of the common temper-embrittling impurities. This fact is illustrated by the results shown in Fig. 8 for heats of impurity-doped NiCr steel, in which the variations of both K_{Ic} and K_{th} with intergranular impurity concentration are given. Here is a compelling argument for treating hydrogen as one of a number of cohesion-lowering impurities. (It should be noted that the extent of equilibrium segregation of hydrogen to grain boundaries in iron and steel is unknown quantitatively, but it appears not to be affected by the presence of the above impurities, according to experiments by microautoradiography [39]).

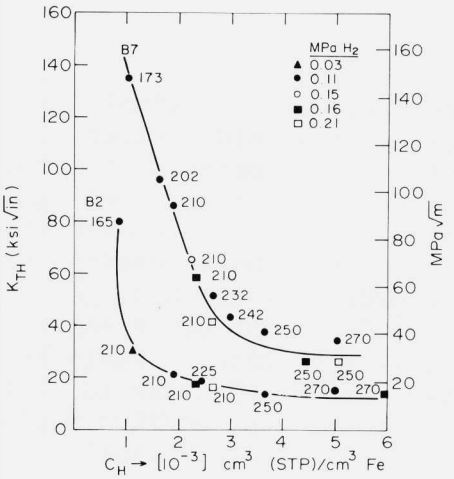

Fig. 7 Correlation of decrease in Kth in heats B2 and B7 with the calculated hydrogen concentration in the crack-tip region in specimens of different yield strength tested in different pressures of hydrogen gas [23].

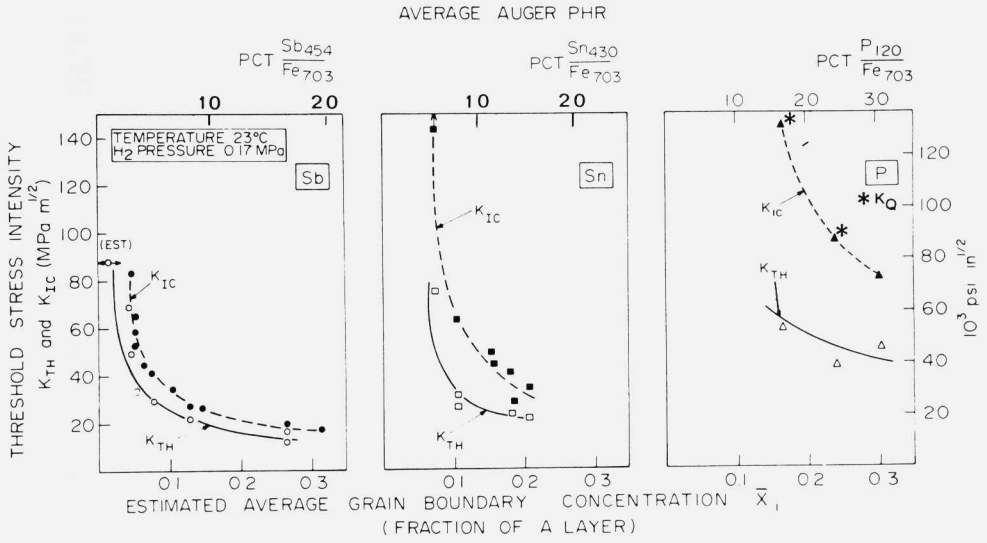

Fig. 8 Effect of increasing the average intergranular concentration of antimony, tin, or phosphorus (through isothermal aging) on K_{Ic} and K_{th} in hydrogen gas in a model NiCr steel [24]. Compare effects of impurities with that of hydrogen in Fig. 7.

The difficulties with the simple model discussed so far are two-fold. First, it ignores the important microscopic details of how hydrogen-induced cracking actually occurs, and, second, the calculated crack-tip hydrogen concentrations are in the ppm range, even with the stress-induced enhancement. In order for the hydrogen to be considered comparable to the other impurities, one would require it to segregate to grain boundaries with an enrichment factor of order 10^5. There is no evidence to support such an enormous surface activity of hydrogen in iron or steel.

These difficulties can be addressed as follows: First, it is now understood that a fatigue pre-crack in a test specimen does not extend in hydrogen in

the manner envisaged for a hypothetical sharp crack, but rather by discontinuous bursts of intergranular cracks which eventually link up and produce a detectible extension of the macroscopic crack [21,24]. These intergranular microcracks form on impurity-weakened grain boundaries in the high-stress (i.e., high-hydrogen) region of the crack tip. The microcracks are known [36] to nucleate at impurity inclusions in the grain boundaries, as shown schematically in Fig. 9. Thus, the hydrogen-induced crack extension is, on the microscopic scale, a discontinuous, dynamic process.

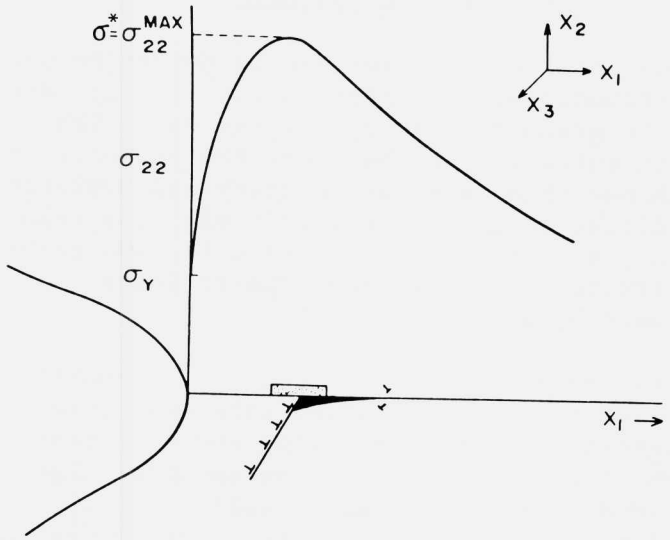

Fig. 9 Schematic illustration of the nucleation of an intergranular microcrack due to blockage of slip at an inclusion in the region of maximum tensile stress ahead of a notch or pre-crack.

The dynamic aspect, when recognized, allowed the formulation of a qualitative rationalization of the large hydrogen effect in materials containing a few atomic ppm hydrogen in the lattice [37]. The key factors are the extraordinarily high mobility of hydrogen in bcc iron and its large atomic volume, which makes it strongly attracted to regions of lattice expansion, such as the core of the tip of a sharp crack. Thus, it is envisioned that the continued extension of a microcrack nucleus (Fig. 9)

can be enhanced by hydrogen gathered up from the surrounding lattice as the tip advances. If this hydrogen is carried along in increasing amounts by the microcrack tip, the cohesive energy would continuously decrease, thereby enabling the formation of full-blown microcracks of the grain size or larger in cases where the applied stress or impurity concentration would be otherwise too small. A test of this idea would require a molecular-dynamic simulation using believable interatomic potentials, which does not yet appear feasible.

RECENT FRACTURE STUDIES

The goal of these studies was to determine how hydrogen interacts with segregated impurities: How does the intergranular fracture stress vary with impurity concentration and how does the presence of hydrogen change this; are the impurity and hydrogen effects additive or not? The result was less than a clear answer, but the attempt appears to have probed the outer limits of what we can hope to learn quantitatively by mechanical tests.

In this study, begun by Kameda [24], impurity-doped heats of a model NiCr steel were embrittled to varying degrees by isothermal aging and then tested in the form of notched bars in slow bending. The notch provided a stress elevation sufficient to produce brittle fracture at room temperature over a wide range of impurity concentrations, but this stress was calculable by the finite-element method, and it varied slowly over distances of the order of the grain size, in contrast to the high, constricted, sharply varying stress field ahead of a fatigue pre-crack. Measurement of the distribution of impurity concentrations on the grain boundaries by scanning Auger microprobe analysis, together with a statistical analysis, allowed an estimate of the most probable maximum impurity concentration in the highly stressed region ahead of the notch. The maximum tensile stress at fracture was correlated with the maximum impurity concentration, under the assumption that these two factors controlled microcrack nucleation, which was found to lead directly to fracture of the specimen.

A comparison of the variation of this fracture stress, σ^*, with the concentrations of antimony, tin, and phosphorous is given in Fig. 10. At first, this was taken to represent the grain boundary strength as a function of composition. Later [38] it was realized that, since the microcracks were

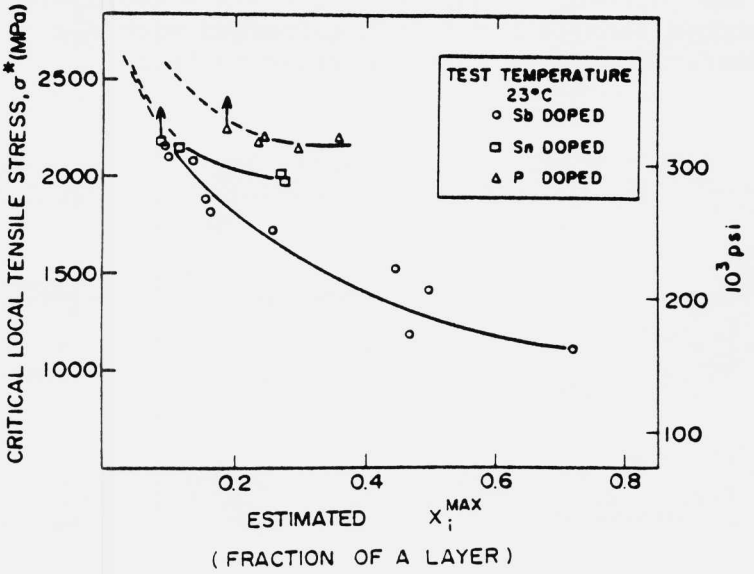

Fig. 10 Correlation of maximum stress ahead of the notch at fracture (coinciding with microcrack nucleation) with the maximum intergranular impurity concentration in the high-stress region [27].

nucleated at inclusions and since the inclusions varied in size and number among the grain boundaries, one would have to take account of this second, independent distribution in the analysis.

Kameda [24] then showed that, when the specimens were loaded in 1.7 atm hydrogen, the fracture stress was reduced to a value designated σ_H^* and that microcracks formed in hydrogen at a still lower stress, σ_{th}, as shown in Fig. 11. (The first microcracks were found to form one or two grain diameters ahead of the notch tip, as one would expect from the decohesion model.) A puzzling feature of these results for the case of the antimony-doped steel was the convergence of the σ_{th} and σ^* values at high levels of segregated antimony.

A succeeding study by Morgan [38] was aimed at understanding this convergence, since it appeared to show that hydrogen exerted no effect at high levels of a potent segregated impurity. Morgan reproduced Kameda's results almost exactly and then showed that the curve of σ_{th} could be lowered by reducing the yield stress of the steel. This counter-intuitive result was followed by another: The σ_{th} measured in an unnotched tensile bar (which coincided with σ_H^*) was considerably lower than σ_{th} measured in a

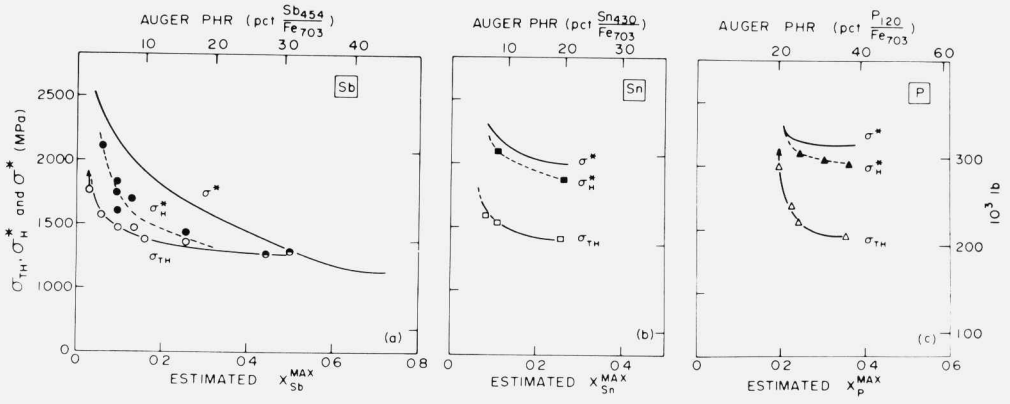

Fig. 11 Effect of hydrogen in lowering the micro-crack nucleation stress σ_{th} and fracture stress ∂H in similar specimens [24].

notched bar of the same yield strength and impurity distribution. The reason for the convergence shown for the antimony-doped steel in Fig. 11 was then apparent: As in any case of brittle crack formation in iron or steel, plastic yielding is a pre-requisite to cracking, since it provides the necessary initial stress concentration (e.g., at the tip of a slip band blocked at an inclusion). Once σ_{th} falls to a value at which the yielded region is of the order of one grain in size, it cannot fall further, no matter how much the impurity concentration increases. This is because the crack-nucleating process of slip blockage at a reasonably-large inclusion (e.g., an oxide or sulfide) lying on a well-embrittled grain boundary becomes unlikely. Thus, the yield stress provides a lower cut-off below which one cannot measure a fracture or cracking stress. This is exactly analogous to the

effect of increasing the grain size in the low-temperature brittle fracture of iron, demonstrated in the classical work of Low [40], where the fracture stress falls below the yield stress at coarse grain sizes and therefore cannot be measured. In the present case one can observe hydrogen-induced cracking at lower stresses only by lowering the yield stress of the notched bar or by using a specimen in which the constraint of the notch is absent.

The results in Fig. 11 can, therefore, be interpreted as showing that the impurity and hydrogen effects are essentially additive. They also show that there is only a restricted range of stress within which one is able to observe the hydrogen and impurity effects. The lower limit of the range is defined by the necessity for yielding over a region sufficiently large for microcrack nucleation to occur. The upper limit is imposed by the necessity to reach a certain tensile stress in order to extend the microcrack, once nucleated. Thus, when the impurity concentration is low, the stress needed to produce a brittle crack is too high to be reached before the onset of general yielding, which prevents any further significant elevation of stress.

These results, when taken together, reveal not only the nature of the hydrogen-impurity interaction, but also the limitations of mechanical tests in studying these phenomena.

ACKNOWLEDGEMENTS

The preparation of this report was supported by the National Science Foundation under grant no. DMR 86-12168; the NSF also supported the work of Bandyophadhyay, Kameda, Morgan, and Takeda under previous grants.

REFERENCES

1. H. Kimura and H. Matsui, Scripta Metall., 1987, Vol. 21, p. 319.

2. T. Tabata and H. K. Birnbaum, Scripta Metall., 1983, Vol. 17, p. 947.

3. T. Tabata, Bul. Japan Inst. Metals, 1985, Vol. 24, p. 485.

4. J. Nagakawa, K. S. Shin, C. G. Park, and M. Meshii, Supl. to Trans. Japan Inst. Metals, 1980, Vol. 21, p. 549.

5. J. K. Tien, A. W. Thompson, I. M. Bernstein, and R. J. Richards, Metall. Trans. A, 1976, Vol. 7A, p. 821.

6. J. A. Donovan, Metall. Trans A, 1976, Vol. 7A, p. 145.

7. V. Vitek, Crystal Lattice Defects, 1974, Vol. 5, p. 1.

8. T. D. Lee, T. Goldenberg, and J. P. Hirth, Metall. Trans. A, 1979, Vol. 10A, p. 199.

9. C. J. McMahon, Jr., Hydrogen Effects in Metals, 1981, TMS-AIME, eds. I. M. Bernstein and A. W. Thompson, p. 219.

10. T. Tabata and H. K. Birnbaum, Scripta Metall., 1984, Vol. 18, p. 231.

11. M. S. Daw and M. I. Baskes, NATO Advanced Workshop on Physics and Chemistry of Fracture, Bad Reichenhall, West Germany, 1986.

12. H. Vehoff and H. K. Klameth, Acta Metall., 1985, Vol. 33, p. 955.

13. H. H. Johnson, J. F. Morlet, and A. R. Troiano, Trans. TMS-AIME, 1958, Vol. 260, p. 528.

14. A. R. Troiano, Trans, ASM, 1960, Vol. 52, p. 54.

15. R. A. Oriani, Ber-Bunsen-Geselsch. Phys. Chem. 1972, Vol. 76, p. 848.

16. R. A. Oriani and P. H. Josephic, Acta Metall., 1974, Vol. 22, p. 1065.

17. W. W. Gerberich and Y. T. Chen, Metall. Trans. A, 1975, Vol. 6A, p. 271.

18. J. F. Lesser and W. W. Gerberich, Metall. Trans. A, 1976, Vol. 7A, p. 953.

19. K. Yoshino and C. J. McMahon, Jr., Metall. Trans., 1974, Vol. 5, p. 363.

20. S. K. Banerji, C. J. McMahon, Jr., and H. C. Feng, Metall. Trans. A, 1978, Vol. 9A, p. 237.

21. C. L. Briant, H. C. Feng, and C. J. McMahon, Jr., Metall. Trans. A, 1978, Vol. 9A, p. 625.

22. Y. Takeda and C. J. McMahon, Jr., Metall. Trans. A, 1981, Vol. 12A, p. 1255.

23. N. Bandyophadhyay, Jun Kameda, and C. J. McMahon, Jr., Metall. Trans. A, 1983, Vol. 14A, p. 881.

24. Jun Kameda and C. J. McMahon, Jr., Metall. Trans A, 1983, Vol. 14A, p. 903.

25. H. Matsui, S. Morija, S. Tahaki and H. Kimura, Trans. Japan Institute of Metals 1978, Vol. 19, p. 163.

26. M. Menyhard and C. J. McMahon, Jr., to be published.

27. Jun Kameda and C. J. McMahon, Jr., Metall. Trans. A, 1981, Vol. 12A, p. 31.

28. C. L. Briant and A. M. Ritter, Acta Metall., 1984, Vol. 32, p. 2031.

29. M. Guttmann, Surf. Sci., 1975, Vol. 53, p. 213.

30. S. Takayama, T. Ogura, S. C. Fu, and C. J. McMahon, Jr., Metall. Trans. A, 1980, Vol. 11A, p. 1513.

31. J. C. Murza and C. J. McMahon, Jr., ASME J. Eng. Matls. Tech., 1980, Vol 102, p. 369.

32. W. Steven and K. Balajiva, J. Iron Steel Inst., 1959, Vol. 193, p. 141.

33. Weng Yu-Qing and C. J. McMahon, Jr., in Grain Boundary Structure and Related Phenomena, suppl. to Trans. Japan Inst. Metals, 1986, Vol. 27, p. 579.

34. C. M. Li, R. A. Oriani, and L. W. Darken, Z. Phys. Chem., 1966, Vol. 49, p. 271.

36. Jun Kameda and C. J. McMahon, Jr., Metall. Trans. A, 1980, Vol. 11A, p. 91.

37. Jun Kameda and M. L. Jokl, Scripta Metall., 1982, Vol. 16, p. 325.

38. M. J. Morgan, Ph.D. Thesis, Univ. of Pennsylvania, 1987.

39. J. Aucoutourier, Univ. Paris Sud, Orsay, 1985, private communication.

40. J.R. Low, Jr. in Relation of Properties to Microstructure, ASM, Cleveland, 1954, p. 163.

THERMODYNAMIC AND MECHANICAL MODELS OF INTERFACIAL EMBRITTLEMENT

PETER M. ANDERSON,[1], JIAN-SHENG WANG,[2]
and JAMES R. RICE[2*]

[1] Department of Materials Engineering, Ohio State University, Columbus, Ohio, 43210
[2] Division of Applied Sciences, Harvard University, Cambridge, MA 02138

ABSTRACT

We present thermodynamic and mechanical models of interfacial embrittlement. These include consideration of the dependence of interfacial decohesion on segregants and their mobility, and analysis of the competition between cleavage decohesion and dislocation blunting at an interfacial crack tip. Results are illustrated by applications to various segregants (H, C, P, Sn, Sb, S) in Fe with estimates of their effects on the work of interfacial decohesion, $2\gamma_{int}$. The theory on emission versus cleavage is applied to the model system of [110] symmetric tilt Cu bicrystals with segregated Bi. Two of those and other Cu bicrystals were grown, heat treated, and tested mechanically. The [110] tilt bicrystals show qualitative compatibility with the theory, which could not be closely tested. As a group, the bicrystals showed highly variable resistance to interfacial cracking and a range of fracture morphologies.

INTRODUCTION

We review some thermodynamics and mechanics concepts used to study intergranular decohesion and the embrittlement or toughening caused by interface impurity segregants. The discussion first focuses on elastic-brittle fracture, and considers the Griffith condition for a cracking interface on which an impurity segregant lies. Using a thermodynamic framework that includes both adsorption and decohesion, the general features which distinguish cohesion enhancers from reducers are noted. Quantitative estimates are made of the deleteri-

ous effects of P, Sn, Sb, S and H on Fe grain boundaries and of why C seems to moderate the embrittling effects of such segregants.

Crack tip dislocation interactions may relax the high crack tip stress field and/or blunt a sharp crack tip, and therefore determine whether an atomically-brittle decohesion mode will occur. This issue is addressed in the context of a critical set of elastic stress intensity factors, K_M^{disl} ($M = 1,2,3$ denotes the loading mode), for emission of a single dislocation from a crack tip. Whether such emission or, instead, atomic decohesion occurs first as a stationary crack tip is loaded is regarded as fundamental to whether a cracked crystal, or interface, is intrinsically cleavable. Some qualifications to exercising this criterion are that the effect of external dislocations not nucleated from the crack tip and the overall viscoplastic dynamics of crack propagation are not accounted for in the present model.

The effect of a driving force for impurity segregation to the dislocation core or blunted crack tip will generally be to reduce the critical crack tip loading for dislocation emission from the impurity-free value. A successful embrittler must, however, reduce the critical crack tip load for cleavage below both that for crack tip dislocation emission and that for extensive nucleation and motion of external, non-crack-tip dislocations.

Finally, the work of atomically-brittle decohesion is evaluated for several Cu-Bi [110] symmetrical tilt interfaces, and is compared to corresponding estimates for dislocation emission from an interface crack. The work of decohesion is estimated to vary by up to 40% among the boundaries considered, and to reduce by up to 35% from the values for pure Cu. The corresponding value of energy release rate G for dislocation emission is expected to be little affected by impurities with low mobility such as Bi, at least assuming that residual elastic misfit stresses are small, although it is predicted to be highly dependent on the mode of crack loading and crack orientation.

Mode 1 tests of interfacial cracks in Cu-Bi bicrystals lead to ductile and brittle interface failure that is qualitatively consistent with theoretical predictions. Results include a dependence of brittleness on crack growth direction, as predicted theoretically, although it seems unlikely that the theoretical predictions could be correct in detail in describing interfacial fracture in this system.

INTERFACIAL SEGREGATION AND WORK OF DECOHESION

In this section, we first summarize recent discussions of interfacial segregation and cohesion by Rice (1) and Rice and Wang (2). Consider a loaded crack lying along an interface as shown in Fig. 1a. The criterion for crack growth in the absence of plasticity would be given by the Griffith condition,

$$G = 2\gamma_{\text{int}} \tag{1}$$

where G is the energy consumed per unit area of crack advance, and $2\gamma_{\text{int}}$ is the reversible work of separating the interface through displacement δ, against atomic cohesive forces as shown in Fig. 1a. If the tensile stress σ across the interface is regarded as a function of the crack profile displacement δ as shown in Fig. 1b, then

$$G = \int_0^{\delta'} \sigma(\delta)\, d\delta = 2\gamma_{\text{int}} \tag{2}$$

which one may recognize as the area under the σ versus δ curve. There may be other work modes involving in-plane shearing displacements which are not considered here. Rice and Wang (2) discuss various theoretical concepts for interfacial decohesion in non-ideally-brittle systems. They conclude that of those properties susceptible to alteration by atomic segregation of impurities to interfaces, the alterations of $2\gamma_{\text{int}}$ has an important but probably not exclusive role in determining embrittlement.

To evaluate the above integral relation for an interface containing an impurity (3,4), consider the interface as a thermodynamic system described in terms of Gibbsian excess quantities. For example, in a body loaded by remote uniform tension σ normal to the interface, define δ as the excess of total displacement of a point A in one phase relative to a point B in the other, over that accountable by homogeneous straining of the two phases in which points A and B reside. Then $\sigma d\delta$ is the excess of work over that accountable as work in straining the adjoining phases, and this work expression will obey the laws of thermodynamics in terms of analogously defined excess internal energy, heat adsorption, free energy ($\bar{f}$ per unit area of undeformed interface), surface energy ($\bar{\gamma}$ per unit area of undeformed interface), entropy ($\bar{s}$), *etc.*

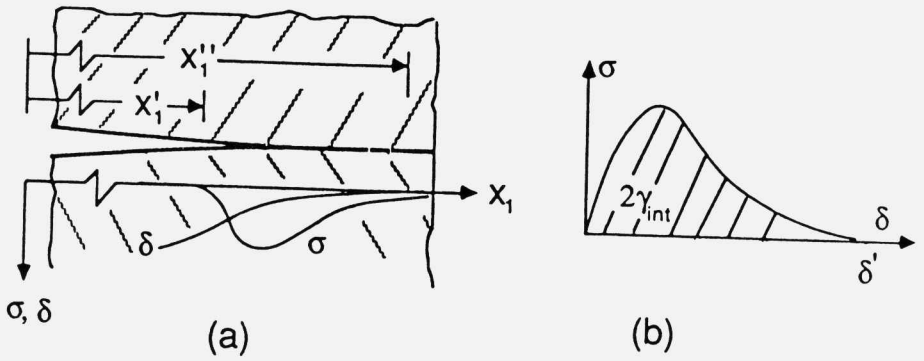

FIG. 1. (a). Loaded interfacial crack showing a schematic distribution of tensile stress σ and opening displacement δ at the crack tip. **(b).** Representation of the work of separation in the σ-δ plane.

A Constitutive Approximation for Local Interface Equlibrium

In fracture as affected by solute segregation, one is often concerned with interfaces that are out of composition equilibrium with the bulk, both before and after separation. For simplicity, a single segregant is considered which is present only at extremely small concentrations in the adjoining bulk phases so that the concentration Γ per unit reference area of interface is unambiguously defined. In order to deal with nonequilibrium separation, the constitutive approximation $\sigma = \sigma(\delta, \Gamma, T)$ and $\bar{f} = \bar{f}(\delta, \Gamma, T)$ is adopted. Within this approximation, the state functions, *e.g.*, $\bar{f}(\infty, \Gamma, T)$, are regarded as the same function of Γ irrespective of whether it refers to the energy of a pair of surfaces at temperature T that have been freshly created by a fracture and contain total solute Γ or to a pair of free surfaces which have reached a state of composition and reconstruction equilibrium at temperature T and solute content Γ. The model described by this approximation is thus one for which all states of the interface are at local equilibrium, but are not necessarily at equilibrium with the bulk phases.

By standard thermodynamic formalism, but assuming that the interface is constrained against composition equilibrium with the ad-

joining bulk phases,

$$d\bar{f} = \sigma d\delta - \bar{s}dT + \mu d\Gamma$$
$$d\bar{\gamma} = d(\bar{f} - \mu\Gamma) = \sigma d\delta - \bar{s}dT - \Gamma d\mu \tag{3}$$

where μ is defined by $\partial\bar{f}(\delta,\Gamma,T)/\partial\Gamma$ and is the equilibrating chemical potential of the solute as it is present locally along the interface.

Limiting Thermodynamic Cases of Separation

Within this framework, we may identify two limiting cases of isothermal separation (3,4). The classically considered one is separation at composition equilibrium with bulk phases, *i.e.*, with $\mu =$ constant, for which the work $\int \sigma d\delta$ of interfacial separation is

$$\begin{aligned}(2\gamma_{\text{int}})_{\mu=\text{const.}} &= \bar{\gamma}(\infty,\mu,T) - \bar{\gamma}(\delta_b,\mu,T) \\ &= (2\gamma_{\text{int}})_0 - \int_{-\infty}^{\mu} [2\Gamma_s(\mu') - \Gamma_b(\mu')]d\mu' \ ,\end{aligned} \tag{4}$$

where $\delta = \delta_b(\mu,T)$ on the unstressed boundary. Here $\Gamma = 2\Gamma_s(\mu)$ and $\Gamma = \Gamma_b(\mu)$ describe the relations between Γ and μ at fixed temperature T for the two free surfaces ($\delta = \infty$) created by separation (*i.e.*, $\Gamma_s(\mu)$ is the composition on a single one of the pair) and for the unstressed boundary or interface ($\delta = \delta_b$). Similarly, for separation at constant composition Γ, the work $\int \sigma d\delta$ is

$$\begin{aligned}(2\gamma_{\text{int}})_{\Gamma=\text{const.}} &= \bar{f}(\infty,\Gamma,T) - \bar{f}(\delta_b,\Gamma,T) \\ &= (2\gamma_{\text{int}})_0 - \int_0^{\Gamma} [\mu_b(\Gamma') - \mu_s(\Gamma'/2)]d\Gamma' \ .\end{aligned} \tag{5}$$

Here, $\delta = \delta_b(\Gamma,T)$ on the unstressed boundary, and $\mu = \mu_s(\Gamma/2)$ and $\mu = \mu_b(\Gamma)$ describe the two relations between Γ and μ mentioned above. Often $(2\gamma_{\text{int}})_0$, which refers to the impurity free interface ($\Gamma = 0$), is written as $2\gamma_s - \gamma_b$.

Detailed forms for the two limiting works of separation defined by eqs. (4) and (5) have been given in the literature (5,6) based on the Langmuir-McLean form,

$$\begin{aligned}\mu_b(\Gamma_b) &= \Delta h_b - T\Delta s_b^{\circ} + RT\ln[\Gamma_b/(\Gamma_b^{\circ} - \Gamma_b)] \ , \\ \mu_s(\Gamma_s) &= \Delta h_s - T\Delta s_s^{\circ} + RT\ln[\Gamma_s/(\Gamma_s^{\circ} - \Gamma_s)] \ .\end{aligned} \tag{6}$$

Here $\Delta s^{\circ}_{b/s}$ is a vibrational entropy term and $\Gamma^{\circ}_{b/s}$ denote values of $\Gamma_{b/s}$ at full coverage. Also, $\Delta g_{b/s} = \Delta h_{b/s} - T\Delta s^{\circ}_{b/s}$ is the free energy of segregation relative to the bulk, where $\mu = RT \ln[x/(1-x)] \approx RT \ln x$ in a bulk phase with fraction x of available sites occupied by the solute.

For isothermal separation at constant composition Γ (below Γ°_b), the entropy terms are generally found to make a small contribution at room temperature (2), and

$$\begin{aligned}(2\gamma_{\text{int}})_{\Gamma=\text{const.}} &\approx (2\gamma_{\text{int}})_0 - (\Delta g_b - \Delta g_s)\Gamma \\ &\approx (2\gamma_{\text{int}})_0 - (\Delta h_b - \Delta h_s)\Gamma \end{aligned} \tag{7}$$

For isothermal separation at constant chemical potential μ, which equilibrates initial coverage Γ on the unstressed boundary,

$$\begin{aligned}(2\gamma_{\text{int}})_{\mu=\text{const.}} &= (2\gamma_{\text{int}})_0 \\ &\quad - RT\left[2\Gamma^{\circ}_s \ln\left(\frac{\Gamma^{\circ}_b + (\lambda-1)\Gamma}{\Gamma^{\circ}_b - \Gamma}\right) - \Gamma^{\circ}_b \ln\left(\frac{\Gamma^{\circ}_b}{\Gamma^{\circ}_b - \Gamma}\right)\right]\end{aligned} \tag{8}$$

where

$$\lambda = \exp[(\Delta g_b - \Delta g_s)/RT] \ .$$

Separation at constant μ is always the more embrittling of the two cases discussed, for it may be shown (3,4) that so long as $d\Gamma/d\mu > 0$ on the pair of free surfaces, $2\gamma_{\text{int}}$ for slow separation at constant μ is less than that for fast separation at constant Γ.

It can also be shown (1) that the work of separation at constant Γ along a reversible path is a lower bound to the work of separation along actual (irreversible) paths which have the same initial and final states of the interface and pair of free surfaces. Thus, within the limitation that $\bar{f} = \bar{f}(\delta, \Gamma, T)$ and provides an adequate description of the interface and resulting crack surfaces,

$$W \geq W_{\text{rev}}[= \bar{f}(\infty, \Gamma, T) - \bar{f}(\delta_b, \Gamma, T) \quad \text{at const. } \Gamma] \tag{9}$$

where the right side coincides with equations (5) and (7).

Equations (7) and (8) are convenient forms which clearly show that the difference in segregation free energies, $(\Delta g_b - \Delta g_s)$, and the excess, Γ, residing on the interface are important in determining

the embrittling potential of a solute. Estimates of adsorption free energies, Δg, or enthalpies, Δh, are generally difficult to come by. Wynblatt and Ku (7,8) provide a model to estimate surface adsorption energies which depends primarily on the heats of sublimation of the solute and solvent as well as the heat of mixing. The model gives a reasonable estimate of the surface segregation energy for Cu-Bi (9). In principle, $\Delta g = \Delta h - T\Delta s^\circ$ can be determined from high temperature adsorption isotherms for which the surfaces or boundary are at composition equilibrium with the bulk, and in which AES (most frequently) or RBS techniques are used to estimate Γ_b or Γ_s. For such conditions, the chemical potential of the grain boundary/surface, given by eq. (6), is equated to that for the bulk. The resulting expression,

$$\Gamma/(\Gamma^\circ - \Gamma) = x \exp[\Delta g(T)/RT] \tag{10}$$

may be fitted to high T results to define Δg, and Δh and Δs° are determined separately using $\Delta s^\circ = -d(\Delta g)/dT$. Typically, one assumes that values of Δh and Δs° determined above are independent of T down to room temperature conditions.

Rice and Wang (2) have recently surveyed the literature on such determinations of Δg_b and Δg_s for segregants in Fe. There are considerable uncertainties and some inconsistencies in the data. Also, there are indications that $-\Delta g_s$ for low index crystal surfaces may be much larger than for general polycrystalline surface created by intergranular fracture, at least for P and Sn. Unfortunately, for C only the $-\Delta g_s$ for the low index (100) surface is known, and this might seriously overestimate the polycrystalline value. Their results for C, Sn, P, Sb and S in Fe all reduced to $T = 300$ K, are given as broad, approximate ranges in Table 1; the reader is referred to their paper for further discussion of the data and references. By using results summarized by Hirth (10) for H in Fe, including his estimate for Δh_b in terms the segregation enthalpy of H to a dislocation core, and results of Grabke (11), we have added estimates for H in Fe to the table.

We now use the results summarized in Table 1 to evaluate our formulae for $2\gamma_{\text{int}}$, in particular, for the reduction of $2\gamma_{\text{int}}$ from $(2\gamma_{\text{int}})_0$ due to segregation. The reductions are indicated in particular cases in Tables 2 and 3. To interpret the significance of these

TABLE 1

Free Energies of Segregation, in kJ/mol, for Grain Boundaries and (Polycrystalline) Free Surfaces of Fe, at $T = 300$ K. (Data for C, P, S, Sn and Sb from review by Rice and Wang; data for H from review by Hirth and from Grabke)

Segregant	$-\Delta g_b$	$-\Delta g_s$
C	50-75	73-85 (⋆)
Sn	30-35	61-87 (⋆⋆)
P	32-41	76-80 (⋆⋆)
Sb	8-25	83-130
S	50-58	165-190
H	65-68	71-109

Note: Δh and Δg at T other than 300 K may be estimated from $\Delta g = \Delta h - T\Delta s^\circ$, with $\Delta s_b^\circ \approx 0.02$-$0.03$ kJ/mol K and $\Delta s_s^\circ \approx 0$-$0.03$ kJ/mol K.

⋆ Not available for polycrystal surface; 85 kJ/mol is for (100) crystal surfaces.

⋆⋆ Values reported for low index crystal surfaces are higher: 180 kJ/mol for P and > 200 for Sn.

reductions, note that

$$(2\gamma_{\text{int}})_0 = 2\gamma_s - \gamma_b \approx 2(1.95) - 0.78 \approx 3.1 \text{J/m}^2$$

for a Fe boundary, using estimates of γ_s and γ_b from Hirth and Lothe (12).

To represent Γ, consider the grain boundary or free surface as a square grid of sites spaced by distance $b = 2.5 \times 10^{-10}$m. Then $\Gamma = 1.0/b^2 = 1.6 \times 10^{19}/\text{m}^2 = 2.65 \times 10^{-5}$ mol/m^2 corresponds to coverage of all grid sites. In Table 2, which shows reductions for separations at constant Γ, from eq. (7) and Table 1, we have used a comparitively low value of $\Gamma = 0.25/b^2$, *i.e.*, one-quarter coverage. This suffices to produce reductions which, for known embrittling segregants such as Sn, P, Sb and S in Fe, are of order 10% to 30% of $(2\gamma_{\text{int}})_0$. The

reduction scales with Γ, so long as $\Gamma < \Gamma_b^\circ$ and one is sensibly in the Langmuir-McLean range. For example, $\Gamma = 0.5/b^2$ leads to reductions of order 20% to 60% of $2\gamma_{int}$.

TABLE 2

Segregant-induced Reduction in Work of Separation, $2\gamma_{int}$, in J/m^2, for Fe Grain Boundaries at $T = 300$ K for Fixed Interfacial Composition, Γ, during Separation. (Results, in J/m^2, for $\Gamma = 0.25/b^2 = 4 \times 10^{18}/\text{m}^2 = 7 \times 10^{-6}$ mol/m^2.)

Segregant	$(2\gamma_{int})_{0^-} - (2\gamma_{int})_{\Gamma=const}$
C	−0.01-0.25(⋆)
Sn	0.18-0.40
P	0.25-0.34
Sb	0.41-0.85
S	0.75-0.98
H	0.02-0.31

Note: The results scale with Γ; *e.g.*, reductions are twice as large for $\Gamma = 0.5/b^2$ and half as large for $\Gamma = 0.125/b^2$.

⋆ Based on Δg_s for (100) crystal surface; if $-\Delta g_s$ for polycrystal surface is substantially smaller, as seems to be the case for P and Sn, then negative reductions in $2\gamma_{int}$ would be predicted. *I.e.*, C segregation would then increase $2\gamma_{int}$.

These effects are large but segregants can be much more deleterious when there is sufficient solute mobility so that the idealized limit is approached of separation at constant μ, *i.e.*, composition equilibrium with the bulk throughout the separation process. This case is difficult to deal with because simple L-McL adsorption isotherms, using segregation energies as in Table 1, suggest that the pair of free surfaces will usually be fully saturated after separation, *i.e.*, $\Gamma = 2\Gamma_s^\circ$ after separation, unless x is extraordinarily low or T high. In that case the L-McL model becomes inaccurate and segregant interactions, multi-layer coverage, *etc.* should be considered. Nevertheless, using the simple L-McL model, we make estimate for two interesting cases in Table 3.

The first is for high temperature separation in presence of S as a segregant, where there is assumed to be enough mobility for full composition equilibrium with the bulk concentrations indicated during separation. The effects in reducing $2\gamma_{int}$ are very large. Knott (13) argues that the high temperature stress relief cracking of steels near weld zones may be a consequence of the mobility of S, which then allows (as a high mobility limit) the sort of large reductions of $2\gamma_{int}$ shown in our table. It may be checked that the grain boundary coverage with S when it is at equilibrium with the bulk phase at the temperature assumed is negligible for the first two x values shown. Thus $2\gamma_{int}$ would be barely reduced in "fast" separation, at constant $\Gamma[= \Gamma_b(\mu)]$ in those cases but it is seen to be reduced by a large amount for "slow" separation of fixed μ in those same cases.

The second illustration in Table 3 is for H in Fe at 300K. Bulk concentrations and the pressures on a H_2 gas phase with which they are in equilibrium are indicated. Over this broad pressure range, H is seen to substantially reduce $2\gamma_{int}$ assuming, of course, that it is sufficiently mobile and the fracture process is slow enough for conditions of separation at constant μ to be approached. For the same choice of Δg values, the reduction of $2\gamma_{int}$ in Table 2, for separation at constant Γ, would be 0.17 J/m^2 with $\Gamma = 0.25/b^2$, and this increases to 0.67 J/m^2 if we make Γ as large as possible, *i.e.*, $\Gamma = \Gamma_b^\circ = 1.0/b^2$ in this illustration. The values in Table 3 for separation at constant μ are much larger and this, again, shows the effect of mobility of the solute in embrittlement.

Some guidelines for characterizing embrittling versus beneficial, and perhaps even cohesion enhancing, segregants emerge from those considerations, assuming that it is proper to focus on the effect of the segregant on $2\gamma_{int}$ as a key to understanding embrittlement. A deleterious segregant has a large value of the integrands in eqs. (4) and (5.). Essentially, this translates by eq. (7) into large values of $\Delta g_b - \Delta g_s$ at the fracture temperature and abundant segregation Γ. True cohesion enhancers should show negative values for the integrands of eqs. (4) and (5), as would be the case for an anomalous segregator which, at a given potential, segregates more to a grain boundary than to a pair of fracture surfaces. *E.g.*, B appears to show such segregation features in Ni_3Al, and it relieves the grain boundary brittleness normally shown in that system (14,15) and thus is probably a true cohesion enhancer. C appears to be a beneficial segregant

TABLE 3

Segregant-induced Reduction in Work of Separation, $2\gamma_{int}$, for Fe Grain Boundaries for Fixed Equilibrating Potential, μ, during Separation.

S at $T = 900$ K

($\Gamma_b^\circ = \Gamma_s^\circ = 0.5/b^2, \Delta g_s = -175$ kJ/mol, $\Delta g_b = -55$ kJ/mol)

x_S	$(2\gamma_{int})_0 - (2\gamma_{int})_{\mu=const}$
10^{-8}	0.96 J/m^2
10^{-6}	1.86 J/m^2
10^{-4}	2.73 J/m^2

H at $T = 300$ K

($\Gamma_b^\circ = \Gamma_s^\circ = 1.0/b^2, \Delta g_s = -90$ kJ/mol, $\Delta g_b = -66$ kJ/mol)

x_H	$P_{H_2}(\star)$	$(2\gamma_{int})_0 - (2\gamma_{int})_{\mu=const}$
1.94×10^{-9}	0.01 atm	1.71 J/m^2
1.94×10^{-8}	1.0 atm	1.87 J/m^2
1.94×10^{-7}	100 atm	2.02 J/m^2

$\star$ Related to x_H, by (Hirth [10]) 1.8×10^{-3} (P/atm)$^{1/2} \times \exp(-3440$ K/T), here 1 atm= 10^5 N/m^2.

in Fe in two ways. First, because it has a relatively high segregation energy to the grain boundary, it tends to displace, by site competition, other more deleterious segregants which may be present there [*e.g.*, 11, 16, 17, 18)]. Our results in Tables 1 and 2 suggest that C is, in fact, a modest cohesion degrader, less harmful than, say, P or Sb. On this basis Rice (1) suggested that the entire beneficial effect of C is due to displacement. However, that conclusion may be based on the lack of polycrystalline surface segregation energy data for C; see (2) and footnotes to Tables 1 and 2. It is possible that C might actually lower $2\gamma_{int}$. In any event, there are convincing experiments (17,18) showing that in addition to the displacement effect by site competition, C has a further beneficial effect which seems to mark it

as a true cohesion enhancer. It is thus unresolved as to whether the effects of C on cohesion are sensibly explained in terms of its effect on $2\gamma_{int}$.

DISLOCATION EMISSION FROM A CRACK TIP

The Kelly-Tyson-Cottrell and Rice-Thomson approaches have focussed on the competition of dislocation emission and atomic decohesion as a fundamental test of whether a given crystal or interface may cleave. An important idea in the Rice-Thomson model and refinements to it is that a critical crack tip loading is required for crack tip dislocation emission. This concept has been supported by experimental observations of loaded crack tips in several f.c.c. and b.c.c. materials (19). We will briefly discuss the features of and reservations in using the model as revised by Mason (20), which compares two local crack tip values of G associated with dislocation emission (G_{disl}) and cleavage-like decohesion ($G_{cleav} = 2\gamma_{int}$), or equivalently, the local elastic stress intensity factors $(K_M)_{disl}$ and $(K_M)_{cleav}$ for a given loading mode M. In addition to impurity effects on G_{cleav} discussed earlier, impurity segregation to the dislocation core, stacking fault (if a partial), and blunting ledge at the crack tip is predicted to lower G_{disl}.

The geometry for dislocation emission is shown in Fig. 2, where an emergent semicircular dislocation loop of radius r and Burgers vector of magnitude b and direction angle ψ is positioned on a slip plane at angle ϕ. The crack tip is completely contained by the slip plane. The energy to introduce the dislocation loop into a loaded crack tip region is written as (21,22,6,1)

$$U = \pi r[E_{core} + \alpha b^2 \ln(8mr/e^2 b)] + 2rE_{ledge} - 3.5br^{3/2}K_M S_M \ . \quad (11)$$

The last term is the work produced by the crack tip stress field, described by K_M, acting through the slip displacement b; the preceding term is the energy (E_{ledge}, per unit length) of the crack tip blunting ledge left by the dislocation, and the first two terms with $m = 1$ represent one-half of the total self energy of a full circular loop of radius r in an uncracked, infinite body. The factor m is included to describe the exact elastic interaction between a dislocation loop and a crack; its value depends on ψ and ϕ and is estimated between approximately 1.2 and 2.3 for a representative case of partial

and full dislocation nucleation in f.c.c. crystals and along symmetric tilt interfaces (23,24). In the full circular loop expression, E_{core} is the average energy per unit length contained within a cylinder of radius b of the dislocation line and αb^2 is the average of the prelogarithmic energy factor over all straight dislocation lines positioned in the loop plane and having Burgers vector b of the loop. Thus, $\alpha = (2-\nu)\mu/8\pi(1-\nu) \approx \mu/10$ for an isotropic solid with elastic shear modulus μ. Further, $E_{\text{core}} = \alpha b^2 \ln(b/r_0)$ provides a relation between the familiar dislocation core cutoff r_0 and E_{core}.

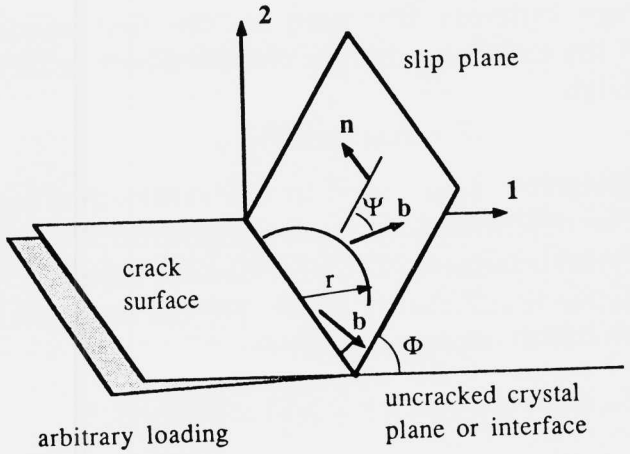

FIG. 2. Geometry for an emergent semicircular loop at a crack tip.

The loop nucleation condition is given by satisfying $dU/dr = 0$ and $d^2U/dr^2 = 0$, and yields

$$(K_{\text{M}} S_{\text{M}})_{\text{disl}} = \frac{1.2\alpha b^{1/2}}{\sqrt{r/b}} \quad , \tag{12}$$

where the corresponding critical loop radius is

$$r = \frac{e^3}{8m} \exp\left[-\left(\frac{E_{\text{core}}}{\alpha b^2} + \frac{2E_{\text{ledge}}}{\pi \alpha b^2}\right)\right] . \tag{13}$$

The orientation factors S_{M} are functions of the loading mode M, angles ψ and ϕ, and elastic properties of the materials joining the interface so that $K_{\text{M}} S_{\text{M}}/\sqrt{\rho}$ is the resolved shear traction acting on

the slip plane in the direction of $\vec{b}$, at a distance ρ from the crack tip. In particular, for a crack in an isotropic body under mode 1 loading,

$$S_1 = \sqrt{1/8\pi}\cos(\phi/2)\sin\phi\cos\psi \ .$$

Equation (12) describes a planar surface in K-space (25,21) with intercepts $K_M^0 = 1.2\alpha b/\sqrt{r}S_M$ along each axis as shown in Fig. 3. Thus, the critical condition for emission is defined as that point along a given path of local crack tip loading which intersects the planar surface.

The cleavage criterion discussed in the first section of the manuscript and the emission criterion discussed here in terms of K_M are related through

$$G = K_M \Lambda_{MN} K_N \ , \tag{14}$$

where the components Λ_{MN} used in the summation over M,N = 1,2,3 above can be determined for cracks in anisotropic single crystals (26) or along crystal interfaces (27), provided the region of oscillatory stresses in the latter is sufficiently small. For the intergranular crack in an isotropic material, eq. (14) becomes

$$G = [(1-\nu)/2\mu](K_1^2 + K_2^2) + (1/2\mu)K_3^2 \ ,$$

where ν = Poisson's ratio. If G above is equated to G_{cleav} defined in eq. (1), the cleavage decohesion surface may be drawn as a quadratic surface in Fig. 3, with intercepts of K_1 and K_2 equal to $\sqrt{2\mu G_{cleav}/(1-\nu)}$, and K_3 equal to $\sqrt{2\mu G_{cleav}}$. Equivalently, one may use eq. (14) to calculate G_{disl} and compare it to G_{cleav}, although it is important to note that no unique value of G_{disl} exists for a general mixed mode loading, since the critical condition is a function of $(K_M S_M)_{disl}$.

There are considerable uncertainties in calculating $(K_M S_M)_{disl}$ or G_{disl} as outlined, so that results should be taken as suggestive. The emission criterion has only been calculated in the context of linear elasticity, and depends on poorly characterized parameters describing an inherently atomistic structure such as the dislocation core energy, the energy of the dislocated ledge at the loaded crack tip, and configurations of very-near-tip dislocation loops. Often, the critical values of r estimated by eq. (13) are of order one to two Burgers vectors and are well outside the range of continuum elastic dislocation theory. At best, a lower bound to $(K_M S_M)_{disl}$ can be obtained in such

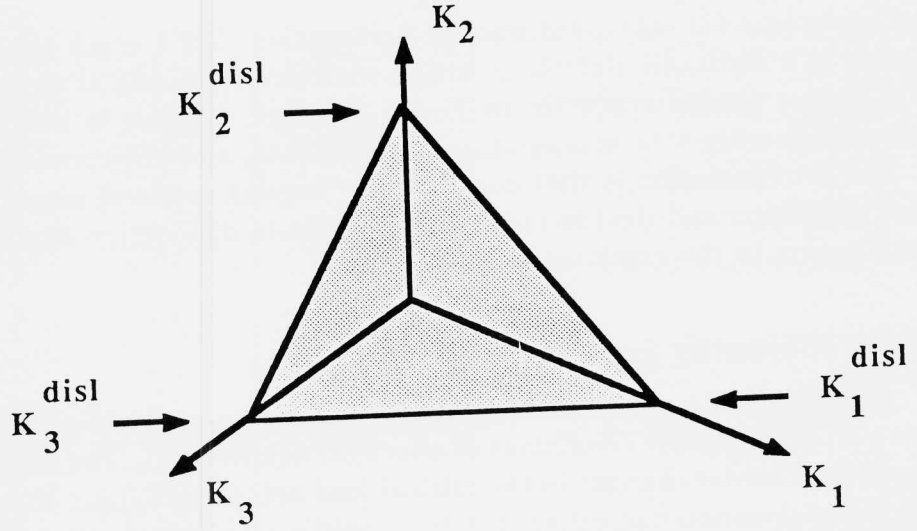

FIG. 3. Graphical representation of eq. (12), showing conditions for dislocation emission in terms of local stress intensity factors.

cases by substituting for r in eq. (12) the smallest value at which a continuum elastic approach is expected to be valid. In addition, the assumed geometry that the crack tip lie completely in a slip plane may favor dislocation emission, since other geometries would require some crack alignment to the slip plane or complicated dislocation loop jogs in order to emit a dislocation. Finally, dislocation loop shapes should be a function of the elastic anisotropy, core and ledge energies, and the local, perhaps mixed crack tip loading; thus, any constraint on shape should in principle overestimate the critical load set, $(K_M S_M)_{disl}$.

Three final, but important reservations concern the validity of the G_{disl} versus G_{cleav} approach outlined. In many cases of interest, brittle phase nucleation sites (situated perhaps in front of a large, stationary crack) may act as points of injection of rapidly moving cracks into the matrix, and the prediction that a stationary crack emit a dislocation may not be applicable to such a dynamic situation (28). Further, cracks predicted as intrinsically brittle by the criterion proposed may in fact blunt and relax from diffusive plastic flow of nearby dislocation not considered in the analysis. Rate effects, temperature, and current dislocation density (flow stress) may therefore control whether a local energy release G_{cleav} may exist at the crack tip (29,30). Finally, experimental work of Vehoff, Neumann,

and coworkers (31–34) questions the assumption that a crack tip responds in a distinctly ductile or brittle manner. Here, the sharpness of a fatigue loaded crack tip in Fe-3% Si single crystals is seen to vary significantly with temperature, loading rate, and environmental H. The interpretation is that continuously varying levels of cleavage crack extension and ductile crack opening due to dislocation slip are contributing to the crack tip opening angle.

Effects of Impurity Segregation on $(K_M S_M)_{disl}$

The effect of a solute on the reversible work to nucleate a dislocation is discussed for conditions of chemical equilibrium. The result is used to consider changes in the critical load set, $(K_M S_M)_{disl}$ in eq. (12), for dislocation nucleation due to a rapidly mobile impurity such as H in Fe.

Consider a body at pressure P and temperature T from which we may adsorb/desorb a solute and in which we may form dislocations. A reversible change in the internal energy of the body is given by

$$dU = TdS - PdV + \mu_H dn_H + e\, d\ell \quad , \tag{15}$$

where n_H and μ_H are the number and chemical potential of the solute atoms (denoted here by 'H' for application to hydrogen) in the system, and e is the free energy per unit length of dislocation formed. Analogous to surface or grain boundary free energy, e is the reversible work required to effect unit increase in dislocation line length, and we assume $e = e(\mu_H, P, T, \ell)$ in general, with a simpler model being e independent of ℓ. This representation is an approximation, in that not all energy changes associated with alteration of dislocation line positions and introduction of new dislocations can be described by such a parameterization.

For conditions where a dislocation of length $d\ell$ is introduced into the body at constant P, T and $\mu_H = \mu_0$, it is convenient to define the following state variable

$$d\Lambda = d(U + PV - TS - \mu_H n_H) = -SdT + VdP - n_H d\mu_H + e\, d\ell \quad .$$

Therefore, the reversible work to enlarge the total dislocation length by $d\ell$ at constant P, T, and $\mu_H = \mu_0$ is given by

$$e = \left(\frac{\partial \Lambda}{\partial \ell}\right)_{P,T,\mu_H} = \left(\frac{\partial G}{\partial \ell}\right)_{P,T,\mu_H} - \mu_0\, \Gamma(P, T, \mu_0, \ell) \quad ,$$

where $\Gamma = (\partial n_H/\partial \ell)_{P,T,\mu_H}$ is defined as the excess number of solute atoms associated with a unit length of dislocation. From the expression for Λ, we may obtain the following Maxwell relation,

$$\left(\frac{\partial e}{\partial \mu_H}\right)_{P,T,\ell} = -\left(\frac{\partial n_H}{\partial \ell}\right)_{P,T,\mu_H} = -\Gamma(P,T,\mu_H,\ell) \ .$$

The above equation may be integrated along a path of constant P, T, ℓ from $\mu = -\infty$ (corresponding to absence of solute in the system) to $\mu_H = \mu_0$,

$$e_H = e_0 - \int_{-\infty}^{\mu_0} \Gamma(\mu_H)\, d\mu_H \ . \tag{16}$$

Thus, the reversible work of forming a unit length of dislocation in the presence of a solute is given above, with e_0 equal to the work of formation in the absence of solute.

Equation (16) is evaluated for conditions where the dislocation is formed at chemical equilibrium between the solute and the bulk and dislocation core sites. A McLean isotherm (see eq. (10)) is used to define the equilibrium excess Γ_d at the dislocation in terms of the lattice concentration x, the segregation free energy Δg_d to the dislocation sites, and the saturation excess level Γ_d° at the dislocation. Since the solute is assumed to be dilute in the lattice, $(d\mu_H)_{P,T} = RTdx/x$, and eq. (16) is evaluated as

$$e_H = e_0 - RT\Gamma_d^\circ \ln[1 + x\exp(-\Delta g_d/RT)] \ . \tag{17}$$

The fact that chemical equlibrium is assumed between the bulk and dislocation allows e_H to be expressed directly in terms of x.

The same treatment may be applied to the dislocation ledge, or the stacking fault left by a partial, assuming that the free energies of each are dependent only on P, T, and μ_H. In such cases, E_{core} and E_{ledge} appearing in the criterion for emission of a full loop dislocation (see eq. (12)) may be replaced by using eq. (17). The critical condition for nucleation would be given in terms of the pure system value, thus

$$\begin{aligned}(K_M S_M)_H = &(K_M S_M)_0 \\ &\times [1 + x\exp(-\Delta g_d/RT)]^{-RT\Gamma_d^\circ/2\alpha b^2} \\ &\times [1 + x\exp(-\Delta g_{ledge}/RT)]^{-RT\Gamma_{ledge}^\circ/2\alpha b^2}\end{aligned} \tag{18}$$

where subscripts 'd' and 'ledge' denote quantities evaluated for the dislocation and ledge, respectively. For conditions where the dislocation core and ledge act as segregation sites (*i.e.*, Δg_d, $\Delta g_{\text{ledge}} < 0$), the effect of adding an impurity to the bulk material is seen to reduce the critical load set, $(K_M S_M)_{\text{disl}}$, for dislocation emission. This effect is intended to complement impurity effects on atomic decohesion discussed earlier, and on diffuse plastic flow from external, non-crack-tip dislocations as discussed by Hirth for H in Fe (10). The effect of H on dislocation emission in Fe is difficult to estimate, since Γ_d° and Γ_{ledge}^0 are poorly known. For comparison, the binding energy of H to a nonscrew dislocation in Fe is estimated as –58.6 kJ/mol (35), which is considerably lower than either the estimate of –95 kJ/mol for a carbide interface (36) or –104 kJ/mol for a Fe (110) surface (37).

Another possible effect of impurity segregation, not considered here, is that large-atomic-size segregants may retain some residual misfit even after segregation along the grain boundary. A first analysis (38) suggests that this may impede dislocation nucleation at the tip.

APPLICATION TO Cu-Bi INTERFACIAL CRACKS

The Prediction of the Model

Earlier work by Wang *et al.* (6) has outlined theoretical estimates of G_{cleav} and G_{disl} for mode 1 cracks on Cu-Bi [110] symmetrical tilt interfaces. The resulting estimates predict strong differences in G_{cleav} and G_{disl} which depend on the particular crystallographic interface, the crack growth direction, and the amount of Bi segregated to the interface. The closing section of this manuscript reports on experimental observations of fracture surface morphology in mode 1 tested Cu-Bi bicrystals, in an effort to determine how useful and fundamental is the G_{cleav} versus G_{disl} approach outlined.

Here we give improved estimates for the critical G values of Wang *et al.* (6). Their work was based on an approximate estimate (21,22) of the correction factor m for dislocation self energy, of eq. (11); here we use the results of subsequent exact continuum elastic calculations (23). Also, the grain boundary segregation energy, $-\Delta g_b$, for the $\Sigma 11$ boundary was overestimated in their work (9).

Using a 3-D weight functions Gao and Rice (23) derived the self

energy of a crack-tip dislocation loop and computed the energy correction factor m as a function of ϕ and ψ. Computations showed that for a semicircular loop $m(\phi,\psi)$ decreases monotonously with increasing ϕ and this angular dependence is the strongest at $\psi = 0^0$ and becomes weaker as ψ increases. Since G_{disl} is scaled by a factor of m for a mode 1 loading, using new values of m modifies the orientation dependence of G_{disl}.

The misorientation and structural dependence for grain boundary segregation has been the subject of wide interest in recent years and a variety of results, sometimes contradictory, have been published. In spite of inconsistencies of data from different laboratories, experimental results (24,39) and theoretical analysis (40,41) suggest that segregation to $\Sigma 11$ $[110]/(1\bar{1}3)$ boundaries is very unlikely. The value of Δg_b used by Wang *et al.* (6) is an overestimate and a much lower value was estimated by Wang (24). This leads to a stronger misorientation dependence of the effect of Bi content on G_{cleav}. Combining corrections for the values of m and the values of $-\Delta g_b$ for the $\Sigma 11$, $\Sigma 9$ $[110]/(2\bar{2}1)$ and $\Sigma 41$ $[110]/(4\bar{4}3)$ boundaries, Wang (24) recently recalculated G_{cleav} and G_{disl} for model 1 cracks on Cu-Bi [110] symmetrical tilt boundaries.

The estimates reported in Wang (24) are shown in Fig. 4 which displays G_{cleav} and G_{disl} for three representative grain boundaries, with crack growth in either $[n\bar{n}\bar{m}]$ (denoted by $(+)$) or $[\bar{n}nm]$ (denoted by $(-)$) opposing directions as to contain the crack front completely in a $\{111\}$ slip plane as required by the model. The solid black line then divides cleavage and ductile behavior into two regions based on $G_{\text{cleav}} > G_{\text{disl}}$ and $G_{\text{cleav}} < G_{\text{disl}}$, respectively.

Estimates for a pure boundary at room temperature are shown in Fig. 4 by the rightmost point on a given horizontal line, and the effect of Bi segregation is to move leftward, reducing $2\gamma_{\text{int}}[= G_{\text{cleav}}]$. G_{disl} is assumed to be unaffected by the immobile Bi, and is shown here for the nucleation of two partials on the $\{111\}$ planes symmetrically disposed about the interface rather than for the full (undissociated) loop as described earlier. The partial calculation is similar, and is outlined in detail by Anderson (21) and Wang *et al.* (6). In particular, the energy U_1 associated with nucleation of the first partial is written as for U in eq. (11), except now a term $\pi r^2 \gamma_{sf}/2$ is added to account for the energy of the stacking fault. For the mode 1 loading discussed here, the first partial is found to expand to a stable radius of order

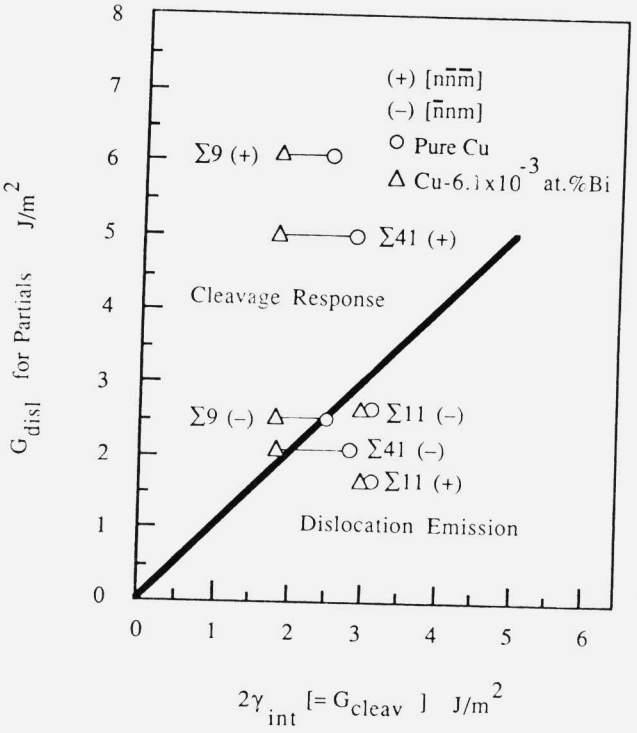

FIG. 4. Predictions of cleavage and partial dislocation emission for interfacial cracks on three representative Cu-Bi [110] symmetric tilt boundaries. The effect of Bi segregation is to move the prediction for a given crack geometry leftward on the horizontal lines shown. (+) and (−) denote opposite crack orientations on a boundary.

$100b$ to $1000b$ due to the dominance of the stacking fault term at large r. The energy U_2 of the second partial is written as U in eq. (11), with an added term $-\pi r^2\gamma_{sf}/2$ to account for the removal of the stacking fault, and an added interaction energy between the first and second partials. The calculation yields $(K_1)_{\text{disl}}$ values for the first and second partials which bound that for nucleation of the full dislocation in a given orientation. Even though the calculation predicts a lower load to nucleate the full dislocation than the partials, the latter is regarded as more plausible since once the first partial is nucleated, the possibility of a full, undissociated loop has disappeared. There are considerable uncertainties involved in the estimate of core and ledge energies which are discussed along with the other parameter choices needed for G_{disl} in (21).

Predictions of G_{cleav} are based on separation at constant Γ so

that eq. (7) is applicable. A more complete discussion of appropriate parameter choices to apply eq. (7) to Cu-Bi interfaces is found in (9,21,24). The Bi concentration, Γ, residing on the interface is estimated assuming equilibration of the interface and bulk solute at the annealing temperature, $T_a = 723$ K. Thus, eq. (10) is used to calculate Γ for the bulk (lattice) concentration of $x = 6.1 \times 10^{-3}$ at. %, estimating $\Gamma_b^\circ = 3.41 \times 10^{-5}$ mol/m^2 and taking $\Delta g_b = -67.6$ kJ/mol, -56.6 kJ/mol and -42.8 kj/mol for the $(4\bar{4}3)$, $(2\bar{2}1)$ and $(1\bar{1}3)$ boundaries, respectively (24). Values of $(2\gamma_{\text{int}})_0$ are based on the free energy difference, $2\gamma_s - \gamma_b$, between two clean free surfaces and the clean grain boundary, and are predicted to vary by up to 20% due primarily to variation of γ_b with orientation (21).

Several features are seen from Fig. 4: 1. Grain boundary orientation is important in determining the nature of crack tip response, due to variations in $2\gamma_{\text{int}}$ and G_{disl}. The $(1\bar{1}3)$ boundary is most ductile, because its low grain boundary free energy and segregation energy and the orientation of the slip planes at the crack tip are favorable for dislocation emission. The strong dependence on slip plane orientation causes the difference in G_{disl} among the three boundaries to be more significant if the crack propagates in the $[n\bar{n}\bar{m}]$ direction. 2. Segregation of Bi to the boundary reduces $2\gamma_{\text{int}}$ and hence embrittles the $(2\bar{2}1)$ and $(4\bar{4}3)$ boundaries. The $(1\bar{1}3)$ boundary is not embrittled by Bi segregation due to a smaller segregation energy. Decreases in $2\gamma_{\text{int}}$ are in the range of 5% and 35% when $x = 6.1 \times 10^{-3}$ at. % , depending on the grain boundary. 3. The direction of the crack propagation strongly affects the ductile versus brittle response because of the difference in the resolved shear stress acting on the active slip plane. The difference is large for $(4\bar{4}3)$ and $(2\bar{2}1)$ boundaries, so that the bicrystals are predicted to be ductile when the crack grows in along one direction, and become brittle if the crack propagates in another direction. In cases where the crack tip is not coplanar with a slip plane, crack propagation may tend to a cleavage mode.

Experimental Results

In order to check the prediction of the model, two symmetrical [110] tilt grain boundaries, $\Sigma 11[110]/(1\bar{1}3)$ and $\Sigma 9[110]/(2\bar{2}1)$, were studied. As a comparison, one symmetrical [100] tilt grain boundary, $\Sigma 5[100]/(031)$, and one asymmetrical random grain boundary

were also studied. The bicrystals were grown by the vertical Bridgeman technique. The bulk concentration is believed to be lower than 100 ppm (0.003 at. %) Bi except for the $\Sigma 5$ bicrystal. Different heat treatments were applied. The notches were made along grain boundaries. Specimens were fractured and the fracture surfaces were compared. The detailed experimental procedure and results were described elsewhere (24) and the experimental results are summarized as follows.

The $\Sigma 11$ bicrystal is essentially ductile after any heat treatment. After annealing at 723 K or 773 K in vacuum the specimen could not be broken by bending. The surface newly created by bending at the near tip region is shown in Fig. 5, which is a so called tearing topography surface (42) and the appearence of this type of fracture surface indicates an excellent ductility. Doping with Bi by annealing the specimen in Bi vapor did not reduce the ductility notably, but occasionally small areas of the faceted boundary could be found on the background of the tearing topography surface (Fig. 6). The bicrystal was slightly embrittled by annealing in the liquid Bi bath for a long time. After this treatment, a mixed fracture surface appeared with the major area still being transgranular and small areas of intergranular fracture along the faceted interface as shown in Fig. 7. These results indicate that the $\Sigma 11$ boundary is highly resistent to Bi segregation and embrittlement.

The $\Sigma 9$ grain boundary is also ductile after the segregation treatment by annealing at 723 or 773 K in vacuum. From the ease of breaking the specimen by bending, its ductility is lower than $\Sigma 11$. By annealing in Bi vapor, the $\Sigma 9$ boundary was severely embrittled. A faceted quasi-cleavage topography surface appeared in the curved area of the boundary (Fig. 8). The detailed discussion (24,43) showed that this type of faceted structure consists of three mutually perpendicular crystallographic planes which are 2 sets of {110} type planes and 1 set of serrated {100} type planes. The appearance of this type of fracture surface seems to be related to a special type of intergranular brittle fracture where the cracking path is apparently not coincident with the boundary plane at the microscopic level. Rather it may wander along the boundary by cleavage of {110} plane and dislocation slip, which produces the serration of {100} planes.

The random grain boundary studied is usually brittle after annealing at 723 or 773 K in vacuum. When the annealing temperature

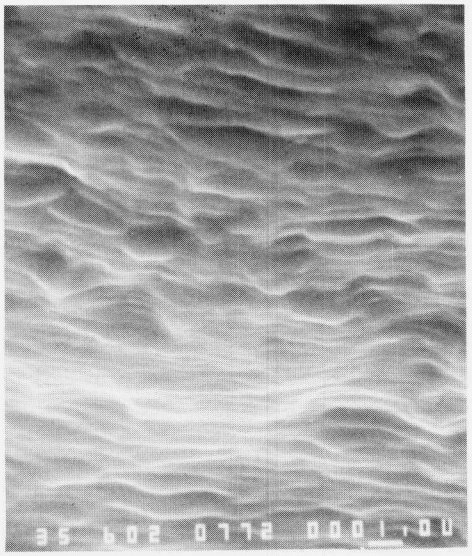

FIG. 5. The tearing topography surface of the Σ11 bicrystal. (723 K in vacuum for 96 hours)

Fig. 6. The small faceted fracture area of the Σ11 bicrystal. (1123 K, 24 hrs. + 773 K, 24 hrs in Bi vapor)

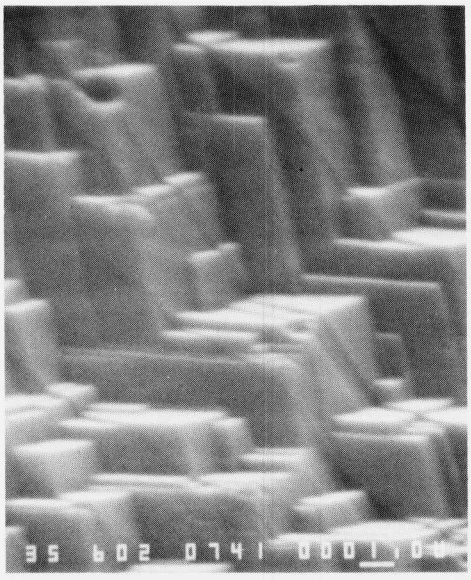

FIG. 7. The small faceted fracture area of the Σ11 bicrystal. (1123 K 24 hrs + 723 K, 96 hrs in Bi bath)

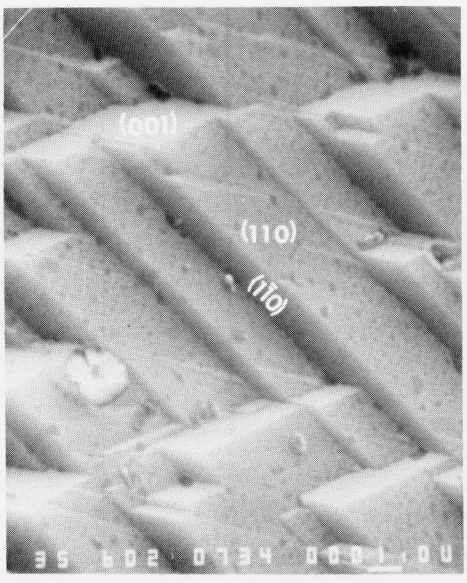

FIG. 8. The faceted quasi-cleavage topography surface of the Σ9 bicrystal. (1123 K 24 hrs + 723 K 96 hrs. in Bi vapor)

was low (723 K) so that grain boundary faceting did not occur, a curved boundary fractured in a brittle manner producing the faceted quasi-cleavage topography surface (Fig. 9). At higher annealing temperature (773 K) the curved grain boundary was faceted, resulting in a faceted intergranular fracture surface (Fig. 10) with the elongated facet direction along the un-curved direction and regular steps that accommodate the macroscopic curvature. In contrast for a planner boundary after annealing at higher temperature (773 K), only small scale faceting occurred and resulted in a mixed fracture surface with neither the large scale faceting nor faceted quasi-cleavage topography surface.

The $\Sigma 5$ grain boundary is brittle in the as-grown condition. A thermal contraction crack formed along the interface during solidification and cool-down of the bicrystal. The crack was readily propagated under a tensile load, leading to a very low ductility and a variety of brittle fracture surfaces, which are composed of the faceted quasi-cleavage topography surface (Fig. 11), the large scale faceted intergranular fracture surface and also the relatively flat fine scale faceted intergranular fracture surface (Fig. 12).

The experimental results are consistent with the theoretical predictions in Fig. 4 that the $\Sigma 11$ grain boundary is ductile and it cannot be embrittled by segregation regardless of the cracking direction and the heat treatment. The $\Sigma 9$ bicrystal could not be embrittled by segregation but it was severely embrittled by doping with Bi. This is, to some extent, consistent with the prediction in Fig. 4 when cracking is in the $[\bar{1}14]$ direction, considering that the bulk concentration of the bicrystal is lower.

The model can only deal with the situation that the crack front is situated in a potentially active slip plane. This geometry seems to provide the most favorable condition for dislocation emission. For any other geometries dislocation emission is expected to be more difficult. The brittle behaviors of the $\Sigma 5$ and the random grain boundaries are thus compatible with this framework. On the other hand, propensities of Bi segregation in the $\Sigma 5$ and the random grain boundaries are expected to be large from the consideration of the excess volume of the boundary plane [44] or from the newly suggested argument that the most important geometrical parameter governing the behavior of special interfaces is the interface spacing of the lattice planes parallel to the interface plane (45). The reduced decohesion energy of the

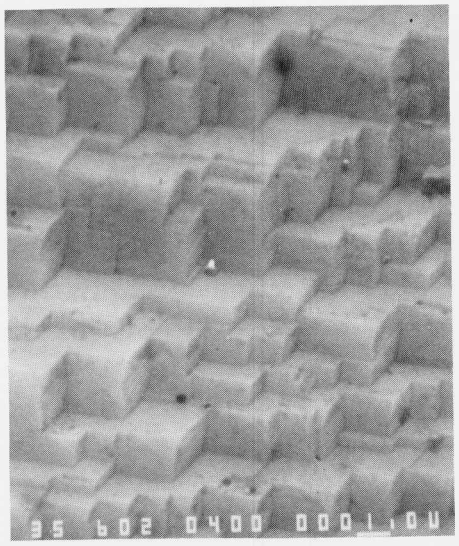

FIG. 9. The faceted quasi-cleavage topography surface of the random boundary. (723 K, 96 hrs. in vacuum)

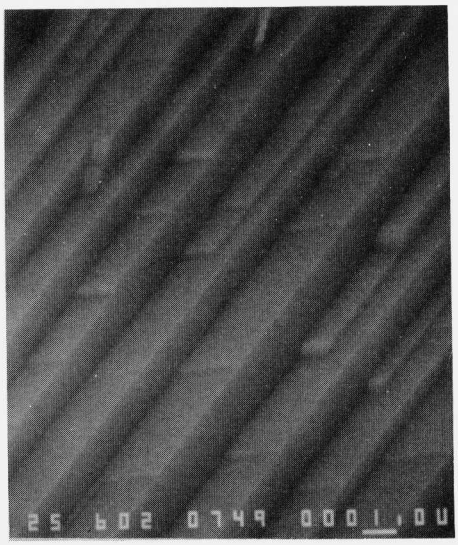

FIG. 10. The faceted intergranular fracture surface of the random boundary. (773 K 24 hrs in vacuum)

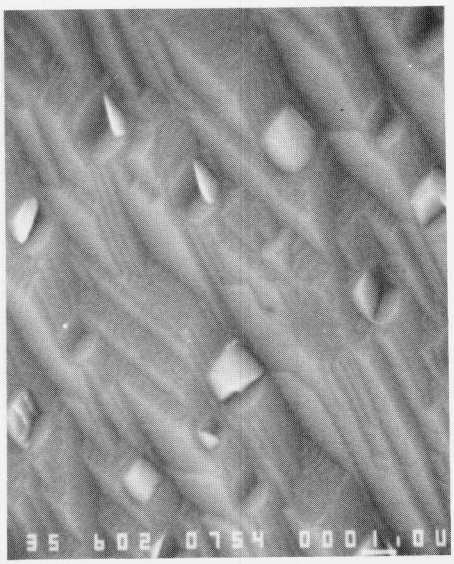

Fig. 11. The faceted quasi-cleavage topography surface of the Σ5 bicrystal. (as-grown)

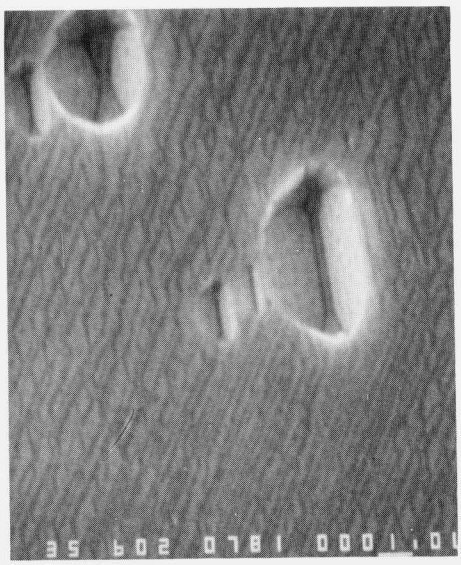

FIG. 12. The fine scale faceted intergranular fracture surface of the Σ5 bicrystal. (as-grown)

interface combining with the difficulty in dislocation emission leads to low ductilities of the $\Sigma 5$ and the random boundaries.

An important prediction of the model is that the ductile versus brittle response of an interfacial crack depends on the cracking direction, and in some cases, *e.g.* for the $\Sigma 9$ boundary, the dependence may be very strong. This prediction was verified indirectly by tests on a what was supposed to be 'pure' Cu $\Sigma 9$ bicrystal. A fatigue strain hardened specimen cut from this bicrystal was sectioned to form two specimens and notches were cut along the interfaces in opposite directions. One was in the $[1\bar{1}\bar{4}]$ direction, the other in $[\bar{1}14]$. The two notched specimens were fatigue tested again. It turned out that the fracture behaviors of the two specimens are completely different. The one with the $[1\bar{1}\bar{4}]$ direction notch fractured at a lower load in fewer cycles and the fracture surface appeared to be brittle intergranular. The one with the $[\bar{1}14]$ direction notch fractured at a much higher load in a large number of cycles and the fracture surface was transgranular with well developed fatigue striations. We cannot take this test as full evidence for the model prediction because a large number of sulphides were found on the fracture surface of the brittle specimen, and these particles might be the source of the brittleness. Thus, we can not be certain from this test whether the $\Sigma 9$ boundary in pure Cu is ductile or brittle when cracking in the $[\bar{1}14]$ direction. But the result is compatible with the theoretical prediction in the sense that the only difference between the two specimens is the cracking direction, and their response is significantly different.

SUMMARY DISCUSSION

We have presented thermodynamic and mechanical models of interfacial embrittlement, illustrating results with applications to various segregants (H, C, P, Sn, Sb, S) on Fe grain boundaries, and have described studies of Cu bicrystals with Bi segregation as a model system to test theoretical concepts.

The thermodynamic formulation for interfacial decohesion in presence of a segregating species relates the work of separation, $2\gamma_{\text{int}}$, to segregation free energies at the grain boundary (Δg_b) and pair of surfaces (Δg_s) created by fracture. Separation in presence of a mobile segregant, which can allow approach to idealized limiting conditions of separation at constant equilibrating potential of the segre-

gant, leads to substantial reductions in $2\gamma_{int}$, as shown for H and S in Fe. The more typical case at low temperatures, of separation at fixed composition, leads to smaller but still significant reductions of $2\gamma_{int}$, illustrated for various segregants in Fe.

Segregants which decrease $2\gamma_{int}$, and thus presumably embrittle grain boundaries, have relatively large values of $\Delta g_b - \Delta g_s$ and sit with abundant coverage Γ at the boundary. Those which increase $2\gamma_{int}$, and are presumably true cohesion enhancers, have negative values of $\Delta g_b - \Delta g_s$ as is apparently the case for B in Ni_3Al. A segregant can be beneficial, however, so long as it simply does not have a large value of $\Delta g_b - \Delta g_s$ and acts to displace other more deleterious segregants from the boundary. Such displacement is to be expected if $-\Delta g_b$ is large, because then the segregant wins out over others by site competition. C in Fe is beneficial partly because it has a high $-\Delta g_b$ and displaces other deleterious elements from the boundary. It also seems to have an additional beneficial effect, but estimates based on currently available surface segregation data suggest that it modestly decreases, rather than incrases, $2\gamma_{int}$. This conclusion may, however, change if segregation energy data becomes available for C segregation to the general polycrystal surfaces of intergranular fractures, rather than just to a (100) crystal surface as at present.

Updates of the Rice-Thomson formalism were outlined for addressing the competition between cleavage decohesion and blunting by dislocation emission for atomistically sharp cracks along interfaces. This is to determine if an interface is intrinsically cleavable for a given direction of cracking along it. As we discuss, factors relating to the presence and mobility of nearby dislocations (and hence to loading rate and temperature) will often control whether an interface, judged as intrinsically cleavable, will actually fail by cleavage.

Aspects of the modelling discussed here include more exact estimates by continuum elasticity of the self-energy of dislocation loops emerging from a crack tip, the possibility of nucleation in a partial dislocation mode, and effects of a mobile solute, notably H, which could segregate along an emerging loop.

The theory for the dislocation emission versus cleavage competition is applied to a model system of Cu bicrystals, symmetrically tilted about [110], on the boundary of which Bi may segregate. Detailed results are given for the $\Sigma 11/(1\bar{1}3)$ and $\Sigma 9/(2\bar{2}1)$ boundaries,

and predict that the latter is more readily affected by Bi and is more brittle. A dependence of load levels for dislocation nucleation on the direction of crack growth is found in the case of the $\Sigma 9/(2\bar{2}1)$ boundary. This relates to different orientations of potentially relaxing slip systems relative to the crack tip.

In coordinated experiments, several Cu-Bi bicrystals were grown, heat treated for segregation, and tested mechanically. These include the two [110] tilt cases just mentioned and also the $\Sigma 5[100]/(031)$ symmetrical tilt boundary and a high angle random grain boundary. Results for the two [110] tilt cases have qualitative consistency with the theoretical predictions, although the theory is probably inadequate to explain all results and could not be checked with much precision due to factors relating to nearby dislocations and uncontrolled impurities. Consistent with the theory, the $\Sigma 9[110]$ bicrystal is readily embrittled with Bi whereas the $\Sigma 11[110]$ remains ductile. Also, the $\Sigma 9$ bicrystal showed brittle interfacial fracture for one direction of crack growth but a highly ductile failure mode for the opposite direction.

In order of brittleness, the Cu-Bi bicrystals are $\Sigma 5[100]/(031)$, random, $\Sigma 9[110]/(2\bar{2}1)$ and $\Sigma 11[110]/(1\bar{1}3)$. The fracture surface morphologies are highly varied, often from place to place along the same boundary. Brittle intergranular fracture surfaces may have large planar areas, or be highly faceted. Sometimes the facets reflect interfacial facetting, as it thought to be induced by Bi segregation, but in other cases they seem to show a new type of interfacial brittle failure in which the crack path may not microscopically follow the boundary and forms flat cleavage like {110} facets and also {100} facets which sometimes show slip markings.

ACKNOWLEDGEMENT

This study was supported by the NSF Materials Research Laboratory at Harvard.

REFERENCES

1. J. R. Rice, in *Chemistry and Physics of Fracture* (R. M. Latanision and R.H. Jones, eds.) (Matinus Nijhoff Publishers, Dordrecht, 1987) p. 27.

2. J.R. Rice and J.-S. Wang, "Interfacial embrittlement by solute segregation", submitted to *Mater. Sci. Eng.*, 1988.
3. J. R. Rice, in *Effect of Hydrogen on Behavior of Metals* (A. M. Thompson and I. M. Berstein, eds.) (TMS-AIME, New York, 1976) p. 455.
4. J. P. Hirth and J. R. Rice, *Metall. Trans.* **11A**, 1502 (1980).
5. R. J. Asaro, *Phil. Trans. Roy. Soc. London* **A295**, 150 (1980).
6. J.-S. Wang, P.M. Anderson, and J.R. Rice, in *Mechanical Behaviour of Materials -V* (M.G. Yan, S.H. Zhang and Z.M. Zheng, eds.) (Pergamon Press, Oxford, 1987) p. 191.
7. P. Wynblatt and R. C. Ku, *Surface Sci.* **65**, 511 (1977).
8. P. Wynblatt and R. C. Ku, in *Interfacial Segregation* (W. C. Johnson and J. M. Blakely, eds.) (ASM, Metals Park, OH, 1979) p. 115.
9. J.-S. Wang, "Review of Data to Evaluate Segregation Effects on the Ductile-Brittle Transition in Cu-Bi Bicrystals," Harvard University, Informal Progress Report (unpublished), 1985.
10. J. P. Hirth, *Metall. Trans. A* **11A**, 861 (1980).
11. H. J. Grabke, *Steel Research* **57**, 178 (1986).
12. J. P. Hirth and J. Lothe, *Theory of Dislocations*, (McGraw-Hill, New York, 1968).
13. J. F. Knott, in *Chemistry and Physics of Fracture* (R. M. Latanision and R. H. Jones, eds.) (Martinus Hijhoff Publishers, Dordrecht, 1987) p. 44.
14. C. T. Liu, C. L. White and J. A. Horton, *Acta Metall.* **33**, 213 (1985).
15. C. L. White, *J. Vac. Sci. Technol.* **A4**, 1633 (1986).
16. H. J. Grabke, in *Chemistry and Physics of Fracture*, (R.M. Latanision and R. H. Jones eds.) (Martinus Nijhoff Publishers, Dordrecht, 1987), p. 388.
17. S. Suzuki, M. Obata, K. Abiko and H. Kamura, *Trans. Iron Steel Inst. Jap.* **25**, 62 (1985).
18. S. Suzuki, S. Tanii, K. Abiko and H. Kimura, *Metall. Trans.* **18A**, 1109 (1987).
19. S. M. Ohr, *Mater. Sci. Eng.* **72**, 1 (1985).
20. D. D. Mason, *Phil. Mag.* **39**, 455 (1979).
21. P. Anderson, "Ductile and Brittle Crack Tip Response" (Ph.D. Dissertation, Harvard University, 1986).
22. P. M. Anderson and J. R. Rice, *J. Mech. Phys. Solids* **35**, 743 (1987).

23. H. Gao and J. R. Rice, *J. Mech. Phys. Solids*, in press.
24. J.-S. Wang, "Fracture Surfaces of Embrittled f.c.c. Metal Bicrystals and their Misorientation Dependence," to be submitted to *Acta Metall.*
25. I. H. Lin and R. Thomson, *Acta metall.* **34**, 187 (1986).
26. P. C. Paris and G. C. Sih, in *Fracture Toughness Testing and its Applications*, (ASTM Spec. Tech. Publ. 381), (1965) p. 30.
27. J. R. Willis, *J. Mech. Phys. Solids* **19**, 353 (1971).
28. M. L. Jokl, V. Vitek, and C. J. McMahon Jr., *Acta metall.* **28**, 1479 (1980).
29. L. B. Freund and J. W. Hutchinson, *J. Mech. Phys. Solids* **33**, 169 (1985).
30. L. B. Freund, J. W. Hutchinson, and P. S. Lam, *Eng. Fracture Mech.* **23**, 119 (1986).
31. H. Vehoff and P. Neumann, *Acta metall.* **27**, 915 (1979).
32. H. Vehoff and P. Neumann, *Acta metall.* **28**, 265 (1980).
33. H. Vehoff, W. Rothe, and P. Neumann, in *Fracture* 1981, vol. 1 ICF5. Cannes (1981), p. 265.
34. H. Vehoff and W. Rothe, *Acta metall.* **11**, 1781 (1983).
35. A. J. Kumnick and H. H. Johnson, *Acta metall.* **28**, 33 (1980).
36. J. P. Hirth and H. H. Johnson, in *Atomistics of Fracture* (R. M. Latanision and J. R. Pickens, eds.) (Plenum Press, New York, 1983) p. 771.
37. K. Christmann, in *Atomistics of Fracture* (R. M. Latanision and J. R. Pickens, eds.) (Plenum Press, New York, 1983) p. 363.
38. J. Yu and J. R. Rice, in *Interfacial Structure, Properties and Design*, (M. H. Yoo, C. L. Briant and W. A. T. Clark, eds.), Mat. Res. Soc., vol. 122, (1988), in press.
39. J.-S. Wang, in *Interfacial Structure, Properties and Design*, (M. H. Yoo, C. L. Briant and W. A. T. Clark eds.), Mat. Res. Soc. vol. 122, (1988), in press.
40. D. Bouchet and L. Priester, *Scripta Metall.* **21**, 475 (1987).
41. V. Paidar, *Acta Metall.* **35**, 2035 (1987).
42. Metal Handbook, 9th edition, vol. 12, ASM, Metal Park, OH (1987) p. 21.
43. J.-S. Wang, *J. Mater. Res.* **3**, 16 (1988).
44. H. J. Frost, M. F. Ashby, and F. Spaepen, "A Catalogue of [100], [110] and [111] Symmetric Tilt Boundaries in Face-centered Cubic Hard-Sphere Crystals," MRL Technical Report, Harvard University (1982).

45. D. Wolf, in *Electronic Packaging Materials Science*, (E. A. Griess, K. N. Tue, and D. R. Uhlmann, eds.) (Mat. Res. Soc. vol. 40, 1985,) p. 341.

STRUCTURE OF GRAIN BOUNDARIES IN IRON

RALPH J. HARRISON*[1], FRANS SPAEPEN[2], ARTHUR F. VOTER[3], SHAO-PING CHEN[3],
(1)U.S. Army Materials Technology Laboratory, Watertown, MA 02172; (2)Division of Applied Sciences, Harvard University, Cambridge, MA 02138; (3) Los Alamos National Laboratory, Los Alamos, NM 87545.

INTRODUCTION

The present research has been carried out as part of the Steel Research Group's program to improve the properties of ultra-high-strength steels. It is an investigation of the mechanism of cohesion at grain boundaries as a step toward the design of alloy steel with improved resistance against boundary decohesion under stress corrosion conditions. This research involves a theoretical study of grain boundaries in iron alloys, examining the mechanism of cohesion as affected by structure including imperfections, by the average alloy composition and by segregation at the boundaries.

The direct way to carry out a theoretical investigation of the mechanism of cohesion would be to perform quantum mechanical computations of the electronic structure of different types of grain boundaries, using the results to compute the forces on individual atoms in the boundary, finding the equilibrium positions of the atoms where the forces are zero, and further using the knowledge of forces as a function of atom position to carry out simulations of boundary fracture due to known macroscopic forces. It is not at present computationally feasible to carry out this hypothetical program in complete detail, and therefore we have taken some shortcuts. Since the full program requires an iteration of the quantum mechanical computation as atomic positions are changed, we have attemped to obtain better starting positions by utilizing approximations for the initial configurations. First, we have used hard sphere models to make an overall survey of configurations of grain boundaries and alloying atoms in order to reduce the number of configurations which must be examined in more detail. Starting with the appropriate hard sphere models we then have used an approximation (the embedded atom method) for the interatomic forces which, although not as rigorous as a full quantum mechanical computation, may nevertheless bring about a significant improvement over the starting structure. Finally, the quantum mechanical computation that we plan to use at the end is also less exact but computationally much faster than the present state-of-

the-art methodology. The present paper summarizes what we have done to date in obtaining approximate grain boundary structures. We have tested the approximate interatomic potential for iron which we have obtained by using it to compute the interplanar spacings at the surface and then comparing the computed results with experimental observations. These results are also discussed below.

MODELS OF BOUNDARIES BETWEEN HARD-SPHERE CRYSTALS

The structure of close-packed metals (face-centered cubic or hexagonal) can be described well by a stacking of hard spheres. A number of boundaries between two identical, semi-infinite crystals have been constructed. Most of these are symmetrical boundaries for crystals in high-coincidence (low) orientations, since these boundaries have the shortest repeat lengths.

Hard sphere boundaries can be constructed with physical models, or simply graphically. For tilt boundaries, the two symmetrical half-crystals, projected onto a plane perpendicular to the tilt axis, are translated with respect to each other until a mechanically stable position that maximizes the density without atom overlap is found. Frequently, several mechanically stable configurations exist that are very close in density, so that the densest configuration requires a precise calculation from the atomic coordinates. In many cases the densest configuration is one in which a translation along the tilt axis is required, so that the planes perpendicular to the tilt axis do not continue through the boundary plane. Ashby et al. (1,2,3,4) have catalogued the highest coincidence boundary structures for the [100], [110] and [111] tilt axes, and have listed the sizes of the substitutional atoms and of the interstitials larger than those that fit into the lattice interstices.

Ashby et al. pointed out that structure of these grain boundaries can be described conveniently as a stacking of polyhedral units, formed by connecting the centers of neighboring spheres. This idea is similar to the "structural unit model" of Bishop and Chalmers (5) and has also been discussed by Pond et al. (6,7). Often these polyhedra only have triangles as faces, and are called "deltahedra". The ideal deltahedra, in which all edges have equal length, with 4 to 12 vertices are shown in FIGURE 1. The f.c.c. and h.c.p. hard sphere structures, for example, are made up entirely of tetrahedra and octahedra with edge length equal to the sphere

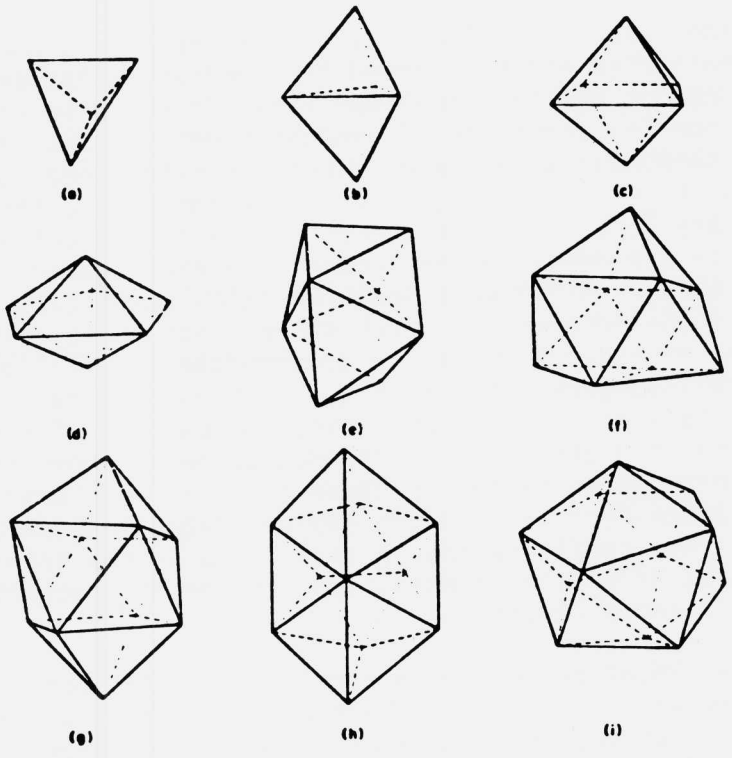

FIGURE 1. Ideal deltahedra with 4-12 vertices.

diameter, The icosahedron of FIGURE 1(i) is large enough to accommodate a central sphere if its edge lengths are 1.05 times the sphere diameter. In a fully densified single-size-sphere structure, no deltahedra with 12 or more vertices need be considered.

The deltahedron of FIGURE 1(f), which has nine vertices and can be described as a trigonal prism capped with a half-octahedron on each of its three square faces, is a common feature of tilt boundaries. Most of the half-octahedral caps are part of the two half-crystals making up the boundary. The deltahedron of FIGURE 1(g), which has ten vertices and is an Archimedian antiprism capped by two half-octohedra, is found in twist boundaries.

The deltahedra of FIGURE 1 have also been used to describe other structures, such as the dense random packing of hard spheres. Bernal (8) showed that such a structure could be described as consisting primarily of tetrahedra (84%), a few octohedra (6%), and the larger of the deltahedra: the

dodecadeltahedron of FIGURE 1 (e) (8 vertices), the capped trigonal prism and the capped Archimedian antiprism. The dense random packing model was later found to be the best model for the structure of amorphous metals (9). Many of these amorphous metals are transition metal-metalloid alloys, such as Ni_4P. Polk (10,11) first proposed that the metalloid atoms are located in the center of the larger deltahedra found in the dense random packed "skeleton" formed by the metal atoms. Although a detailed calculation (12) of the size of the interstices later showed that these deltahedra must be expanded somewhat to accommodate a sufficient number of metalloid atoms, the main qualitative features of the "hole-stuffing" picture were experimentally confirmed (13) the metalloid atoms are surrounded by metal atoms only, and the coordination number is close to nine. This means that the metal atoms tend to form the capped trigonal prism of FIGURE 1(f). This configuration is also found in the intermetallic compounds of similar composition, as the Ni_3P structure of FIGURE 2 shows (14,15).

The 36.87 degree symmetrical [100] tilt boundary (grain boundary vector [013]) in the b.c.c. structure was studied (1) by constructing the plastic sphere model (see FIGURES 3 and 4). The b.c.c. half-crystals are divided up into irregular tetrahedra while the grain boundary itself is made up of distorted capped trigonal prisms and tetrahedra. In each period of this $\Sigma = 5$, small period boundary, there are two sets of capped trigonal prisms along the [100] direction, with the base of the prism staggered by $a/\sqrt{2}$, where a is the lattice constant. The two prisms in the set differ in size; the smaller can fit an interstitial sphere of size 0.69 d as compared to 0.87d for the larger. d is the hard sphere diameter, taken as the nearest neighbor distance, $(1/2)\sqrt{3}$ times the lattice parameter a. It might be noted that as a measure of the distortion, the ideal trigonal prism would have a hole of diameter 0.52d. It is also of interest that when Ashby et al. (1) compared their hard sphere boundaries with those formed from "softer" spheres and from computer simulations, the tendency was to produce somewhat more symmetrical structures. We also find in our relaxed structures, as we shall see, more symmetry between the two prisms. In the iron grain boundary these interstitial sites might also be regarded as potential sites for atoms segregated at the grain boundary. The capped trigonal prism coordination around each of the phosphorus atoms in the boundary is similar to that found in intermetallic compounds such as Fe_3P, which has a structure (16) similar to that of FIGURE 2. There is some evidence that this occurs experimentally in iron boundaries (51).

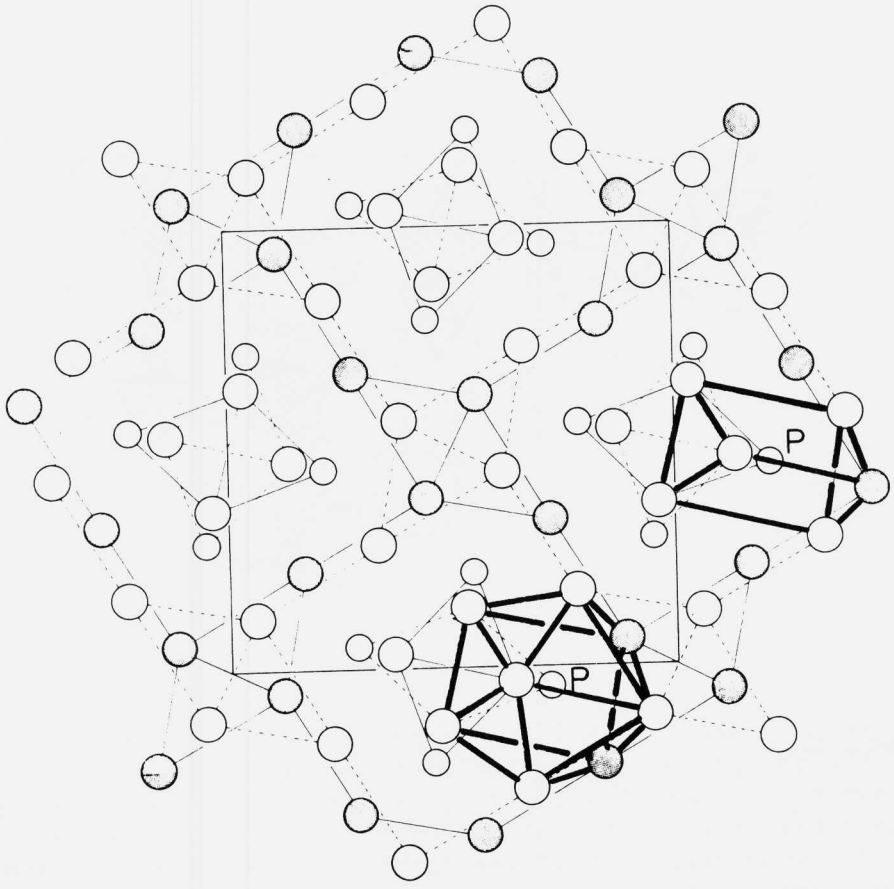

FIGURE 2. Atomic configuration in the body-centered tetragonal Ni_3P structure, viewed down the [001] axis. The larger circles are Ni-atoms; the smaller circles are P-atoms. One of the trigonal prisms around a P-atom is shown by itself. For another trigonal prism two capping half-octahedra are indicated as well; there is a third cap underneath the prism which is not shown and which completes the nine-metal-atom coordination shell around each P-atom.

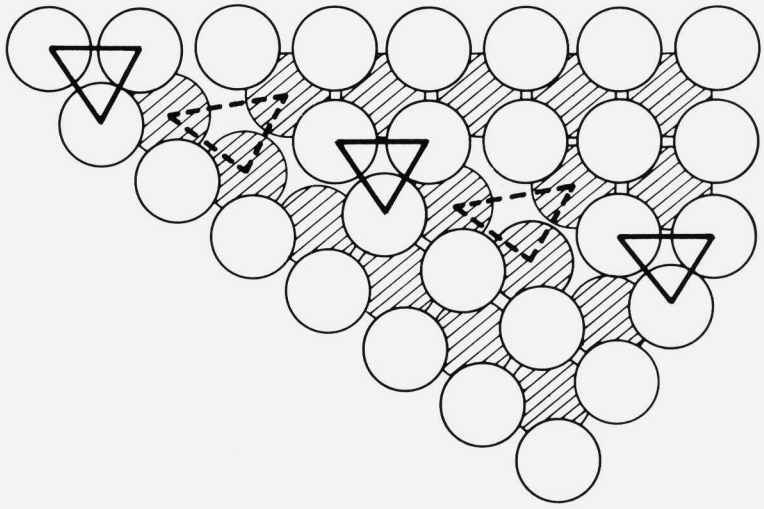

FIGURE 3. The $\Sigma = 5$ [100] boundary. The solid triangles are the top planes of one set of capped trigonal prisms, repeating periodically in the grain boundary plane, while the dashed triangles represent the other set of capped trigonal prisms, staggered by half the lattice parameter in the direction normal to the plane of the drawing. The triangles differ both in orientation and size.

In order to construct a cell that is periodic perpendicular to the boundary in the third dimension we must have two grain boundaries of opposite sense. We first constructed a figure representing a periodic array by simply photocopying FIGURE 4 for the single boundary; cutting and pasting, after turning the figure upside down, forming two boundaries of opposite sign in the required periodic array. Since the transverse shifts with respect to the coincidence structures are additive, the bottom half of the cell is displaced from the top half, and the cell has a monoclinic rather than a rectangular cross section (FIGURE 5).

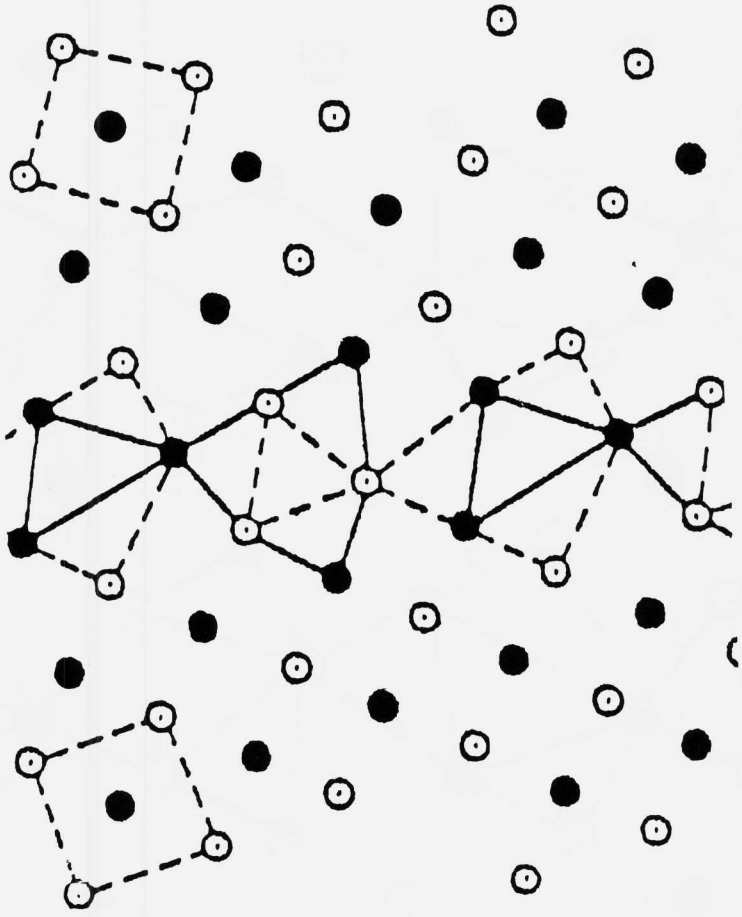

FIGURE 4. The $\Sigma = 5$ [100] tilt boundary between b.c.c. crystals from the hard sphere model. The squares show the rotation of the crystal by 36.9 degrees around the [100] tilt axis. The boundary plane is [310]. The shaded and the solid triangles show the two different size capped trigonal prisms formed in the structure.

If instead the second boundary in the crystal is constructed by using the mirror image of the first boundary, the transverse shifts are in opposite directions and cancel, and the resulting crystal remains orthotropic. The unit cell contains four capped trigonal prisms, two with the larger

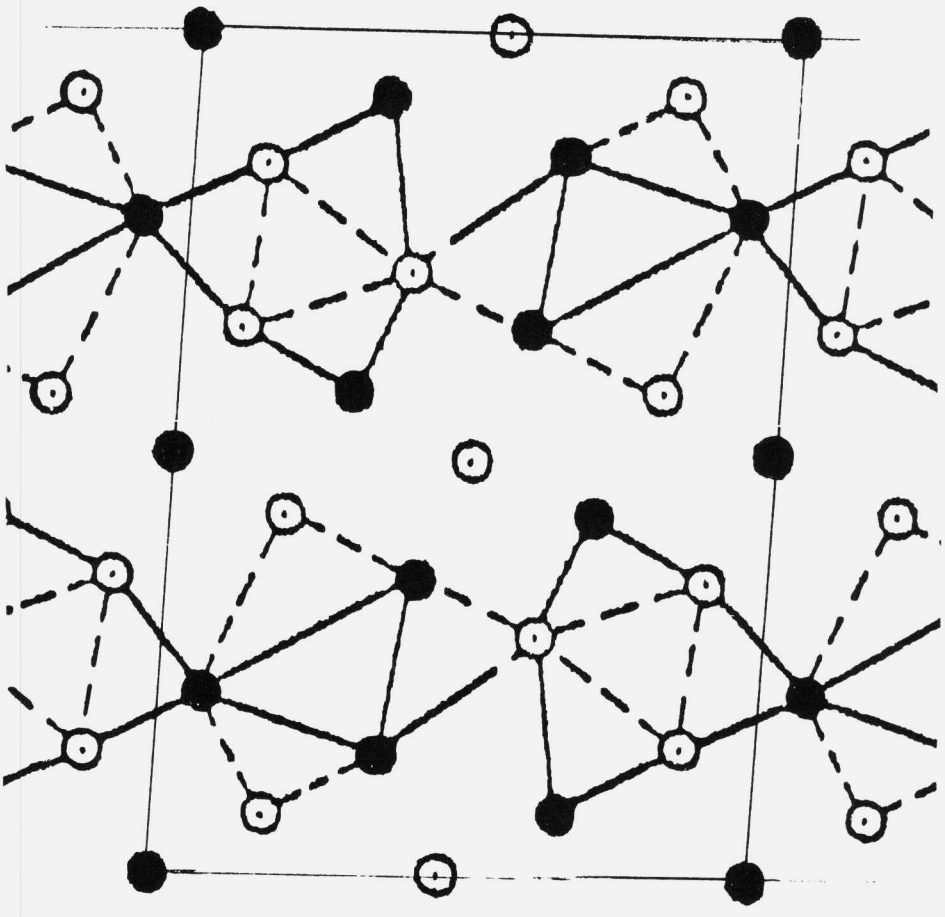

FIGURE 5. Periodic structure obtained from FIGURE 4 by constructing a cell with two grain boundaries, the second gotten from a simple rotation of the first boundary.

interstitial holes and two with the smaller holes. Depending on the distance between the two grain boundaries the unit cell may contain 16,20,24, etc. atoms. As with the conventional "slab" method, in principle one should calculate the electronic structure with increasing number of atoms per cell until one finds that the local electronic structure near the boundary becomes independent of size of cell. The 24 atom cell (FIGURE 6) contains four atoms that are not part of

the trigonal prisms. No atoms in the capped trigonal prisms in one boundary are in common with atoms in the prisms in the second boundary, although within each boundary there are shared atoms as described above. In the 20 atom cell of FIGURE 7 there is also no interboundary sharing, but there

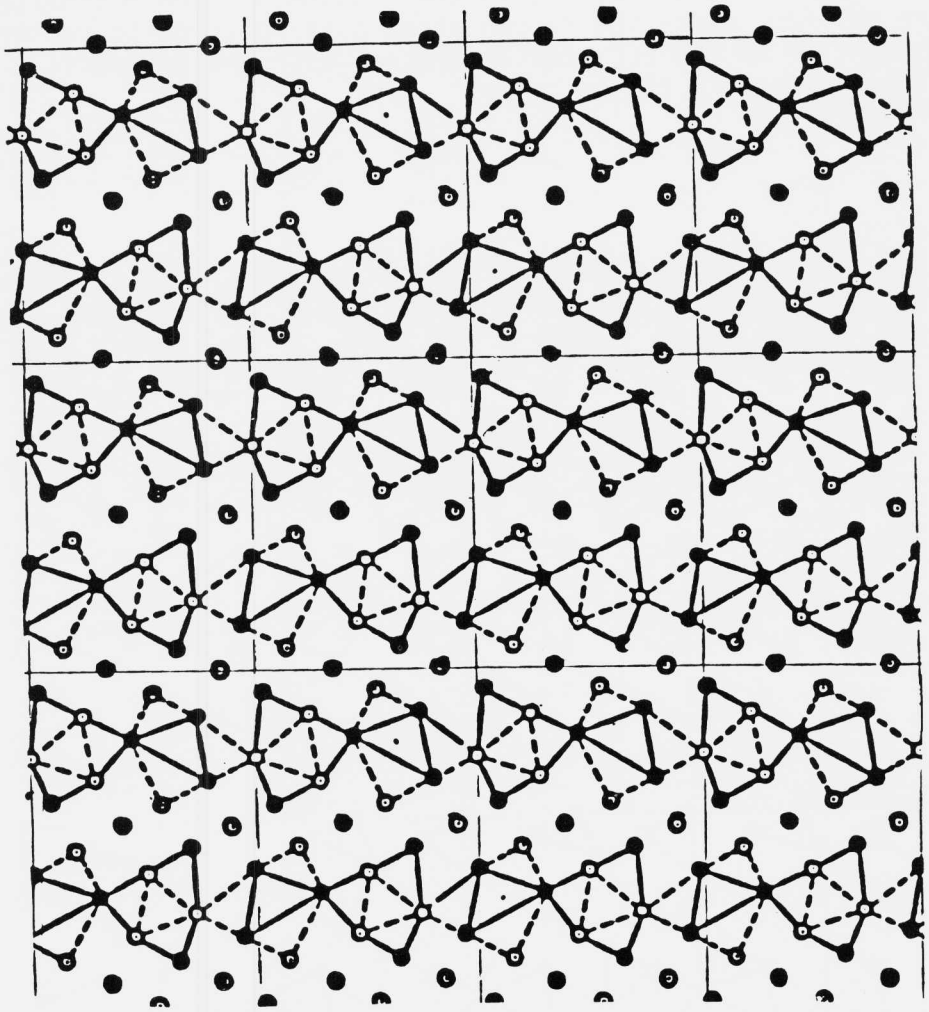

FIGURE 6. Periodic structure to be used for electronic energy band computation of grain boundary properties. Diagram shows 12 complete unit cells. Each cell contains 24 identical atoms, forming a pair of grain boundary structures separated by a small amount of b.c.c. crystalline material.

are no atoms which do not belong to the boundary prisms. In the 16 atom cell of FIGURE 8, four capped atoms in prisms belonging to one boundary are shared with capped atoms in capped trigonal prisms belonging to the second boundary. Although the region of the primitive crystal expands as the number of atoms per cell increases, even for the 16 atom cell the crystalline directions in the regions between boundaries are defined, since the capped atoms just referred to can be thought of as the body-centered-atom, with the prismatic atoms as corners of the cells.

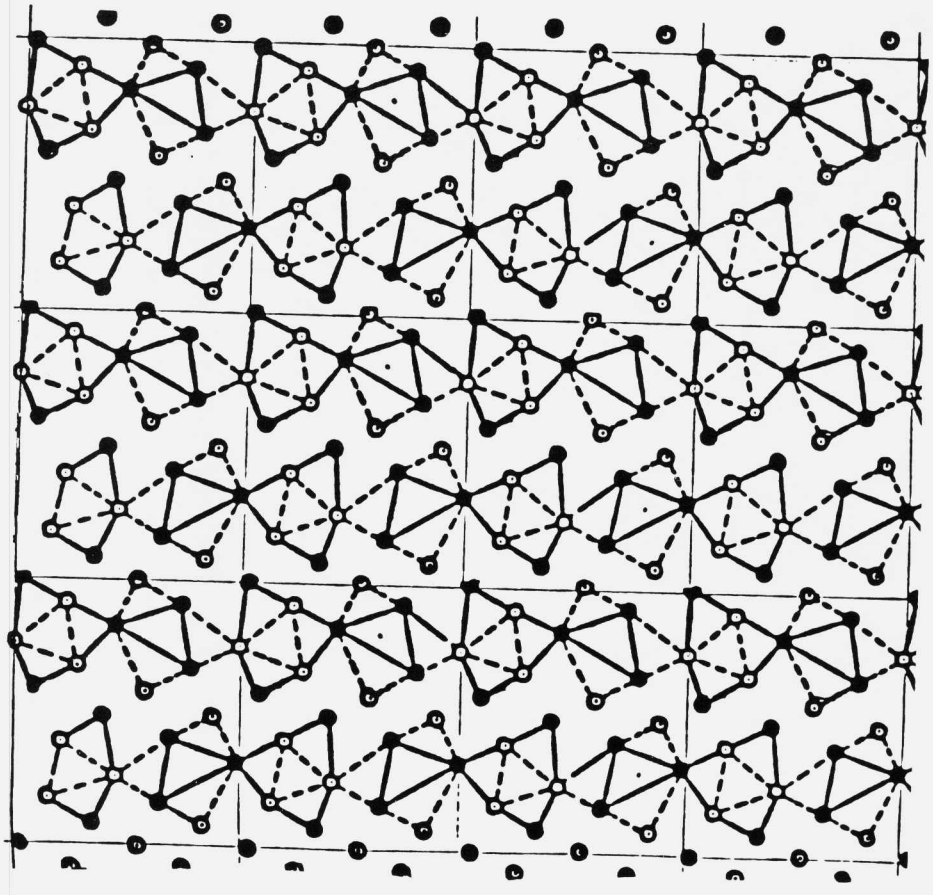

FIGURE 7. 20 atom periodic structure to be used for electronic energy band computation of grain boundary properties. Diagram shows 12 complete unit cells. Each cell contains 20 identical atoms, forming a pair of grain boundary structures, separated by b.c.c. crystalline material.

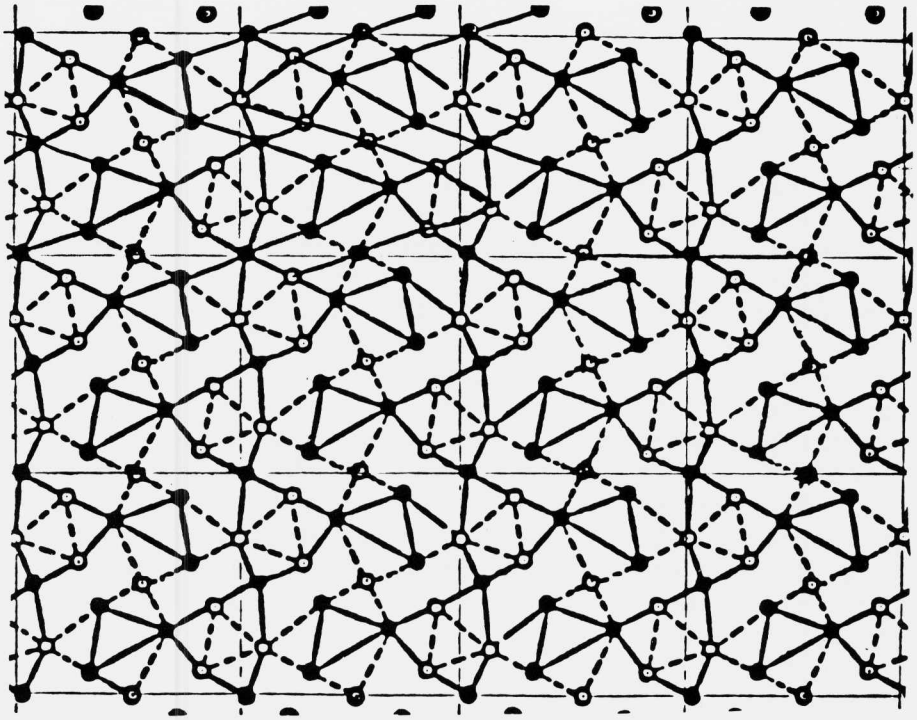

FIGURE 8. 16 atom periodic structure to be used for electronic energy band computation of grain boundary properties. Diagram shows 12 complete cells. Each cell contains 16 identical atoms, forming a pair of grain boundary structures. The "good" crystalline region between boundaries is barely discernible.

We have also utilized the hard sphere method to construct a Σ =3, [110] tilt boundary (grain boundary vector [-1,1,0]) in the b.c.c. crystal. Because, unlike in the f.c.c. case, the favored crystalline arrangement is not that of close packing, one has to be somewhat careful in adjusting the boundary for minimum volume (17).

RELAXATION OF GRAIN BOUNDARIES

Embedded atom potentials

We have chosen the embedded atom method (EAM) (18-21) to approximate the interatomic forces that could be used in a simulation to relax the hard sphere configuration and obtain reasonable starting configurations for the quantum mechanical computations. The reasons for the choice of the EAM to construct such forces are the following: The EAM potentials contain empirical parameters which enable the fitting of many experimental facts, without requiring a long theoretical computation. Pair potentials in the form of spline-fit potentials can also be parameterized (22) to fit experimental data. This was done, for example, by Pak and Doyama (23) to fit lattice constants, elastic constants, and the vacancy energy of iron with a short range, 5 parameter, pair potential; there are drawbacks to their use. For example, pair potentials always yield the Cauchy relations among elastic constants unless they are modified by the introduction of a volume-dependent term. In order to fit changes under hydrostatic pressure, one also may have to introduce volume or density dependence of other parameters in the potential. The problem is that there is no satisfactory way of defining the local specific volume where defects cause local changes in density; without such a definition, the compressibility as determined by uniform deformation will disagree with that obtained by the method of long waves (24). The EAM handles local gradients in density without having to explicitly define a local density or specific volume. It matches both the bulk modulus and cohesive energy quite accurately at the equilibrium volume and over a wide range of volumes through the use of the approximate universal features of the cohesive energy function (25-27). Also when one gets right down to it, perhaps the major reason for our use of EAM potentials rather than other methods (28-32) is simply that the techniques both for constructing such potentials and for using them in molecular dynamics or energy minimization computations have been embodied in computer programs already written and available to us (20,21).

Implementation of EAM. We shall now sketch the implementation of the EAM which we have used, in order to show how the parameters are chosen in this implementation to define the interatomic potential for use in a given application. The EAM uses an expression for energy which contains a many-body

embedding term, F(rho), and other additive terms represented by pair potentials phi(r). The two body pair potentials are taken to be Morse potentials, representing core-core interactions, with the three parameters v_1, v_2 and v_3 in the form

$$\text{phi}(r) = v_1[1 - \exp\{-v_3(r - v_2)\}]^2 - v_1. \qquad (1)$$

The argument, rho, of the embedding function F(rho) is obtained from the total charge density from linearly superimposing charge densities, rhofun, from individual atoms. The atomic wavefunctions are assumed to be 4s Slater functions with one adjustable parameter v_4. Rhofun, the square of the atomic wave function is then given by

$$\text{rhofun}(r) = r^6[\exp\{-v_4 r\} + 512 \exp\{-2v_4 r\}]. \qquad (2)$$

A fifth parameter is chosen as the value of the distance cutoff for both phi and rhofun, which are both adjusted to be smooth at cutoff.

The embedding function F(rho) does not contain any free parameters since it is determined completely by the values of the cohesive energy, the lattice constant and the bulk modulus, through the incorporation into the EAM (19) of the Rose et al. "universal function" (25-27), describing the volume dependence of the cohesive energy. The perfect crystal geometry determines the interatomic distances at a given volume, and then through the functions rhofun(r) determines the values of rho at each site. By including the contribution from the pairwise energies phi(r) as well as from F(rho) into the total energy equated to the Rose et al. function (25-27), the value of the embedding function F(rho) is determined for the given volume. As the structure is uniformly scaled in volume, the values of r at the lattice sites change and lead to different values of rho, and to corresponding values of F(rho), enabling one to tabulate the embedding function over a range of values of rho.

The input data required in the calculation to choose optimum potential parameters are: 1) the crystal lattice type; 2) an initial value for the cutoff radius for the potential which is usually chosen to be between 2nd and 3rd neighbors, and whose value is then adjusted by the program; 3) the values of elastic constants, C_{11}, C_{12} and C_{44} (deter-

mining the bulk modulus $(C_{11}+2C_{12})/3$); 4)the cohesive energy; 5) the (unrelaxed) vacancy energy. In previous work (21) Voter and Chen used also the binding energy and the equilibrium radius of the diatomic molecule. This was not done here for iron since the reference state for binding energy of the diatomic molecule is the free atom whose electronic state is quite different from that in bulk iron - for example Miedema and Gingerich (33) showed that the correlation between the dissociation enthalpies of homonuclear diatomic molecules with the heat of vaporization and the surface energy of the solid metals does not hold without correction for the 3d metals, whereas it does hold, for example, for aluminum and nickel which were modeled previously (20,21).

Validity of EAM. In order to get a better feeling for the limitations of the EAM it is useful to compare the present approach with the method used by Smith and Banerjea (34,35). In that work the total energy with a crystal with defects is written as

$$E = E^*(a^*)E_{coh} + E_{ion\text{-}core} + E_1 + E_2 + \ldots, \quad (3)$$

where a^* is the normalized Wigner-Seitz radius of the defect crystal minus that of the perfect crystal, with the normalization involving the bulk modulus as we have used. E_{coh} is the cohesive energy and $E^*(a^*)$ is the same universal function of Rose et al. (25-27) as used in the EAM. The second term on the right is the difference between the ion-core-ion-core interactions in the actual solid and in the perfect crystal, while the remaining terms E_n represent electronic correction terms which may be regarded as successively higher orders in a perturbation expansion. Smith and Banerjea (34,35) transform the expression for energy into a sum over individual atom sites, n, of "universal functions" of a^*_{On} and a double sum over neighboring sites m of universal functions of a^*_{mn}.

This simplified energy expression is made to be valid to second order by definition of "local" Wigner-Seitz radii and by fitting a parameter describing overlapping charge densities similar to the EAM use of overlapping charge densities to the vacancy formation energy. It appears that with some differences in detail, both the EAM as we have used it and the method of Smith and Banerjea are similar approximations to the formally more exact expression in the right hand side of Eq. (3). Both methods try to incorporate the right hand

terms into functions that can be expressed by sums over sites.

Since the "universal relations" closely describe only part of the cohesive energy of a metal, special methods must be used for those parts past the first term on the right of Eq. (3) arising from non-isotropic distortions. The EAM takes these into account in linear approximation by its match to the elastic constants. Finite changes of volume are accounted for by the universal relationship. The use of overlapping charge densities in the EAM also matches, through its fit to the vacancy energy, some of the effects associated with changes in local coordination. Long range electrostatic effects which might be associated with ionic bonding or with charge polarization at surfaces are not included. Energy changes associated with magnetic effects are also not taken into account explicitly, and we must therefore discuss why the EAM can nevertheless give a reasonable description of the potential for magnetic iron.

EAM Iron Potential

In trying to obtain a reasonable EAM potential we were concerned in view of the fact that the EAM as presently used does not consider magnetic contributions to energy directly. There are indirect ways that the magnetic effects are taken into account in part in the parameterization. For example, the EAM adjusts parameters to fit the vacancy energy. Part of the energy change associated with the formation of a vacancy may arise from the fact that the magnetism changes on the atoms neighboring the vacancy. Similarly, when one requires that the b.c.c. form of iron be more stable than the f.c.c., which is in fact a consequence of the magnetic energy terms, one is building into the potential an ability to mimic the consequences if not the causes of the difference associated with the change in magnetic state. This does not mean that the magnetic energy difference is correctly taken into account in other situations where corrections to energy are correlated with local changes in polarization due to changes in environment of the iron atoms.

The optimum fit to the properties of iron with the corresponding values of the parameters obtained are given in TABLE 1.

The fit to the elastic constants is only fair, and we could have obtained a much better fit had we been willing to forego the requirement the b.c.c. crystal should have a lower

TABLE 1

EMBEDDED ATOM POTENTIAL FOR BCC IRON

		Exptl	Calc'd	%dev.
lattice parameter (angstroms)	a_0	2.87	2.87	exact
sublimation energy (ev)	E_{sub}	4.28	4.28	exact
elastic constants	c_{11}	2.43	1.93	-21%
(10^{12} dyn/cm^2)	c_{12}	1.38	1.63	+18%
	c_{44}	1.22	1.05	-14%
vacancy formation energy unrelaxed			1.95	
relaxed		1.79	1.64	-9%

Crystalline cohesive energy and lattice parameters

E_{bcc} = -4.28 ev	$a_{0\ bcc}$ = 2.870
E_{fcc} = -4.260 ev	$a_{0\ fcc}$ = 3.605
E_{hcp} = -4.271 ev	$a_{0\ hcp}$ = 3.609

potential parameters:			
	v_1	2.32299	x10^{-2}Hartrees
	v_2	2.09238	angstroms
	v_3	1.34321	1/(angstroms)
	v_4	6.26195	1/(angstroms)
	v_5 (R_{cutoff})	4.52432	angstroms

energy than either the f.c.c. or the h.c.p., which we felt was a necessary requirement for any potential used to predict equilibrium defect structures. It is possible that the difficulties in matching the elastic constants arise from the neglect of spin-dependent contributions in the EAM, although possibly other parameterizations than given by Eqs. (1) and (2) may provide another way to obtain better fits.

Simulations using EAM iron potential

Surfaces. Since one of the well-known deficiencies of the usual pair potentials is the fact that they predict expansions in the interplanar spacings adjacent to surfaces whereas many metals show contractions (36,47), we have examined the predictions of the EAM potential for interplanar spacings near surfaces. We have relaxed slab geometries of atoms, with surfaces parallel to various crystalline directions. In this simulation we find the relaxed positions of atoms, and therefore the interplanar spacings near the surface as well as the position shifts parallel to the surface, with respect to positions in the interior of the bulk. Because these spacings have been measured in LEED experiments by Jona's group at Stony Brook (37-44), we have given a comparison between theory and experiment in TABLE 2.

Matthai and Bacon (45) used the tight binding potentials of Finnis and Sinclair (46) to compute the relaxation of the [100] surface of iron. They found an expansion of +1.5% for the first plane and an inward relaxation of 2.1% for the second plane. Jiang et al. (47) obtained good correlation with the experimental results for all iron surfaces using a simple one parameter fit based on an electrostatic model. Our EAM results in TABLE 2 show that there is some, although not complete, success in matching the qualitative features of the changes in surface spacings and their oscillations in depth. The fact that the simpler phenomenological theory, which takes into account the electrostatic term associated with the electronic readjustment at the surface (48), agrees with experiment as well as or better than the present theory, suggests that this term, neglected by the present implementation of the EAM, is important at surfaces. One would expect this term would be less important at grain boundaries.

Before making the present calculation, we had made a preliminary calculation of surface relaxations with an EAM potential which was fit to the correct binding and vacancy energies, but yielded only half the observed elastic constants. This potential predicted relaxations which, except

for the {110} surface where relaxations are small, gave the same signs as given by the present calculation. Both calculations agree with experiment in sign of relaxation for the {211}, {310},{111}, and {210} surfaces, and disagree with the

TABLE II

SURFACE RELAXATIONS IN IRON

SURFACE	SPACING	LAYER	EXP'TL CHANGE (PER CENT OF BULK)	ERROR	REF	PRESENT THEORY
{110}	2.03 A	1:	+0.5%	2 %	(40)	-.2%
		2:			"	+.01%
{100}	1.433	1:	-5 %	2 %	(39)	+1%
		2:	+5 %	"		-.8%
		3:			"	+0.1%
{211}	1.17	1:	-10.5%	3.5%	(42)	-7.8%
		2:	+5.1%			+6.6%
		3:	-1%			-5.7%
		4:				+4.3%
		5:				-3.3%
{310}	0.906	1:	-16.1%	3.3%	(44)	-23.8%
		2:	+12.6	3.3%	"	24.4%
		3:	-4.0	4.4%	"	-20.3%
		4:				+16.2%
		5:				-12.2%
{111}	.827	1:	-16.9	3.0%	(38)	-4.8%
		2:	-9.8	3.0%	"	-7.8%
		3:	+4.2	3.6%	"	+8.9%
		4:	-2.2	3.6%	"	-3.5%
		5:				-2.3%
{210}	.647	1:	-22		(37)	-14.7%
		2:	-11		"	-18.0%
		3:	+17		"	+34.6%
		4:	-4.8	4.7%	"	-15.8%
		5:				-13.6%
		6:				+23.3%

sign of the experimental relaxation for the [100] surface.

Although the overall fit seems appreciably better for the corrected potential, the difference between the two predictions is perhaps less than one might have expected. The conclusions one may draw are : 1)the qualitative agreement of the surface relaxation cannot be taken as a quantitative validation of the potential; 2)the quantitative deviation between observed and predicted spacings suggests that probably the corrections to the EAM potential at surfaces which arise from the electrostatic term referred to above is significant.

Grain Boundary Studies

Finally, we shall report on the results of our grain boundary studies using the EAM potential for iron. We utilized the same slab geometry as was described for the surface studies, but with the grain boundary in the center of the slab, parallel to the slab surface. The computation gives values of grain boundary surface energy in addition to the relaxed boundary atom positions and the value of the grain boundary free volume at zero pressure. It also gives the free surface energy on surfaces parallel to the boundary plane. We have started with the hard sphere geometries for the [100] (031) and for the [110] (1,-1,1) tilt boundaries. We found for these boundaries that the final relaxed positions were the same over a wide range of starting positions, whether we used initial positions as the original coincidence positions, (although shifted perpendicular to the boundary plane to avoid hard sphere overlap) or whether there were shifts parallel to the boundary plane. In particular we found that the final relaxed position of the $\Sigma = 5$, (031) tilt boundary was such that the inequality in the sizes of the interstitial holes in the capped trigonal prisms found in the boundary structure in the hard sphere model had disappeared (FIGURE 9).

This tendency toward a more symmetrical boundary structure as one softened the originally hard sphere potential is also in accord with what was found previously by Ashby et al. (1) who compared their hard sphere structures with those found in bubble models or computer simulations. We also note that in simulations of iron grain boundaries by Hashimoto et al. (49) using Morse (pair) potentials, their $\Sigma = 5$, (031) boundary also exhibited a symmetrical structure with both trigonal prisms the same size.

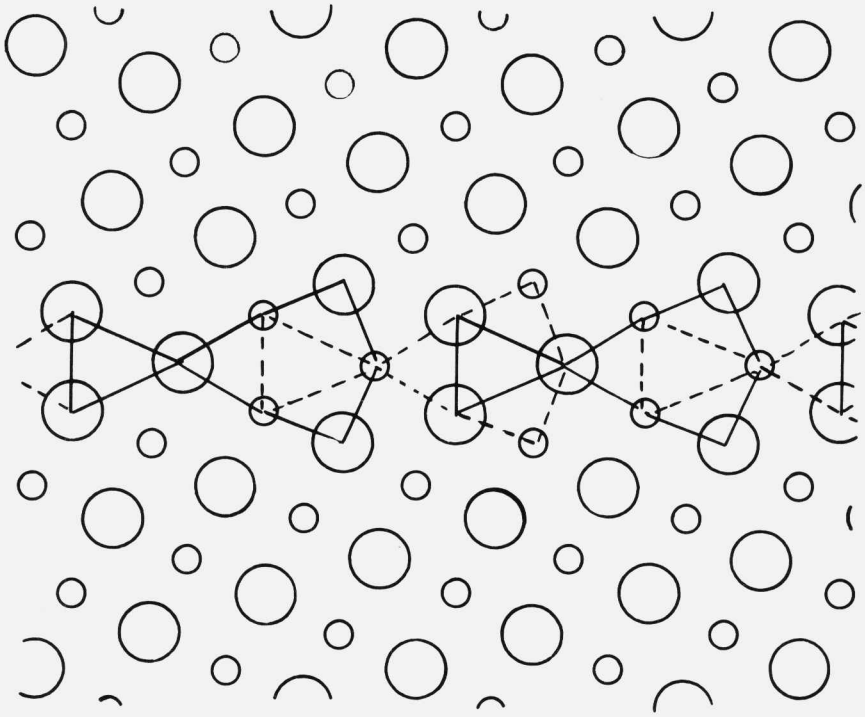

FIGURE 9. Same grain boundary as in FIGURE 4, but relaxed with EAM iron potential.

Hashimoto et al. (49) also studied the structures obtained by incorporating phosphorus or boron atoms as impurities in iron, again with Morse potentials for the interaction between the iron atoms and the boron or phosphorus. They found that the sites inside the trigonal prisms were in fact occupied by these impurity atoms.

We have tabulated the results for the boundaries studied in TABLE III.

The last column tabulated gives the energy per unit area required to fracture the grain boundary, creating two planar surfaces (50,52).

TABLE 3

SIMULATION RESULTS ON GRAIN BOUNDARIES

TILT_AXIS	BOUNDARY PLANE	SURFACE ENERGY	GB ENERGY	2*SURFACE-GB ENERGY
100	031	1834mJ/m^2	842mJ/m^2	2826
100	021	1816	744	2888
110	$1\bar{1}1$	1980	931	3029

We may also compare the values of surface energy with the value of 1810 mJ/m^2 for the (110) surface and 3490 mJ/m^2 for the (100) surface computed by Smith et al. (34), and the value of 3100 mJ/m^2 for the (100) surface by Richter et al. (53). Smith et al. (34) also suggest that the experimental value for polycrystalline iron should be in between the values of the two lowest energy surfaces. However the value of 2452 mJ/m^2 obtained by Wawra (54) which they quote is actually derived from a low temperature measurement of elastic constants, using a correlation suggesting the surface energy is 1.41×10^{-9} times the bulk modulus. There is a measurement of Gilman (55) at liquid hydrogen temperatures of the energy to cleave iron-silicon (3% Si) crystals on (100) planes, obtaining a value of 1360 mJ/m^2 under conditions that cleavage occurs without apparent plastic deformation. Mazanec and Kamenska (56) measured the grain boundary energy of austenite at 1100 C as 0.4 times the solid-vapor free energy, which was separately determined to be 1950 mJ/m^2.

The work of Matthai and Bacon (45) cited above obtained a (100) surface energy of 1682 mJ/m^2.

ACKNOWLEDGMENTS

A. F. Voter and S. P. Chen wish to acknowledge support of this work by the Energy Conversion and Utilization Technologies (ECUT) Program of the U.S. Department of Energy.

REFERENCES

1. M.F. Ashby, F. Spaepen and S. Williams, Acta metall. 26, 1647-1663 (1978)

2. M.F. Ashby and F. Spaepen, Scripta metall. 12, 193 (1978)

3. H.J. Frost, M.F. Ashby and F. Spaepen, Scripta Metall. 14, 1051 (1980).

4. H.J. Frost, M.F. Ashby and F. Spaepen, A Catalog of [100], [110], and [111] Symmetrical Tilt Boundaries in Face-centered Cubic Hard Sphere Crystals, Materials Research Laboratory Technical Report, Division of Applied Sciences, Harvard University, Cambridge MA (1982)

5. G.H. Bishop and B. Chalmers, Phil. Mag. 24, 515-526 (1970)

6. R.C. Pond, V. Vitek and D. A. Smith, Acta metall. 27, 235 (1979)

7. R.C. Pond, V. Vitek and D. A. Smith, Acta Cryst. A35, 689 (1979)

8. J.D. Bernal, Proc. Roy. Soc. (A) 280, 299 (1964)

9. G.S. Cargill III, Sol. St. Phys. 30, F. Seitz, D. Turnbull and H. Ehrenreich, Eds., (Academic Press, New York, 1975) p. 227

10. D.E. Polk, Scripta metall. 4, 117 (1970).

11. D.E. Polk, Acta metall. 20, 485 (1972).

12. H.J. Frost, Acta metall. 30, 889 (1972)

13. J. F. Sadoc and J. Dixmier, Materials Sci. and Eng. 23, 187 (1976)

14. S. Rundqvist, Acta Chem. Scand. 16, No.1 242 (1962)

15. S. Rundqvist, Ark. Kemi 20, 67 (1962).

16. S. Rundqvist, Acta Chem. Scand. 16, 10 (1962).

17. V. Vitek, D.A. Smith and R.C. Pond, Phil. Mag. A41, 649 (1981)

18. M.S. Daw and M.I. Baskes, Phys. Rev. B29, 6443 (1984)

19. S.M. Foiles and M.S. Daw, J. Mater. Res. 2, 5-15 (1987)

20. S.P. Chen, A.F. Voter, D.J. Srolovitz, "Oscillatory Surface Relaxations in Ni, Al, and their ordered Alloys", Phys. Rev. Letters 57, 1308-11 (1986)

21. A.F. Voter and S.P. Chen, Mater. Res. Soc. Symp. 82, 175 (1987).

22. R.A. Johnson, Phys. Rev. 145, 423 (1966)

23. H.M. Pak and M. Doyama, J. Fac. Engineering, U. of Tokyo, B30, 111 (1969)

24. R.J. Harrison, in Condensed Matter Theories, Vol. I, F.B. Malik, Ed., p.207-213

25. J. H. Rose, J. R. Smith, F. Guinea, J. Ferrante, Phys. Rev. B29, 2963 (1984)

26. J. H. Rose, J. R. Smith, J. Ferrante, Phys. Rev. B28, 1835 (1983)

27. J.R. Smith, J. Ferrante, P. Vinet, J.G. Gay, R. Richter, J.H. Rose, in Chemistry and Physics of Fracture, R.H. Jones and R.M. Latanision, eds. (Martinus Nyhoff, Hingham, MA, 1987), p.329

28. K. Masada and A. Sato, "Electronic theory for screw dislocation in b.c.c. transition metals: Calculation of the Peierls stress and the core energy", Phil. Mag. B37, 531-536 (1978)

29. G. Allan and M. Lanoo, Surface Sci. 40, 375 (1970); Phys. Status Solidi (b)74, 409 (1976); J. Phys. Chem. Solids 37, 699 (1976)

30. A. Sato and K. Masuda, Solid State Commun. 29, 545 (1979)

31. K. Masuda and A. Sato, J. Phys. Soc. Japan 50, 569 (1981)

32. G.J. Ackland and M.W. Finnis, Philos. Mag. A54, 301 (1986)

33. A.R. Miedema and K.A. Gingerich, "On the formation enthalpy of metallic dimers", J. Phys. B: Atom. Molec. Phys., 12, 2081-2095 (1979)

34. J.R. Smith and A. Banerjea, Phys. Rev. Letters 59, 2451 (1987)

35. J.R. Smith and A. Banerjea, "Equivalent Crystal Theory of Oscillatory Surface Relaxation", Phys. Rev. B32, 10411-10414 (1988)

36. R.P. Gupta, "Lattice relaxation at a metal surface", Phys. Rev. B23, 6265-6270 (1981)

37. J. Sokolov, F. Jona, P.M. Marcus, "Multilayer relaxation of the Fe 210 surface", Phys. Rev. 31, 1929-1935 (1985)

38. J. Sokolov, F. Jona, P.M. Marcus, "Multilayer relaxation of a clean bcc Fe(111) surface, Physical Review B33, 1397-1400 (1986)

39. Z.W. Wang, Y.S. Li, F. Jona, P.M. Marcus, "Epitaxial growth of body-centered-cubic nickel on iron", Solid State Commun. 61, 623-626 (1987)

40. H.D. Shih, F. Jona, U. Bardi, P.M. Marcus, "The atomic structure of Fe(110)",J. Phys. C.:Solid State Phys. 13, 3801-8 (1980)

41. H.D. Shih, F. Jona, D.W. Jepsen, P.M. Marcus, "Atomic structure of Fe(111)", Surface Science, 104, 39-46 (1981).

42. J. Sokolov, H.D. Shih, U. Bardi, F. Jona, P.M. Marcus, "Multilayer relaxation of body-centered-cubic Fe(211)", J. Phys. C17, 371-383 (1984)

43. J. Sokolov, H.D. Shih, U. Bardi, F. Jona, "New relaxation phenomena in the outer atomic layers of Fe(211)", Solid State Commun. 48, 739-741 (1983)

44. J. Sokolov, F.Jona, P.M. Marcus, "Parallel and perpendicular multilayer relaxation of Fe {310}", Phys. Rev. B29, 5402-5409 (1984)

45. C.C. Matthai and D.J. Bacon, "Relaxed vacancy formation and surface energies in b.c.c. transition metals", Phil. Mag. A52, 1-3 (1985)

46. M.W. Finnis and R. Sinclair, "A simple empirical N-body potential for transition metals", Phil. Mag. A50, 45-55 (1984)

47. P. Jiang, P.M. Marcus, F. Jona, "Relaxation at clean metal surfaces", Solid State Commun. 59, 275-280 (1986)

48. M.W. Finnis and V. Heine, J. Phys. F (Metal Physics) 4, L37 (1974)

49. M. Hashimoto, Y. Ishida, R. Yamamoto and M. Doyama, Acta metall. 32, 1-11 (1984)

50. M.C. Inman and H.R. Tipler, Met. Rev., 8, No. 30, 105 (1963); see page 158.

51. K. Abiko, S. Suzuki, H. Kimura, "Chemical state of phosphorus segregated at grain boundaries in iron", Iron and Steel (Japan) 69, 35-40 (1983)

52. J.P. Hirth and J.R. Rice, Met. Trans. 11A, 1501 (1980)

53. R. Richter, J.R. Smith and J.G. Gay, in The Structure of Solid Surfaces, (Springer Series in Surface Sciences, vol.2, Berlin 1985), M.A. Van Hove and S.Y. Tong, Eds.,pp35-40

54. H.A. Wawra, "The surface energy of solid materials as measured by ultrasonic and conventional test methods", Z. Metallkde 66, 395-401 (1975)

55. J.J. Gilman, "Direct measurements of the surface energies of crystals", J. Appl. Phys. 31, 2208-2218 (1960)

56. K. Mazanec and E. Kamenska, "Surface tension at the boundary of austenite grains", Fiz. Metal. i Metalloved. 12, No.1, 91-6 (1961)

EVALUATION OF DECOHESION MECHANISMS IN IRON BY LMTO-ASA-STONER COHESIVE ENERGY CALCULATIONS

G.L. Krasko* and G.B. Olson**
Department of Materials Science and Engineering
Massachusetts Institute of Technology
Cambridge, Massachusetts 02139

1. INTRODUCTION

"First principles" design of materials is a pipedream of materials scientists. The electronic theory of the solid state, since its first steps in the beginning of the century, has always had this challenging goal as one of its ultimate objectives. Formidable as it is, this problem is of utmost importance for both the future development of new materials, and for improving the quality of existing ones.

The recent progress in high speed computers and software has stimulated a more aggressive approach of physicists and materials scientists in their attempts directed at first principles understanding of not only the traditional electronic properties of materials, but their mechanical properties as well. A new family of efficient methods of band structure and total energy calculations today enables a materials scientist to calculate with the necessary precision such delicate properties as cohesion energy, surface, and grain boundary energies, as well as magnetic energies.

One of the most efficient methods of today's first principles analysis is the so-called "Linear Muffin Tin Orbitals" (LMTO) method. Developed in 1975 by O.-K. Andersen [1-4] the method has since been successfully used on many different systems: from pure metallic crystals to complex compounds and supercell models. In combination with the so-called Atomic Sphere Approximation (ASA) the method is some two orders of magnitude faster than most of the traditional methods used earlier.

During the recent, decade iron has been an object of extensive first principles study (for references, see e.g.

---

*now with the US Army Materials Technology Laboratory, Watertown, MA 02172
**now with Department of Materials Science and Engineering Northwestern University, Evanston, Il. 60208

[5,6]). A wide spectrum of bulk properties was investigated: the bandstructure, magnetic properties, and crystal lattice energies in various crystallographic modifications. A few researchers have also dealt with the iron surface properties: the magnetic moment and the work function [7-9]. Of great interest at present are thin films containing layers of Fe [10-12].

In the present work, we examine the energetics of iron surfaces: the surface energy and its change upon adding nickel atoms on and below the (100) surface of the BCC lattice. The ability of Ni to inhibit the (100) cleavage fracture of iron is well-established. We will show that, thermodynamically, the latter results from the ability of Ni atoms to increase the iron surface energy when present on the surface or right below it. This then increases the "Griffith work" of brittle separation on the (100) cleavage plane. The analysis of the surface energies, which is possible in our approach due to separate calculations of nonmagnetic ("chemical") and ferromagnetic contributions, shows that the cohesion enhancing quality of Ni results mainly from suppressing the (negative) ferromagnetic contribution.

In a wider context, this research is part of a more general investigation of decohesion mechanisms in iron and its alloys responsible for mechanical failure by both transgranular and intergranular cleavage.

Beginning with the pioneering work by Briant and Messmer [13-15] the electronic aspects of decohesion have attracted much attention. In this respect, the molecular cluster calculation method was widely used [16-20]. Our approach emphasizes the cohesion energy rather than bonding behavior. The two methods may be looked upon at the present time as complimentary.

The plan of the paper is as follows: In Section 2 we briefly summarize the LMTO-ASA-Stoner method of total energy calculations. In Section 3 we discuss the supercell approach in description of surfaces and present the 16 atom supercells which were used in our calculations. Results of these calculations thus far are then discussed in Section 4.

2. LMTO-ASA-STONER APPROACH FOR TOTAL ENERGY CALCULATIONS

Most of the first-principles methods used today are based on the so-called Density-Functional Formalism [21-22].

The formalism's efficiency and success is based on two elegant theorems, which allow formulation of many-electron problem of a real physical object in terms of a ficticious system of noninteracting electrons in an effective external field. Computationally, the problem is then reduced to (self-consistent) solving a one-electron, Schrödinger type equation with external potential which can be found in a systematic and well-defined way. The only "unknown" component of the physical picture is the exchange-correlation potential. The latter, however, may be treated within the so-called "local spin-density approximation". From a computational point of view, the LMTO-method is much faster than the "non-linear" methods. This is due to the fact that in calculating the energy dependent quantities the method uses a linear approximation which happens to be sufficient even for describing such high precision quantities as the electronic band structure or the density of states. The Atomic Sphere Approximation (ASA) makes the method even more efficient. Unlike the so-called Muffin-Tin (MT) model, when the Schrödinger equation is solved separately within the touching atomic MT spheres and interstitial volume, and the two solutions are matched, the ASA eliminates the interstitial area by expanding the MT spheres to the size corresponding to the volume per atom. Thus, in the ASA approximation, the whole crystal volume is covered by spheres, which are, in fact, the Wigner-Seitz cells. Of course, in some directions the spheres slightly overlap, while in the others there are voids. The ASA approximation has been shown to work better, the more close packed the crystal lattice is. In an "open" structure like that of diamond, some "empty spheres" should be introduced in order to make the volume coverage more efficient.

In doing calculations for iron, one should be able to treat correctly the spin-polarization which gives rise to ferromagnetism. The LMTO-ASA method has been successfully used in calculating ferromagnetic systems. However, if one is to analyze the role of ferromagnetism with respect to a nonmagnetic situation, two separate calculations must be performed without and with spin-polarization. For a large system (like a multi-atom supercell) even a nonspinpolarized calculation is slowly convergent: in order to achieve self-consistency, some 150-200 interactions have to be run. The convergence of a spin-polarized calculation is even slower.

In order to resolve this difficulty we have chosen not to perform spin-polarized calculations. Rather, in calculating both the magnetic moment and ferromagnetic contribution to the energy, we make use of the Stoner theory of

itinerant ferromagnetism [23]. Beginning with the pioneering work of the 70s [24-26], the Stoner approach in combination with non-spinpolarized self-consistent calculations has been successfully used in describing the ferromagnetism of iron. Particularly, the metamagnetic behavior of the FCC iron was analyzed in detail [27]. Recently, the energetics of the FCC-BCC phase transformation in iron was also calculated using the Stoner approach [28].

Briefly, the Stoner approach consists of the following. First a self-consistent non-spinpolarized solution for the system of interest is found. In iron, this will not correspond to the lowest energy. In order to lower the energy further, a number of electrons will change their spin and flip from under the Fermi-surface into unoccupied states right above the Fermi-surface. The process of flipping will cease when the increase of kinetic energy will be overcompensated by exchange interaction among the electrons. This process may be looked upon as a rigid shift of spin-up and down subbands, each of which would preserve the shape of the non-spinpolarized band. According to [29,30] this would correspond to first order perturbation theory in m/n_d (m is the magnetic moment and n_d is the total amount of d-electrons per atom). Thus, the procedure of finding the magnetic moment and magnetic energy may be easily accomplished if the self-consistent electronic density of states for the non-magnetic system is known.

The Stoner theory contains one unknown parameter, I, the so-called Stoner exchange parameter. The latter can be, in principle, found using linear response theory [30] from calculations on the nonmagnetic system. In [28], a procedure has been described for "enhancing" the "first principles" value of I ($=I_0$) by the factor 1.075. By doing so, the equilibrium lattice parameter of the ferromagnetic BCC iron calculated within the Stoner model becomes equal to the experimental value. This approximation is adopted in the calculations reported here. No other adjustment has been made.

To summarize, the LMTO-ASA-Stoner approach enables one to find the nonmagnetic energies of atomic spheres of all the atoms in the unit cell (or supercell), the total energy of the cell, the magneic moments and magnetic energies for each sphere, electronic densities of states in each sphere, and the electronic band-structure.

3. SUPERCELL APPROACH DESCRIPTION OF FREE SURFACES

The LMTO-ASA method has been designed to calculate pro-